NTIA Report 13-491

Conducted and Radiated Emissions Measurements of an Ultrawideband Surveillance Radar

Robert T. Johnk
Frank H. Sanders
Kristen E. Davis
Geoffrey A. Sanders
John D. Ewan
Ronald L. Carey
Steven Gunderson

report series

U.S. DEPARTMENT OF COMMERCE • National Telecommunications and Information Administration

NTIA Report 13-491

Conducted and Radiated Emissions Measurements of an Ultrawideband Surveillance Radar

Robert T. Johnk
Frank H. Sanders
Kristen E. Davis
Geoffrey A. Sanders
John D. Ewan
Ronald L. Carey
Steven J. Gunderson

U.S. DEPARTMENT OF COMMERCE

November 2012

DISCLAIMER

Certain commercial equipment and materials are identified in this report to specify adequately the technical aspects of the reported results. In no case does such identification imply recommendation or endorsement by the National Telecommunications and Information Administration, nor does it imply that the material or equipment identified is the best available for this purpose.

CONTENTS

FIGURES

TABLES

ABBREVIATIONS/ACRONYMS

dB	Decibel
DOD	Department of Defense
DRH	Dual-Ridged Horn (Antenna)
EIRP	Effective Isotropic Radiated Power
EMC	Electromagnetic Compatibility
HERO	Hazards of Electromagnetic Radiation to Ordinance
HERP	Hazards of Electromagnetic Radiation to Personnel
ITS	Institute for Telecommunication Sciences
NAVFAC	Naval Facilities Engineering Command
NSWC	Naval Surface Warfare Center
NTIA	National Telecommunications and Information Administration
RBW	Resolution Bandwidth
RMS	Root mean square
SLiMS	Shoreline Intrusion Monitoring System
TDMA	Time-Division Multiple Access
UWB	Ultrawideband
VNA	Vector Network Analyzer

CONDUCTED AND RADIATED EMISSIONS MEASUREMENTS OF AN ULTRAWIDEBAND SURVEILLANCE RADAR

Robert T. Johnk, Frank H. Sanders, Kristen Davis, Geoffrey A. Sanders, John D. Ewan, Ronald L. Carey,[1] Steven J. Gunderson[2]

We provide detailed descriptions of recent measurements conducted by the National Telecommunications and Information Administration Institute for Telecommunication Sciences in Boulder, Colorado. ITS engineers performed a comprehensive series of both conducted and radiated emission measurements of the Shore-Line-intrusion-Monitoring System (SLiMS). The SLiMS system is currently being developed by Time Domain® under the sponsorship of the Naval Facilities Engineering Command.

The measurement results demonstrate both low levels emissions that are consistent with existing U.S. electromagnetic compatibility requirements and a low potential for causing interference to incumbent systems.

Key words: amplifier; antenna; bandwidth; calibration; dual-ridged horn; dish antenna; effective isotropic radiated power; frequency-domain; oscilloscope; power; resolution; spectrum analyzer; time-domain; waveform

1 INTRODUCTION

1.1 Background

The United States is currently facing increasingly significant security threats, and the dangers to U.S. personnel and assets have increased significantly overseas and at home. The U.S. Department of Defense (DOD) needs to use surveillance radars to detect and identify intruders on the ground. These systems must be compatible with incumbent electronic systems and not pose safety hazards to other equipment or personnel. In order to ensure safe operation that complies with existing electromagnetic compatibility requirements, the radio-frequency emissions characteristics of these surveillance systems must be thoroughly understood. The Institute for Telecommunication Sciences (ITS) of the National Telecommunications and Information Administration (NTIA) possesses a unique combination of engineering expertise, equipment, and facilities to measure and evaluate the radio-frequency (RF) performance of these systems.

---

[1] The authors are with the Institute for Telecommunication Sciences, National Telecommunications and Information Administration, U.S. Department of Commerce, Boulder, CO 80305.
[2] The author is with the Naval Facilities Engineering Command, Port Hueneme, CA 93043.

The Naval Facilities Engineering Command (NAVFAC) is sponsoring the development of an ultrawideband (UWB) radar fence that can track and image intruders, the Shore-Line Intrusion Monitoring System (SLiMS). The radar consists of a distributed system of autonomous transmit/receive modules mounted on poles, which are deployed around the perimeter of a facility to be protected. The number of poles and modules varies depending on the coverage needed. There are currently plans to operate SLiMS at Whidbey Island Naval Air Station, Washington, to provide perimeter security and the U.S. Department of Energy (DOE) is currently experimenting with SLiMS at one of its facilities.

At the request of NAVFAC, ITS engineers performed a comprehensive set of emissions measurements on a shortened pole structure containing a single radar module. NAVFAC wants to ensure that their system transmits levels that fall below NTIA and Federal Communications Commission (FCC) UWB radiated emissions limits and that their system is safe to operate. ITS coordinated with electromagnetic compatibility (EMC) engineers at the Naval Surface Warfare Center (NSWC) in Dahlgren, Virginia to ensure that the system does not constitute an electromagnetic radiation hazard to either personnel or ordinance (HERP/HERO).

1.2 ITS EMC Tests

During the period of October, 2011-June, 2012, a team of ITS engineers performed a series of EMC tests on a custom designed SLiMS system consisting of a shortened dielectric pole and a single model P400 ultrawideband radar module, which is manufactured by Time Domain® (TDC Acquisition Holdings, Inc. (TDC)).

Two types of tests were performed: 1) hardline conducted emissions and 2) radiated emissions measurements. We performed a full suite of frequency-domain measurements using a spectrum analyzer as well as a set of full-bandwidth measurements using a high-speed oscilloscope. We carried out the spectrum measurements using an Agilent PXA 9030A signal analyzer configured as a spectrum analyzer. We used a Tektronix TDS 6124C high speed real-time oscilloscope (BW = 12 GHz) to capture time-domain records.

We carried out the conducted measurements by connecting the P400 ultrawideband radar module to either the spectrum analyzer or the oscilloscope using a short section of low-loss, precision microwave cable. We performed spectrum measurements over a frequency range of 1–15 GHz with a range of resolution bandwidths extending from 100 kHz to 8 MHz and we used both peak and average detection. We also captured time-domain records with the oscilloscope to investigate the structure of the UWB radar waveform. The time-domain signal properties were used to set the instrument parameters for the spectrum analyzer measurements.

We performed the radiated measurements over a frequency range of 1–14 GHz inside a fully anechoic chamber at the Department of Commerce Boulder Laboratories campus in Boulder, Colorado. The chamber provides a high level of RF shielding, low noise, and a low level of spurious reflections. It is an ideal facility for precision radiated measurements of low-level UWB

signals. We carried out the same types of spectrum and time-domain measurements using the same instrument settings as were used in the conducted measurements.

We performed a complete suite of measurements in both the time- and frequency-domains. We used the spectrum analyzer to perform swept-frequency emissions measurements at selected transmitter/receiver separations, to investigate the effects of the weather-protective radome, and to perform a series of pattern measurements in both azimuth and elevation at selected frequencies. We used both peak and average detector settings. We performed a series of zero-span, time-domain envelope measurements using the spectrum analyzer for a number of resolution bandwidth (RBW) settings at selected frequencies. In addition, we also captured full-bandwidth, time-domain waveforms at several distances using the high-speed oscilloscope. We studied the effects of two different candidate radome materials. We performed swept-frequency spectrum analyzer measurements at fixed azimuth angles using both peak and average detection.

The measurements indicate that the SLiMS system has radiated emission levels below selected NTIA and FCC emissions limits.

2 CONDUCTED EMISSIONS MEASUREMENTS

We carried out the conducted measurements by connecting the P400 radar to the signal analyzer or the oscilloscope using low-loss, precision microwave cable, using the setup shown in Figures 1 and 2. The P400 radar was connected directly to either a spectrum analyzer or a high-speed oscilloscope. Both the spectrum analyzer and the oscilloscope provide an approximate 50 Ω termination. We performed spectrum analyzer measurements over a frequency range of 1−15 GHz at resolution bandwidths of 1, 3 and 8 MHz using both peak and average detection. We performed additional measurements in the range of 3–5 GHz with resolution bandwidths of 0.1, 0.3, 1, 3, and 8 MHz. We also captured 12 GHz bandwidth waveforms with record lengths of 40 µsec and 400 msec using the oscilloscope. The results are presented in Sections 3 and 4 of this report.

The conducted measurements enable us to estimate either the time-domain waveform or the frequency-domain spectrum amplitude of the P400 radar antenna terminals. The NTIA *Manual of Regulations and Procedures for Federal Radio Frequency Management* (Red Book) [1] requires conducted measurements to estimate the emissions parameters.

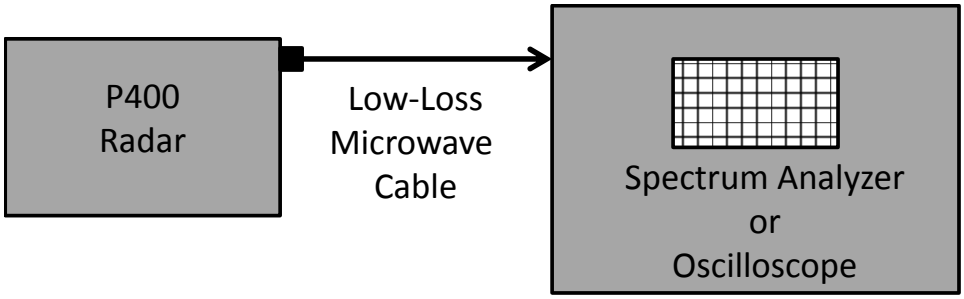

Figure 1. Schematic of the test setup for the conducted emissions measurements.

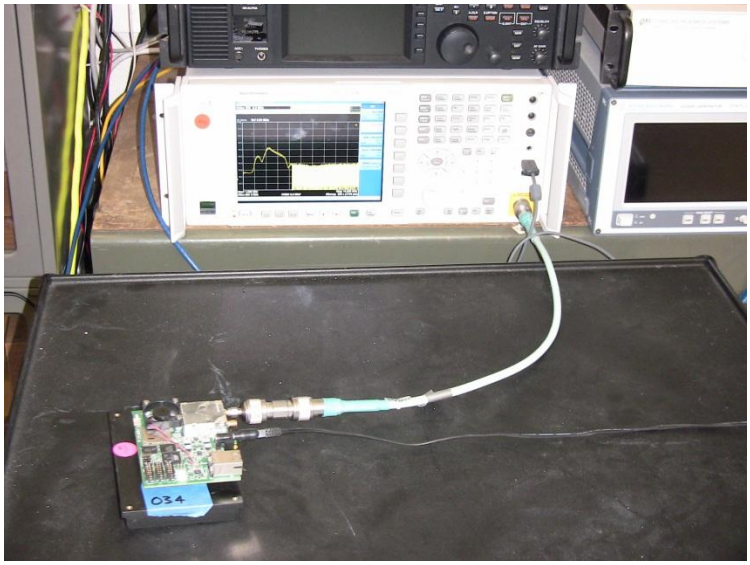

Figure 2. Conducted test setup with a spectrum analyzer.

2.1 Wideband Time-Domain Conducted Results

A thorough understanding of the time-domain character of the radar waveform is a prerequisite for the proper characterization of its spectrum properties. We used a high-speed oscilloscope with the setup as diagrammed in Figure 1 to measure the full-bandwidth waveform characteristics of the P400 radar. The signal was fed to the oscilloscope through a short section of low-loss transmission 50 Ω coaxial line. We captured two waveforms using both a high-speed and a slower-speed sampling rate. The first record was 40 μs long and was sampled at a rate of one sample per 0.625 ps in order to capture fast events and fine detail.

Figure 3 shows the fundamental wavelet that was captured in this mode. The wavelet is an oscillating sinusoid with variable amplitude and a downward chirp in frequency. The wavelet duration is approximately 2.2 ns with a peak amplitude of about 2 V. Figure 4 depicts two successive wavelets captured in the high-speed mode. The wavelets have a time separation of approximately 57.5 ns between them. We then acquired a much longer 400 ms record at a sampling interval of 0.2 μs in order to capture the global macroscopic behavior of the waveform. At this interval, the waveform was under-sampled, but its macroscopic characteristics were discernible. Figure 5 depicts two complete P400 bursts, each of which contains approximately 400000 wavelets. The duration of each burst is 24 ms, and time separation between the bursts is 0.265 seconds. It was this large-scale waveform burst behavior that dictated the spectrum analyzer settings.

We did consider trying to capture a full-fidelity P400 burst using the oscilloscope. However, capturing a 24 ms segment at one sample per 0.625 ps would have greatly exceeded the memory capacity of the oscilloscope. We therefore concentrated on the capture of partial records to understand the key waveform parameters and global waveform structure.

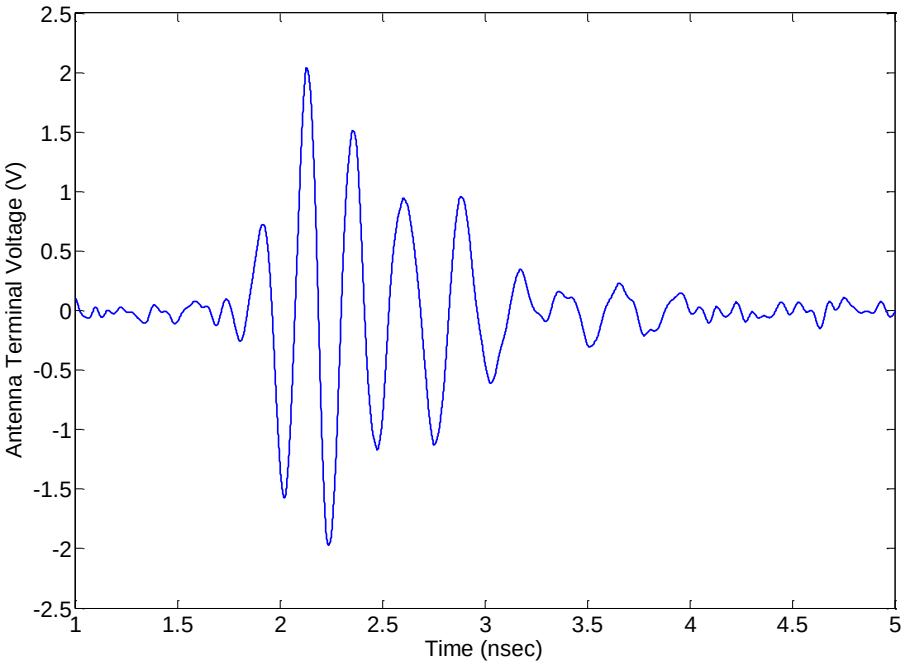

Figure 3. The fundamental SLiMS pulse waveform obtained with a high-speed oscilloscope.

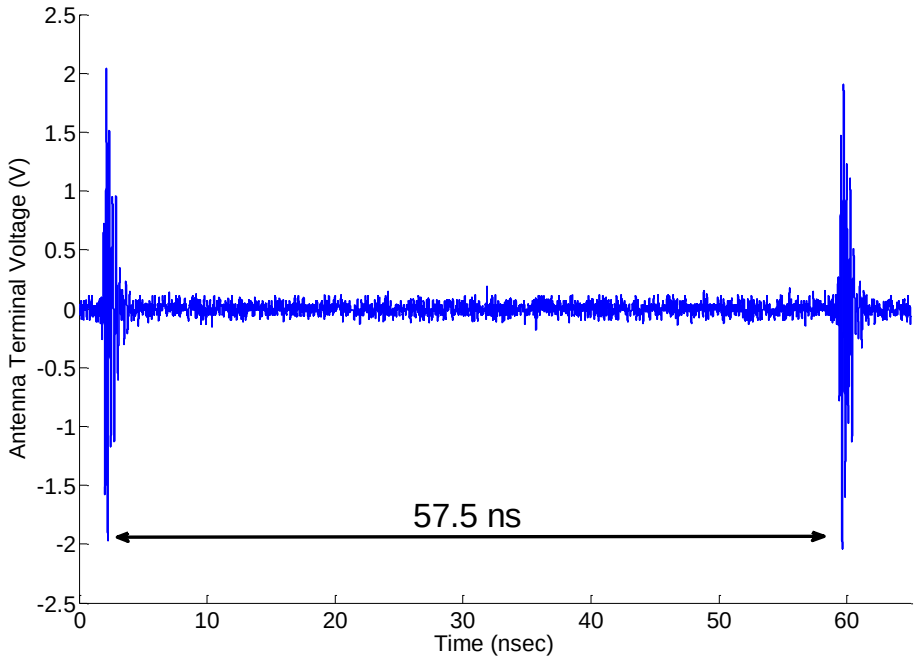

Figure 4. Interval between pulses for the P400 radar system.

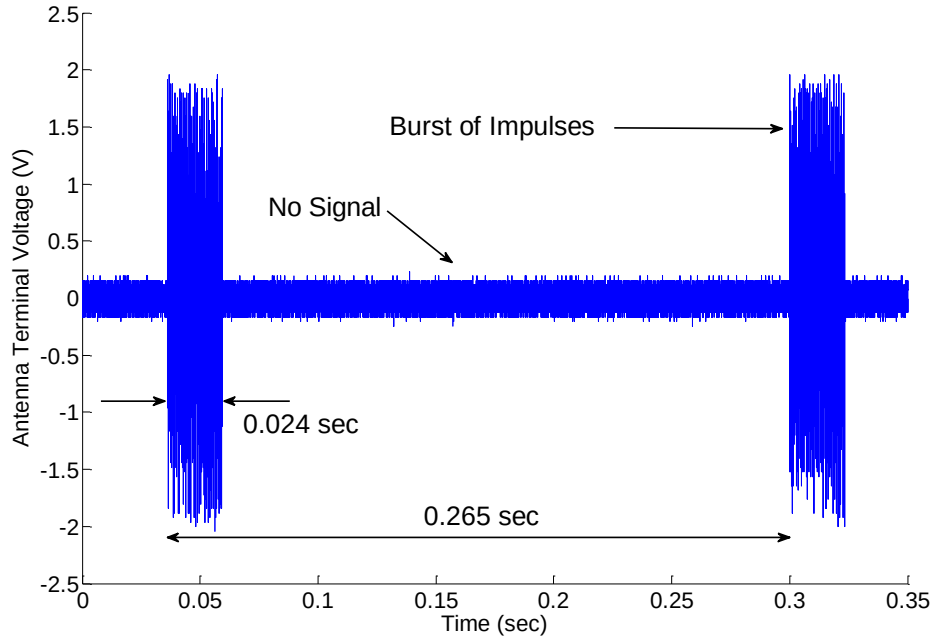

Figure 5. Burst structure for the P400 radar system.

2.2 Influence of the Number of Bursts on Swept Measurements

For the conducted measurements, we used the setup shown in Figures 1 and 2. We configured the spectrum analyzer in the swept-frequency mode. We performed measurements with both peak and average detector settings [2]–[4].

In a full deployment, the SLiMS system operates the radar modules in a time-division multiple access (TDMA) mode, and each module transmits bursts. This places special demands on the spectrum analyzer measurements. There are two conditions that must be met. First, for a given number of frequency bins (or buckets), the resolution bandwidth (RBW) must be set to match the bin width to ensure there are no gaps in the scanned frequency range. Secondly, as the spectrum analyzer sweeps across a specified frequency range, one or more bursts must be processed within a given bin during each scan.

We measured the spectrum analyzer response to the P400 signal. We set the RBW to 1 MHz and swept over the frequency range of 3000–6000 MHz. We then adjusted the sweep times to capture 1, 2, 3 and 4 TDMA bursts per spectrum analyzer frequency bin from the P400 radar. We set the sweep time to be an integer multiple of the fundamental burst period of 0.265 seconds. Table 1 summarizes the required spectrum analyzer sweep times.

Table 1. Sweep times for the spectrum analyzer study (3000–6000 MHz).

Number of Bursts	Sweep Time (sec)
1	795
2	1590
3	2385
4	3180

Figure 6 shows the peak-detected power as a function of the number of bursts. The measured results exhibit noisy behavior as a function of frequency. A steady reduction in signal variations is seen as more bursts are included in each of the frequency bins. The corresponding average-detected results are shown in Figure 7. Average detection yields much smoother results than peak detection, since all of the data within each frequency bin is averaged. In the case of peak detection, only the maximum-power point within each bin is displayed. As a tradeoff between accuracy and measurement time, we decided that measuring two bursts would provide good peak-detected results with variations on the order of 1.0–1.5 dB, and average-detected results with variations of less than 0.5 dB. The use of two bursts also resulted in sweep times that kept us within the time constraints we had on the use of the anechoic chamber.

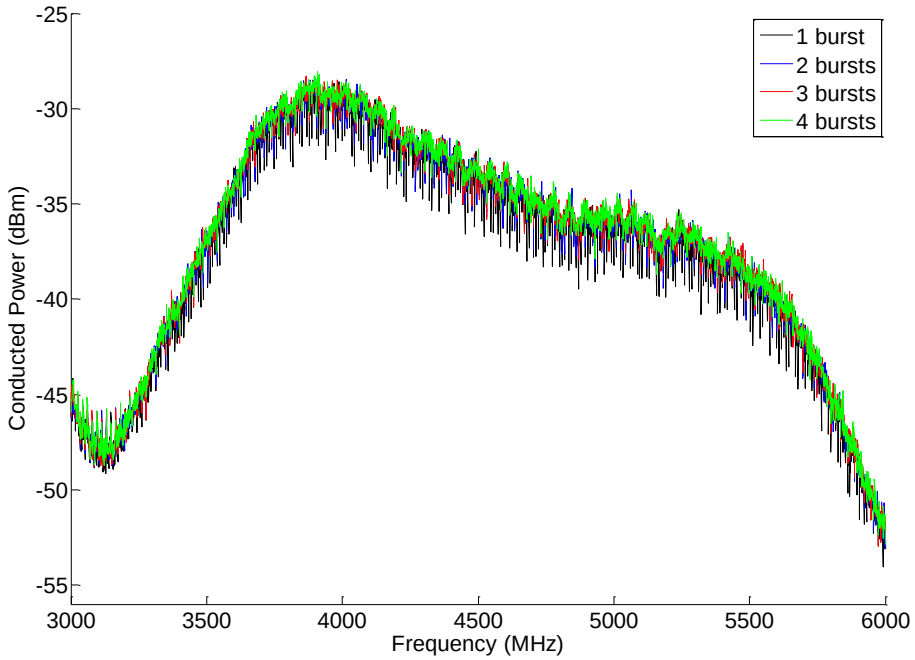

Figure 6. Conducted measurements for 1, 2, 3, and 4 bursts with RBW = 1 MHz and peak detection.

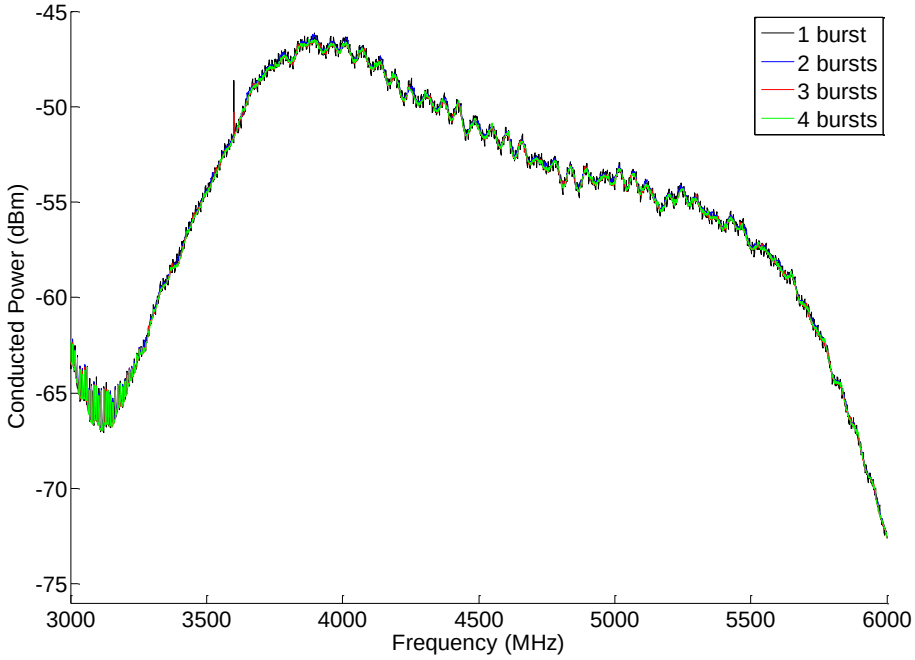

Figure 7. Conducted measurements for 1, 2, 3 and 4 bursts with RBW = 1 MHz and average detection.

2.3 Frequency-Domain Conducted Measurements

2.3.1 Spectrum Analyzer Settings

We carried out a series of conducted measurements using an Agilent 9030A PXA signal analyzer. We configured it to operate in the spectrum analyzer mode and to perform swept-frequency measurements over selected frequency ranges. We used both peak and average detection and for our measurements. In order to assess interference potential to a wide variety of systems we measured at five different resolution bandwidths: 0.1, 0.3, 1, 3, and 8 MHz. We configured the instrument to capture two bursts within each frequency bins during a sweep. This required a dwell time of 0.53 s per frequency bin during the sweep. Table 2 summarizes the required sweep times for various RBWs. The sweep time is computed from the formula

$$Sweep\ Time(sec) = \frac{Frequency\ Span\ (MHz)}{RBW\ (MHz)} \times 0.53\ . \qquad (1)$$

Equation (1) is based on a burst interval of 0.265 s and measuring two bursts in each frequency bin. The spectrum analyzer can measure up to 40000 frequency bins, and it has a maximum sweep time of 4000 s. This sweep time limitation made it necessary in some cases to subdivide the measurements into either two or four bands, depending on the range of frequencies that was needed. The total sweep times ranged from just over 2 minutes with an 8 MHz RBW to a maximum of 2 hours and 56 minutes with RBW = 100 kHz. Table 2 provides a summary of the spectrum analyzer settings that we used for this study.

Table 2. Spectrum analyzer sweep times.

Resolution Bandwidth	Frequency Range (MHz)	Number of Frequency Bins	Sweep Time (sec)
100 kHz	3000–5000	20000 (4 bands)	10600 (4 bands)
300 kHz	3000–5000	6667	3533
1 MHz	3000–5000	2000	1061
1MHz	1000–15000	14000 (2 bands)	7420 (2 bands)
3MHz	3000–5000	667	354
3 MHz	1000–15000	4667	2474
8 MHz	3000–5000	250	133
8 MHz	1000–15000	1750	930

2.3.2 Conducted Swept-Frequency Results

We performed a series of conducted measurements on the P400 radar in the swept-frequency mode using the settings shown in Table 2.

The measured data are summarized in Figures 8–11. Table 3 provides a compendium of the maximum emission frequencies and levels for the two detection modes. The maximum emission power level is denoted by P_m and the associated frequency by f_m. With a resolution bandwidth of

1 MHz, the peak emissions maximum occurs at 3935 MHz and the corresponding average emissions maximum occurs at 3942 MHz. This difference is primarily due to measurement uncertainties. The 3 dB bandwidth of the average emissions spectrum (RBW = 1 MHz) is 508 MHz. We do see case-to-case variations in the locations of the maxima, due to the combination of measurement uncertainties and the complex structure of the emissions spectrum. Smoother characteristics are seen with average detection since multiple samples are averaged within each spectrum analyzer frequency bin.

In the peak detection mode, only one sample is used in each frequency bin, resulting in larger measurement uncertainties; this results in a more "hashy" appearance. We see far less amplitude variation in the vicinity of the maximum with the 3 and 8 MHz bandwidths than at the narrower settings. The variations do increase somewhat at RBW = 1 MHz, but quickly become larger at 0.3 and 0.1 MHz. This is due to the combination of multiple periodicities of the P400 radar and the complex modulation. The finer resolution bandwidths provide more structure and detail. The wider resolution bandwidths incorporate more spectral lines, and we cannot resolve the finer spectral characteristics.

For resolution bandwidths of 1, 3 and 8 MHz, the peak emissions approximately follow a progression given by: $10\ log_{10}[RBW(MHz)]$. This is not the case at narrower bandwidths (RBW = 0.3 and 0.1 MHz) where we begin to see more features of the line spectrum. The results indicate that the combination of timing between the successive impulses and bursts, combined with a sophisticated radar modulation, generates a complicated spectral structure.

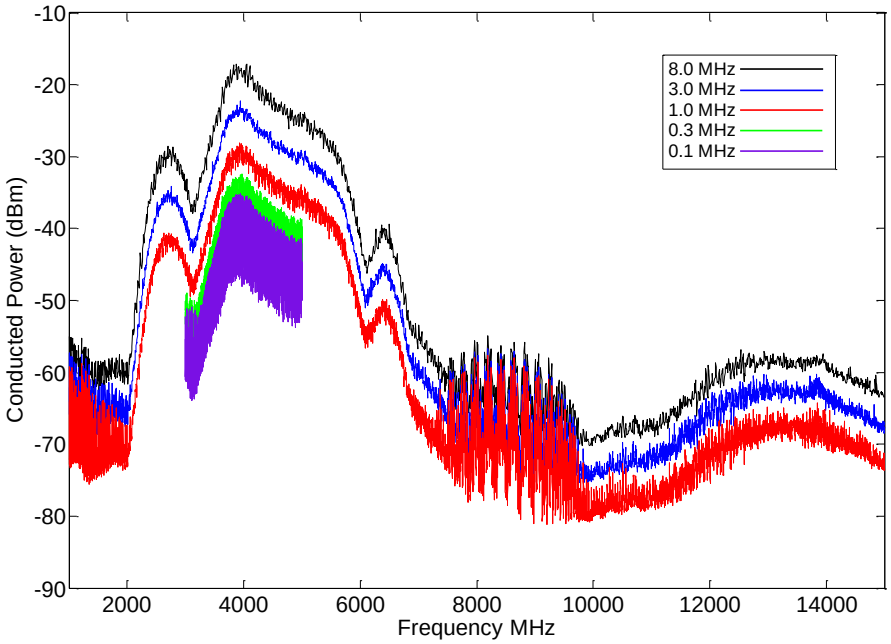

Figure 8. Peak-detected P400 radar emission levels measurements.

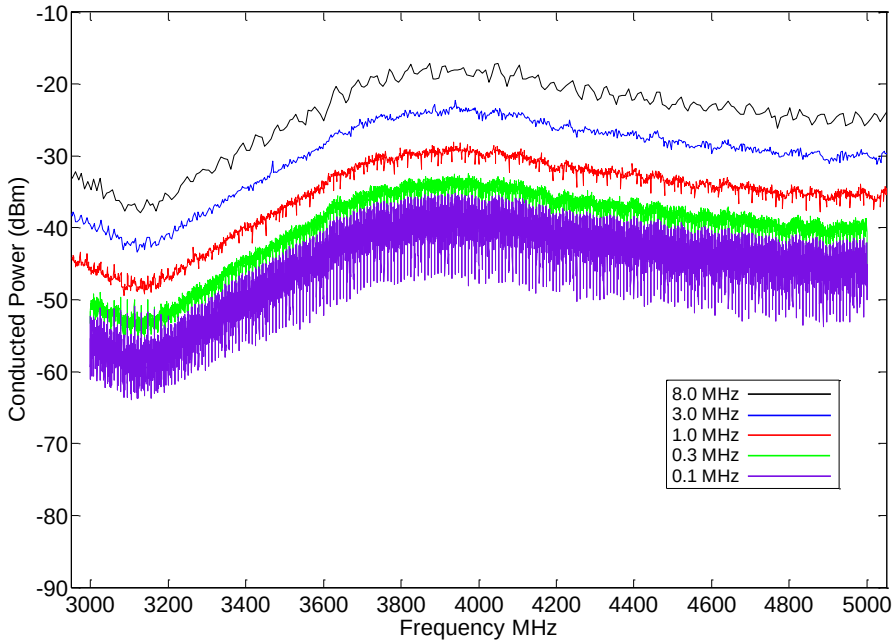

Figure 9. Peak-detected P400 radar emission levels measurements (expanded view).

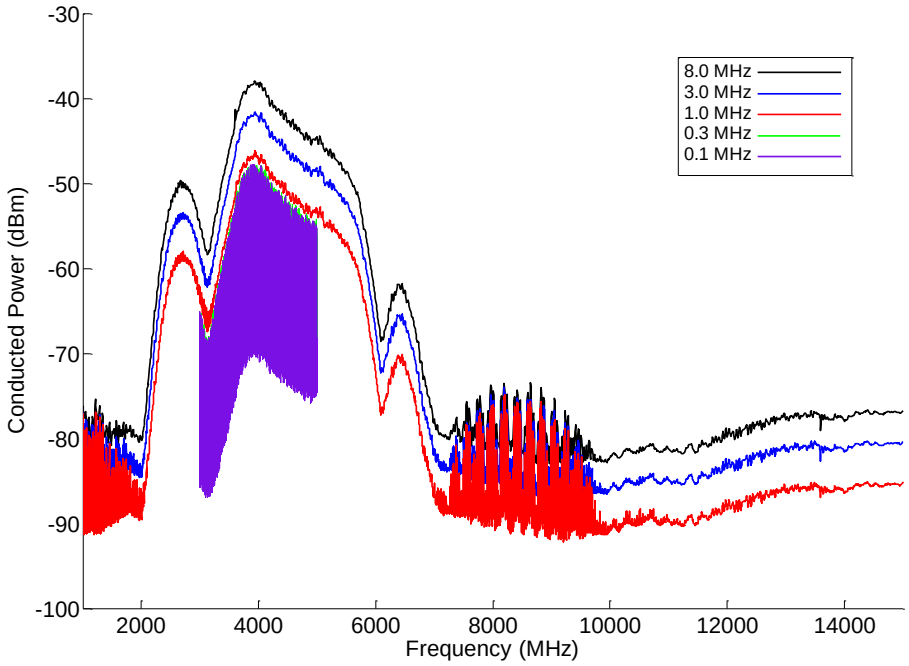

Figure 10. Average P400 radar emission levels measurements.

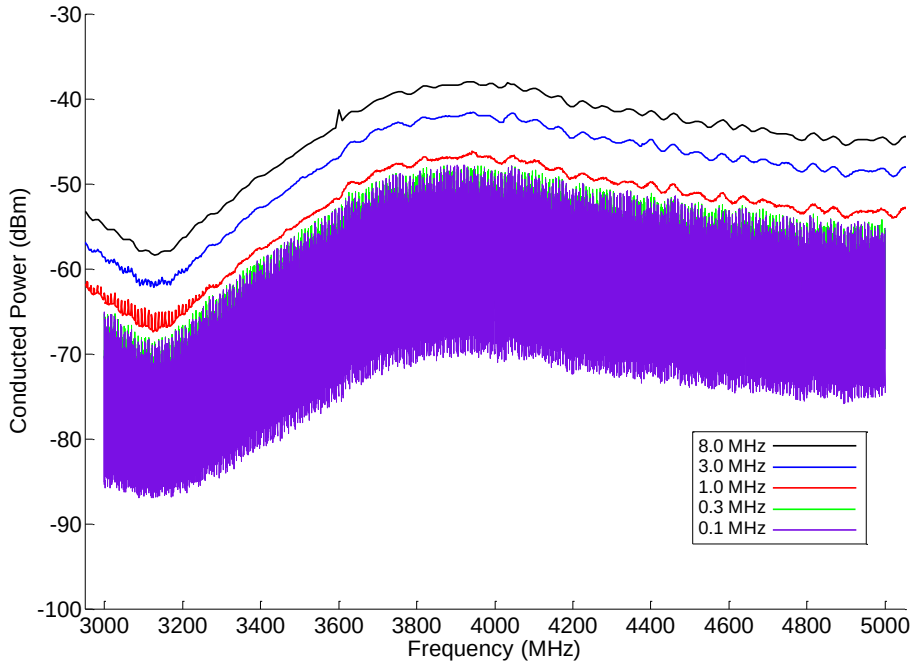

Figure 11. Average P400 radar emission levels measurements (expanded view).

Table 3. Summary of maximum peak and average emissions levels and associated peak-to-average values for P400 radar.

RBW MHz	f_{m_peak} MHz	P_{m_peak} dBm	f_{m_avg} MHz	P_{m_peak} dBm	Peak-to-average dB
8.0	3874	-17.2	3938	-38.0	20.8
3.0	3940	-22.2	3943	-41.6	19.4
1.0	3935	-28.0	3942	-46.2	18.2
0.3	3973	-32.4	3957	-47.9	15.5
0.1	3939	-35.2	3921	-47.8	12.6

2.3.3 Conducted Emissions Characteristics and Emissions Designator

We performed a detailed analysis of the conducted signal analyzer emissions data based on criteria provided in the NTIA Red Book [1]. Annex K of the Red Book defines the technical criteria for the characterization of UWB devices. Section K.3.6.8 requires that emissions measurements with a spectrum analyzer be made with RBW = 1 MHz and average detection. Section 10.8.6 of the Red Book specifies that the transmitter characteristics be measured at the antenna terminals. On this basis, we used our conducted measurements to characterize the P400 emissions and to develop an applicable emissions designator.

There are two distinct frequencies (located below and above the frequency of the emissions peak) that are a specified number of decibels below the peak level. We denote these frequencies $F_{L\_x\_dB}$ and $F_{H\_x\_dB}$ respectively. The subscript 'x' denotes a level of x dB below the maximum

(this value is typically 10, 20, or 40 dB). In addition we define a bandwidth based on these values as

$$BW_{x\_dB} = F_{H\_x\_dB} - F_{L\_x\_dB} \,. \tag{2}$$

Section K.3.6.1 of the NTIA Red Book uses the 10 dB points to define the center frequency and the fractional bandwidth of UWB devices as follows

$$F_{c\_10\_dB} = \frac{F_{H\_10\_dB} + F_{L\_10\_dB}}{2} \tag{3}$$

and

$$\Delta BW = \frac{2\left(F_{H\_10\_dB} - F_{L\_10\_dB}\right)}{\left(F_{H\_10\_dB} + F_{L\_10\_dB}\right)} \tag{4}$$

where $F_{c\_10\_dB}$ is the center frequency and ΔBW is the fractional bandwidth. Equation (4) has the additional constraint that the 10 dB bandwidth of the UWB signal must be greater than 500 MHz, which is the case for the P400 radar.

There are two additional quantities that we consider. The first is the total received signal power, which is obtained by summing the received spectrum analyzer power over all of the frequency bins, as follows:

$$P_{tot} = \sum_{f_{min}}^{f_{max}} P(f_i) \tag{5}$$

where $P(f_i)$ is the measured power in the ith frequency bin of the spectrum analyzer, and f_{min} and f_{max} denote the minimum and maximum frequency limits of the sweep.

The next quantity is the occupied bandwidth. Section 6.1.1 of the Red Book defines this as the ratio of the mean power of the signal outside of the frequency range $f_{ocL} \le f \le f_{ocU}$ to the mean power contained within this bandwidth. The selection of the lower and upper frequencies (f_{ocL} and f_{ocU}) determine the amount of signal power outside of this range.

In terms of our swept-frequency measurements over a frequency range of $f_{min} \le f \le f_{max}$, this ratio is given by

$$R_{OC} = \frac{\sum_{f_{min}}^{f_{ocL}} P(f_i) + \sum_{f_{ocU}}^{f_{max}} P(f_i)}{\sum_{f_{min}}^{f_{max}} P(f_i)}. \tag{6}$$

In an actual computation, we adjust f_{ocL} and then f_{ocU} so that each summation in the numerator is a specified fraction ($\beta/2$) of the denominator. We typically set $\beta/2 = 0.005$, so that the signal power outside of the occupied bandwidth is 1% of the total measured power ($R_{OC} = 0.01$).

Based on the low-power conducted spectrum analyzer measurements with average detection and an RBW = 1.0 MHz, the P400 radar has the following signal characteristics:

1) Location and power of the signal maximum: 3942 MHz, -46.2 dBm
2) Center frequency based on (7): $F_{c\_10\_dB}$ = 4421 MHz
3) Fractional bandwidth based on (8): ΔBW = 0.435 (43.5%)
4) 3 dB points and bandwidth: 3678 MHz, 4186 MHz, BW_{3_dB} = 508 MHz
5) 10 dB points and bandwidth: 3453 MHz, 5372 MHz, BW_{10_dB} = 1919 MHz
6) 20 dB points and bandwidth: 3180 MHz, 5878 MHz, BW_{20_dB} = 2698 MHz
7) 40 dB points and bandwidth: 2057 MHz, 5878 MHz, BW_{40_dB} = 2698 MHz
8) Occupied bandwidth $BW_{oc} = f_{ocU} - f_{ocL}$ = 3279 MHz (R_{OC} = *0.01, 0.5%* criterion)
9) Total conducted power $P_{conducted}$ = 1.95e-5 W, -17.1 dBm (average detection)

The total power is computed by summing over the measured dBm levels in each of the spectrum analyzer frequency bins. In this case, we summed over 14000 frequency bins which covered the entire 1–15 GHz range.

The emissions designator has two primary components: 1) the necessary bandwidth, and 2) the emission classification symbol. Section K.3.6.1 of the NTIA Red Book defines the necessary bandwidth as the 10 dB bandwidth which is 1919 MHz for the SLiMS signal. The first part of the emissions designator is given by 1G92 which represents the necessary bandwidth of 1.92 GHz. The emissions designator is V1D where the letter 'V' denotes pulse transmission, the number '1' denotes a single channel with digital signals, and the letter 'D' stands for data transmission. The proposed emissions designator, therefore, is 1G92V1D.

2.4 Zero-Span Spectrum Analyzer Measurements

We performed a series of conducted measurements with the spectrum analyzer set in the zero-span mode. In this mode, the frequency is fixed and data are acquired in the time-domain for three different resolution bandwidths: 100 kHz, 1 MHz and 8 MHz. We set the analyzer for peak detection, 1000 display points, and a sweep time of 0.8 s. With these settings, the spectrum analyzer displays the time-domain envelope of the signal. Since the resolution bandwidths are much smaller than the SLiMS UWB signal bandwidth, the fast waveform transitions are not seen in the slower response of the analyzer IF filter.

Figures 12–15 depict the zero-span measurements at center frequencies of 3000, 3950, 5000, and 6000 MHz. They are plotted for a 0.8 s time interval to capture three complete bursts of the radar. The results have the same global structure that we saw with the high-speed oscilloscope measurements. Once again, we see a burst width of 24 ms and a repetition rate of 0.265 s. The zero-span results are the envelope of the SLiMS waveform with little additional detail. The resulting pulse amplitudes are a function of both the RBW and the analyzer RF frequency setting. The envelope amplitudes do increase with the IF filter bandwidth, at a rate of approximately 10 $Log_{10}(BW)$. The maximum pulse amplitudes occur at 3950 MHz which is located near the frequency of the maximum emissions level.

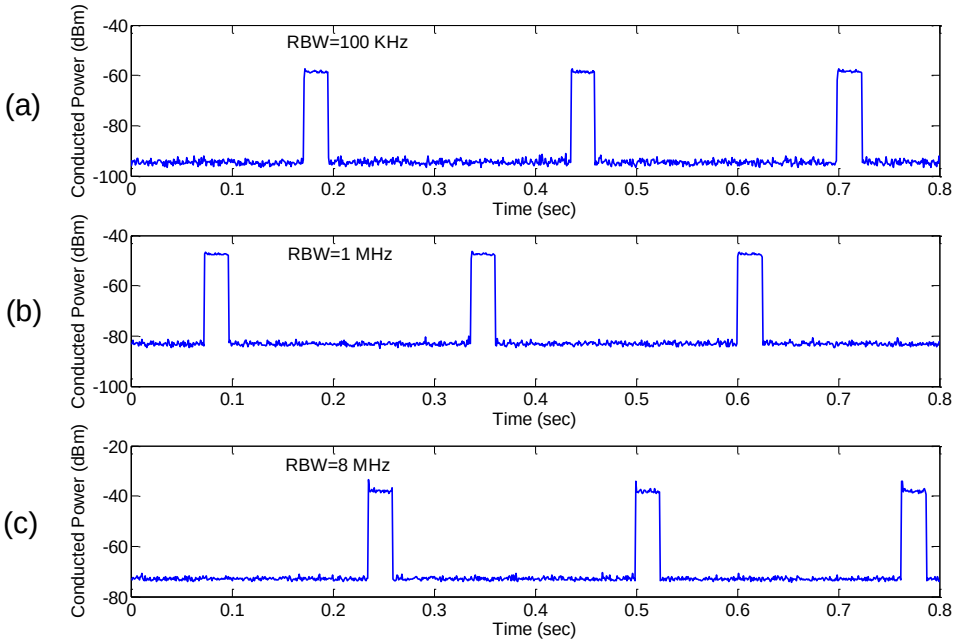

Figure 12. Zero span results obtained at 3000 MHz. (a) RBW = 100 kHz, (b) RBW = 1 MHz, and (c) RBW = 8 MHz.

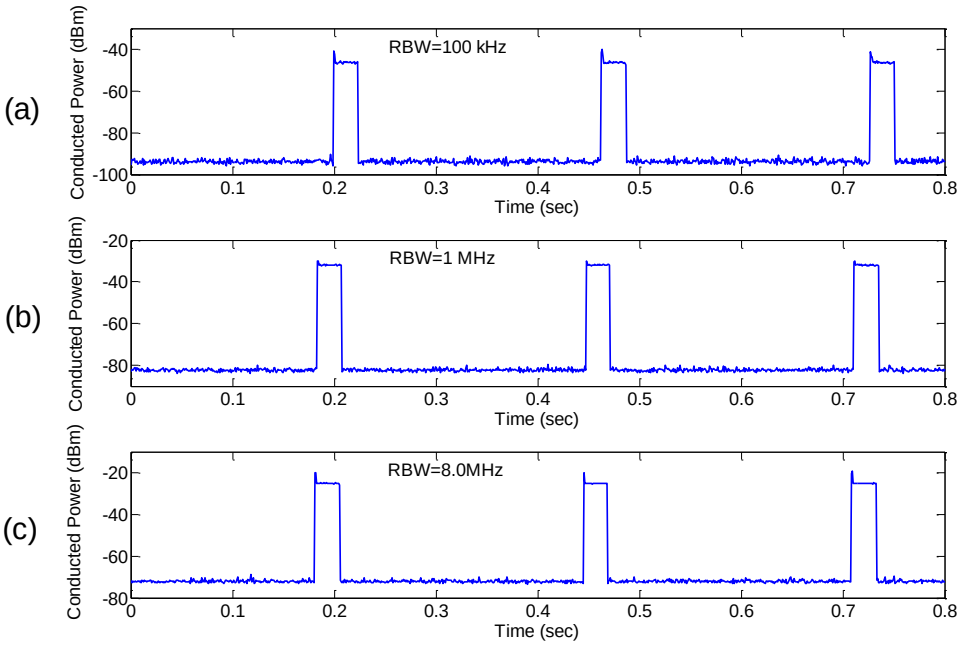

Figure 13. Zero span results obtained at 3950 MHz. (a) RBW = 100 kHz, (b) RBW = 1 MHz, and (c) RBW = 8 MHz.

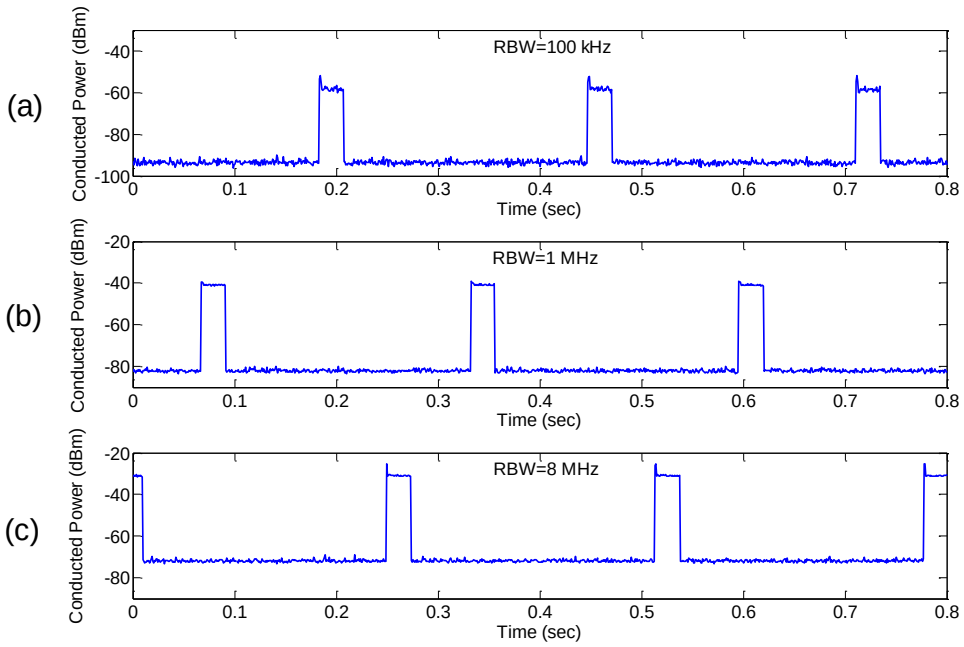

Figure 14. Zero span results obtained at 5000 MHz. (a) RBW = 100 kHz, (b) RBW = 1 MHz, and (c) RBW = 8 MHz.

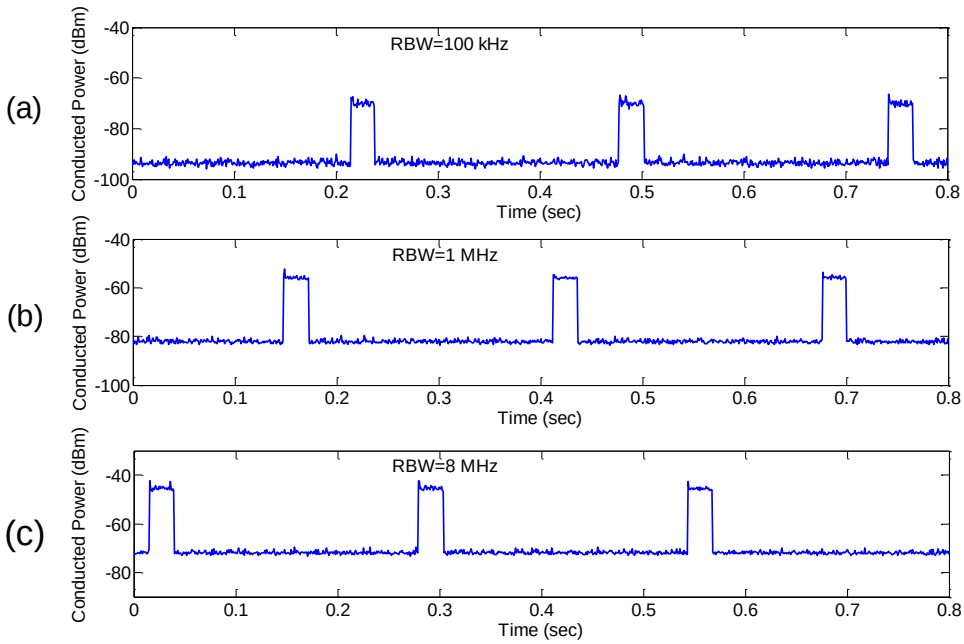

Figure 15. Zero span results obtained at 6000 MHz. (a) RBW = 100 kHz, (b) RBW = 1 MHz, and (c) RBW = 8 MHz.

3 RADIATED EMISSIONS MEASUREMENTS

3.1 Methodology and Overview

We carried out the radiated measurements inside a fully anechoic chamber, as described above. The chamber testing configuration is shown schematically in Figure 16. It was comprised of a SLiMS short pole mounted on a moveable cart, with a multiple-axis positioner and a fixed receiving system. The receiving system consisted of an antenna mounted on a fiberglass pole which, in turn, fed a signal to either an oscilloscope or a spectrum analyzer. The feed network had two coaxial cables connected in series with a low-noise amplifier (LNA). The separation, D, between the transmitting and receiving antennas was varied over the range of 2–4 m.

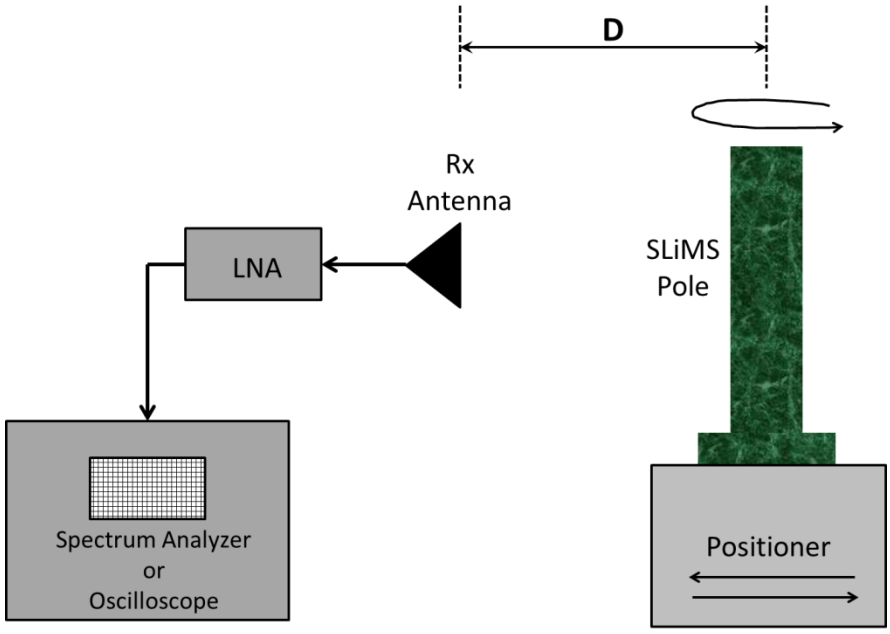

Figure 16. Test setup for radiated emissions measurements.

3.2 Antenna and Radome Configurations

We used two different receiving antennas. The first was an Antenna Research Associates (ARA) parabolic dish with a log-periodic dipole array feed shown in Figure 17. The antenna had a diameter of 91 cm and a manufacturer-specified frequency range of 1–18 GHz. We also used an Electro-Metrics dual-ridged horn (DRH) antenna shown in Figure 18, which also had an operational frequency range of 1–18 GHz. We used the two antenna types to cross-check our emissions measurements and to verify far-field conditions. However, the majority of radiated measurements were performed using the dish antenna due to its higher gain.

The receiving antenna output was fed into a MITEQ low-noise amplifier (LNA) with a nominal gain of 25 dB, a noise figure of 4.5 dB, and a specified frequency range of 1–18 GHz. We routed the LNA output to either the oscilloscope or to the spectrum analyzer using low-loss, precision microwave cables. The cable from the LNA was routed through a small aperture in the chamber

wall to the receiving equipment outside. This provided a high level of protection from ambient RF signals outside the chamber.

On the transmitting side, we installed the P400 radar inside a shortened SLiMS pole and placed it on a moveable cart with a multiple-axis antenna positioner. We used two different deployments: 1) an off-center configuration and 2) a centered configuration. The off-centered configuration, shown in Figure 17, consisted of a straight section of semi-rigid coaxial cable connected directly to a printed-circuit antenna. Due to the combination of the straight cable and the position of the transmitting port, the antenna was displaced 3.5 cm away from the geometric center of the SLiMS short pole. Since the off-center configuration exhibited significant pattern asymmetries, we also deployed the P400 antenna in the centered antenna configuration shown in Figure 18. In this case, we used a bent section of semi-rigid cable to connect the P400 to the antenna element. The outer surface of the interconnecting cable was also covered with an EMI-suppressing dielectric material to reduce common-mode currents and to maintain better pattern control. This centered configuration provided improved pattern symmetry (see Sections 3.8, 3.9, and 3.12).

We performed emissions tests with: 1) an uncovered pole (Figures 17 and 18), 2) covered with a 3 mm thick PVC plastic cylinder with a camouflaged pattern as shown in Figures 19 and 20, and 3) covered with a 7 mm thick section of black ABS plastic pipe as shown in Figure 21.

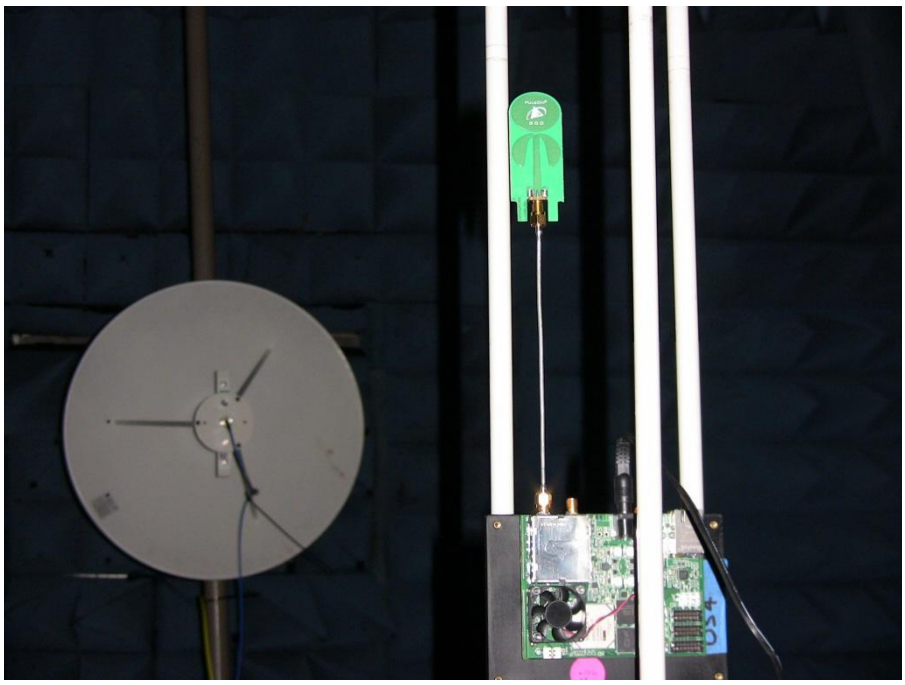

Figure 17. Off-center antenna configuration. The P400 and the printed-circuit antenna are connected by a straight section of 50 Ω semi-rigid coaxial cable.

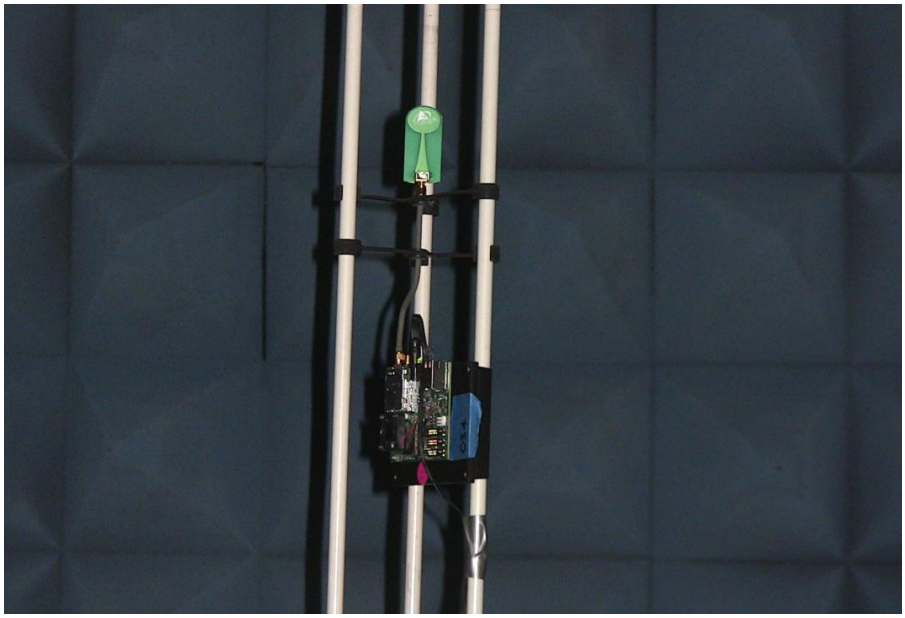

Figure 18. Centered-antenna configuration. The P400 and printed-circuit antenna are connected by a bent section of 50 Ω semi-rigid coaxial cable. The cable is covered with an EMI-suppressing jacket. The antenna is supported by a dielectric spider mount.

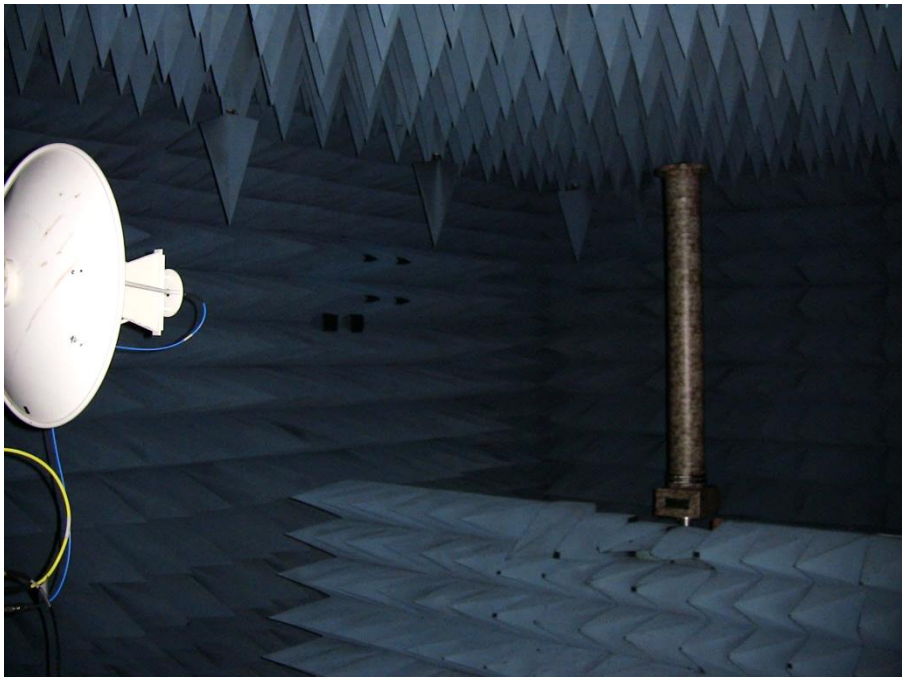

Figure 19. SLiMS pole 3 m emissions measurement setup with a dish receiving antenna.

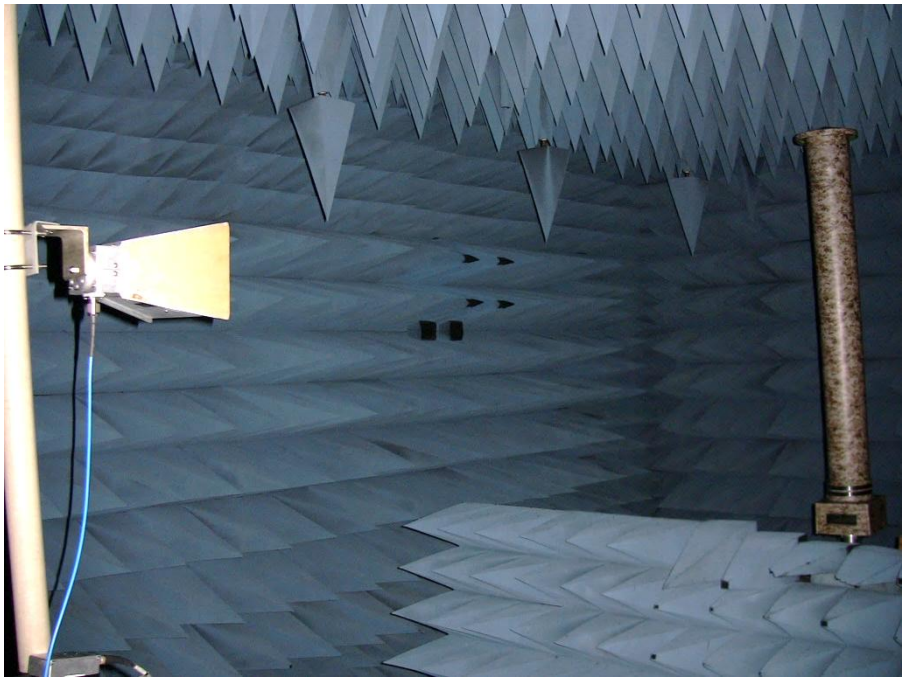

Figure 20. SLiMS pole 3 m emissions measurement setup with a DRH receiving antenna with a 3 mm thick camouflaged PVC® radome.

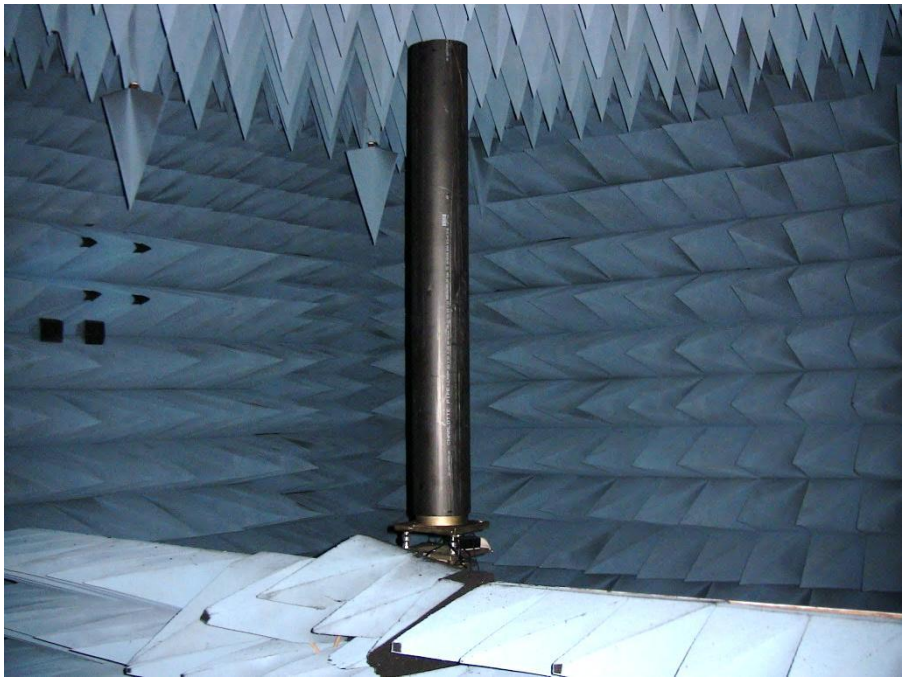

Figure 21. SliMS pole with a 7 mm thick black ABS radome.

3.3 Measurement Instrumentation

We used three instruments in the radiated emissions measurements:

- A spectrum analyzer
- A high-speed real-time digitizing oscilloscope
- A vector network analyzer for feed line and antenna calibrations

We used both the spectrum analyzer and the oscilloscope in Figure 22 to receive the radar signals. The spectrum analyzer was used for the majority of the measurements. We performed swept-frequency measurements, pattern measurements, and zero-span measurements. The spectrum analyzer settings were identical to those used in the conducted measurements (see Section 2.3.1). We used the oscilloscope in a more limited role to capture full-bandwidth time-domain waveforms and to verify the time-domain structure of the emitted waveforms

We also used the vector network analyzer (VNA) (Figure 22) to measure the insertion gain of the receiving antenna feed network that incorporated two cables and the LNA. The VNA data enabled us to convert the spectrum analyzer power readings directly to the transmitted EIRP levels. The details of this feed system calibration are described in section A.1 of Appendix A. We also used the VNA to perform the 3-antenna calibration, which is described in detail in section A.2 of Appendix A. We used three different combinations of the dish antenna and two DRH antennas to perform three insertion gain measurements between selected pairs of these antennas. The three sets of insertion data were then applied to (A.1)–(A.4) to obtain the gains as a function of frequency for each of the three antennas. The resulting antenna gains were then converted antenna factors using (A.5); the antenna relates the antenna port voltages to the incident electric field.

The feed line loss data and antenna factors were incorporated into a customized MATLAB® script, along with the measured spectrum analyzer data to compute the resulting EIRP levels.

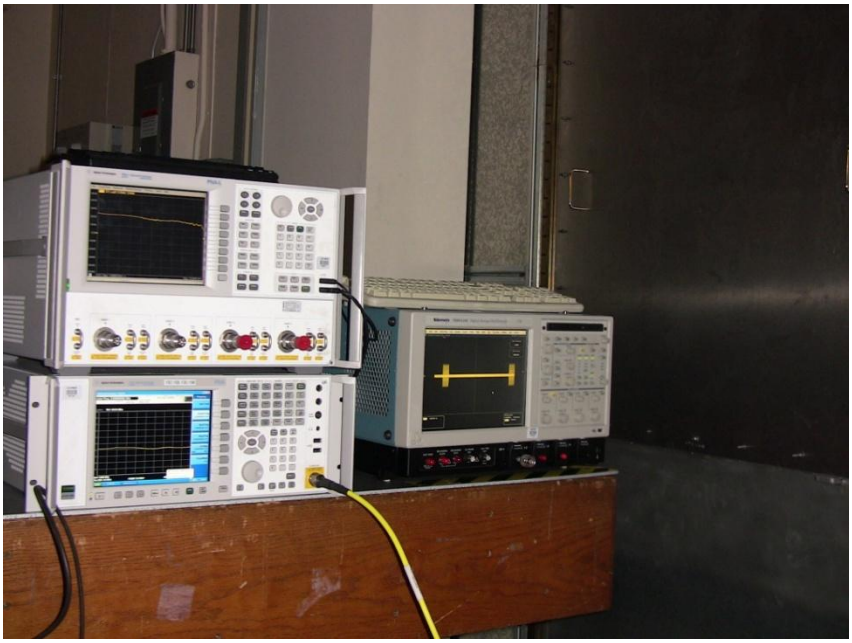

Figure 22. Test instrumentation for the radiated emissions measurements. The oscilloscope is located on the right, and the spectrum analyzer is on the bottom left. The vector network analyzer is located on the top left.

3.4 Computing EIRP from Spectrum Analyzer Readings

The key parameter in these radiated emissions was the effective isotropic radiated power [5]. The EIRP was computed from the measured spectrum analyzer data using the seven-step process shown in Figure 23. The steps incorporated a combination of both calibration corrections and theoretical calculations. The process started with the measured spectrum analyzer data. We then applied the feed network calibration and calculated the voltages at the output port of the receiving antenna. We used the antenna factor calibration data to infer the incident electric field at the antenna aperture plane. Next, we calculated the plane-wave electromagnetic power density at the aperture plane from the electric field values [6]. In the final step, we multiplied the power density by the surface area of sphere of radius D, the distance from the antenna aperture to the SLiMS antenna.

We provide a detailed analysis in Appendix B starting from fundamental equations and pertinent calibration factors. The final result of this analysis is given in (B.6).

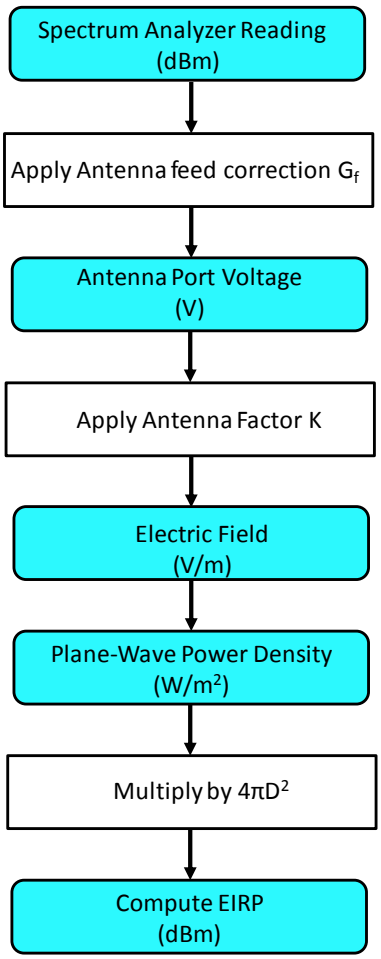

Figure 23. Flow chart for computing effective radiated power from the spectrum analyzer measurements. The pertinent electromagnetic field quantities are highlighted in color.

3.5 Overview of Measurements Performed

The primary purpose of the emissions measurements was to understand the basic radiated characteristics of the P400/SLiMS pole combination, and to compare the radiated EIRP levels with respect to FCC Part 15 [7] emission limits for UWB surveillance radars. Follow-on measurements characterized the P400 time domain and frequency domain emissions. A final series of measurements examined the impact of centering the antenna inside the short pole and the tradeoffs between two different candidate radome materials.

We performed the following measurements:

- Swept-frequency spectrum analyzer measurements (peak and average detection) at D = 3 m
- Extrapolation measurements at selected distances in the range of 2–4 m with swept-frequency measurements being performed at each separation

- Zero-span time-domain envelope spectrum analyzer measurements at selected frequencies
- 360º azimuthal patterns at selected frequencies
- 180º elevation patterns at selected frequencies
- VNA calibrations of the antennas and feed network
- Full bandwidth time-domain measurements using a high-speed oscilloscope

3.5.1 Swept-Frequency Measurements

The swept-frequency measurements constitute the primary data set that we used to characterize the SLiMS radiated emissions characteristics.

In order to ensure that our measurements were in the far field, we performed extrapolation measurements at fixed separations over the range of 2.0 m ≤ D ≤ 4.0 m, using both the dish and the DRH antennas for reception. We used two types of receiving antennas in order cross-check our results, as well as to verify both the far-field behavior and the antenna calibrations.

Figures 24 and 25 show the swept-frequency measurements for both peak and average detection and the dish receiving antenna. We show results with RBW = 1, 3 and 8 MHZ. In addition, we have included noise floor plots for these three bandwidths. The noise floor plots were obtained by turning off the P400 radar and performing swept measurements of the background noise in the closed chamber environment. The resulting noise is generated primarily by the feed system network. The noise floor exhibits approximately a $10\ log_{10}\ (RBW)$ behavior as expected for both types of detection. With the radar powered up and operating, the results become noise limited somewhere in the range of 9–10 GHz. Above this range, the measurements are dominated by noise, with no visible signal components. This effect is caused by the combination of the weak UWB signal and the much increased path loss between transmitter and receiver. The observed swept-frequency emissions have maxima at similar locations to those of the counterparts in the conducted measurements, but have steeper skirts due to the frequency-response characteristics of the P400 radar antenna.

Figures 26 and 27 depict the peak-detected SliMS emissions obtained over the five resolution bandwidths: 100 kHz, 300 kHz, 1 MHz. 3 MHz, and 8 MHz. The corresponding average results are shown in Figures 28 and 29. A summary of results for the radiated measurements is provided in Section 3.6. We provide a compendium of the frequencies and levels for the five resolution bandwidths and the two detection modes. The results obtained show similar trends to those of the conducted measurements. In the vicinity of the peak emissions, the resulting amplitudes exhibit approximately a $10\ log_{10}\ (RBW)$ variation for RBW=1, 3, and 8 MHz. The amplitude spectra once again become “hashy” at resolution bandwidths less than 1 MHz due to the complex waveform structure of the of the SLiMS signal. The frequencies at which the maxima occur differ from those of conducted case. We attribute this to the combination of antenna transmission characteristics and uncertainties in the measurements.

Figures 30–33 show the swept frequency peak and average EIRP values for D = 2, 3 and 4 m. Figures 30 and 32 show results obtained with the dish antenna, while Figures 31 and 33 contain the corresponding results using the DRH antenna. In the case of the DRH antenna, the EIRP

results nearly overlay, which indicates that we have achieved a far-field condition with both the DRH and SLiMS antennas. We see a deviation from this condition at D = 2 m for the dish antenna. This was because the dish antenna was not in the far field. The dish results, however, did converge at D = 3.0 m and 4.0 m, indicating that far-field conditions were satisfied at these separations. The results do indicate that the measurement antenna was in the far field of the SLiMS transmitting antenna for all distances $D \geq 2.0$ m.

We sent both our far-field measurement findings and the data we obtained with RBW = 1 MHz and averaging to the EMC analysis team at the Naval Surface Warfare Center (NSWC-Dahlgren, VA); they used the data in their hazards of electromagnetic radiation to ordinance (HERO) analysis [8].

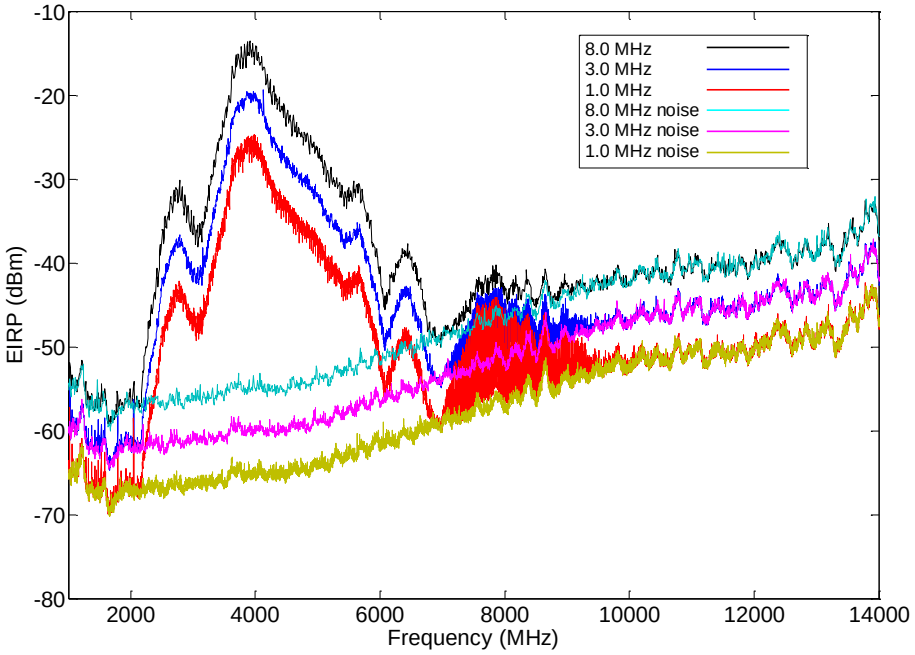

Figure 24. Swept-frequency P400 and noise floor measurements with a dish receiving antenna at D = 3.0 m, peak detection, and RBW = 1, 3, and 8 MHz.

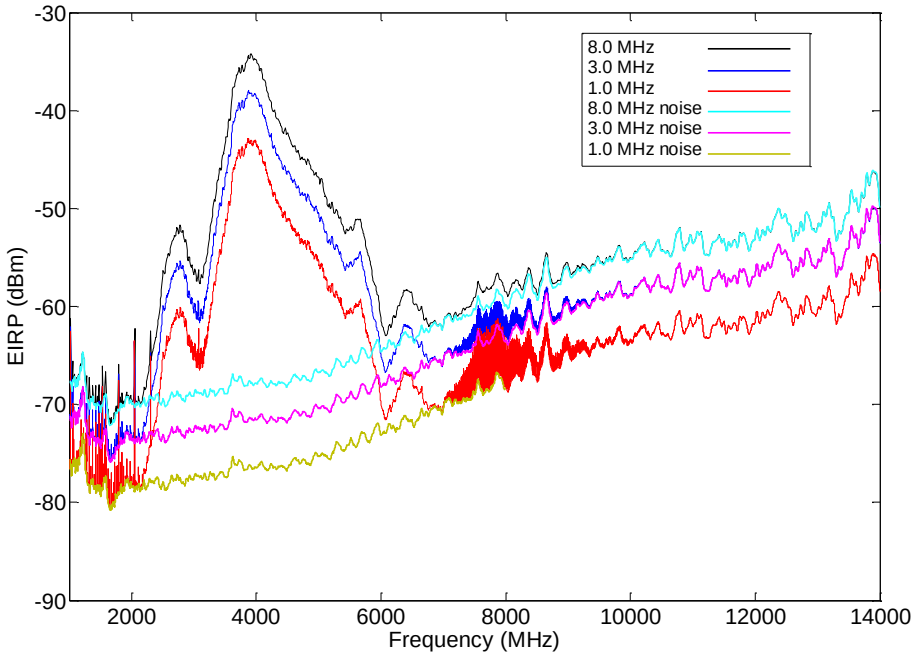

Figure 25. Swept-frequency P400 and noise floor measurements with a dish receiving antenna at D = 3.0 m, average detection, and RBW = 1, 3, and 8 MHz.

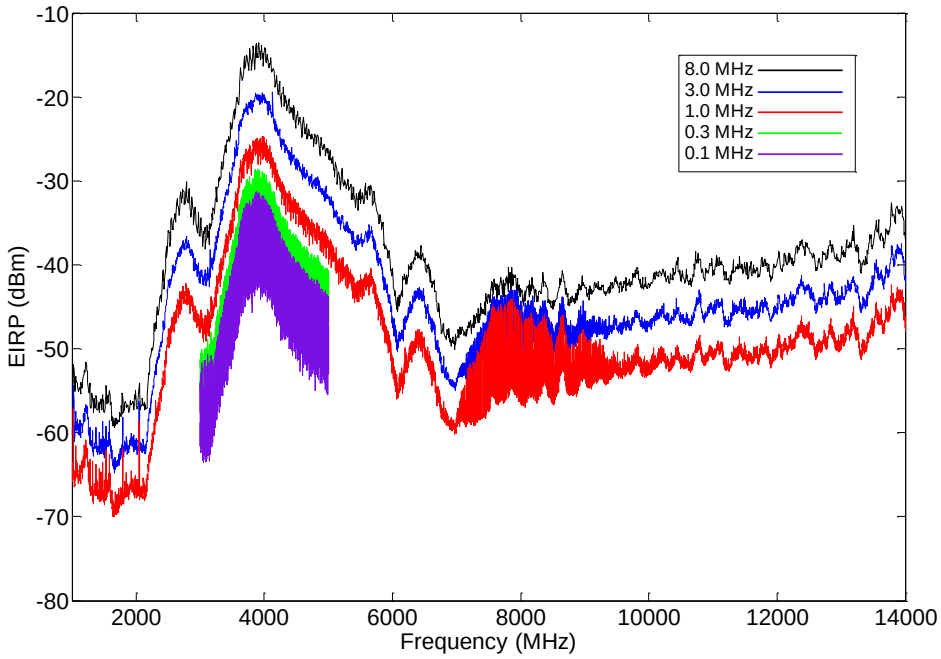

Figure 26. Swept-frequency P400 measurements with a dish receiving antenna at D = 3.0 m, peak detection, and RBW = 0.1, 0.3, 1, 3 and 8 MHz.

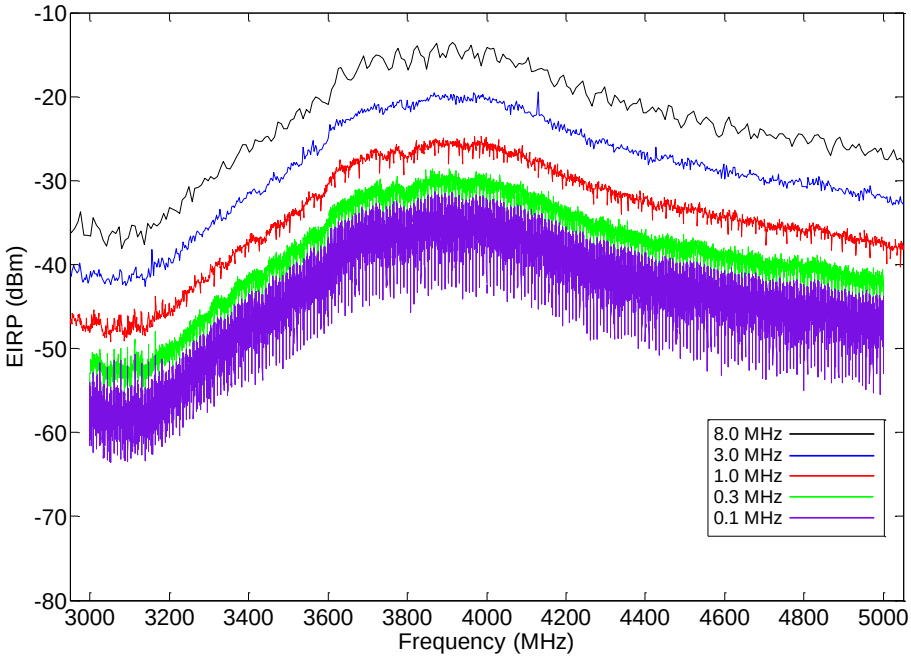

Figure 27. Swept-frequency P400 measurements with a dish receiving antenna at D = 3.0 m, peak detection, and RBW = 0.1, 0.3, 1, 3, and 8 MHz (expanded view).

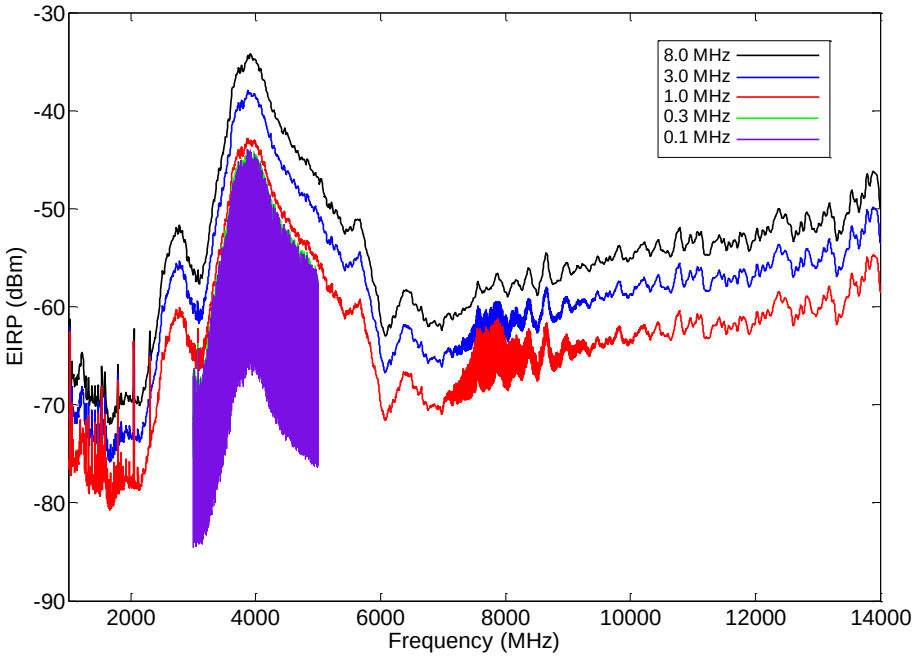

Figure 28. Swept-frequency P400 measurements with a dish receiving antenna at D = 3.0 m, average detection, and RBW = 0.1, 0.3, 1, 3, and 8 MHz.

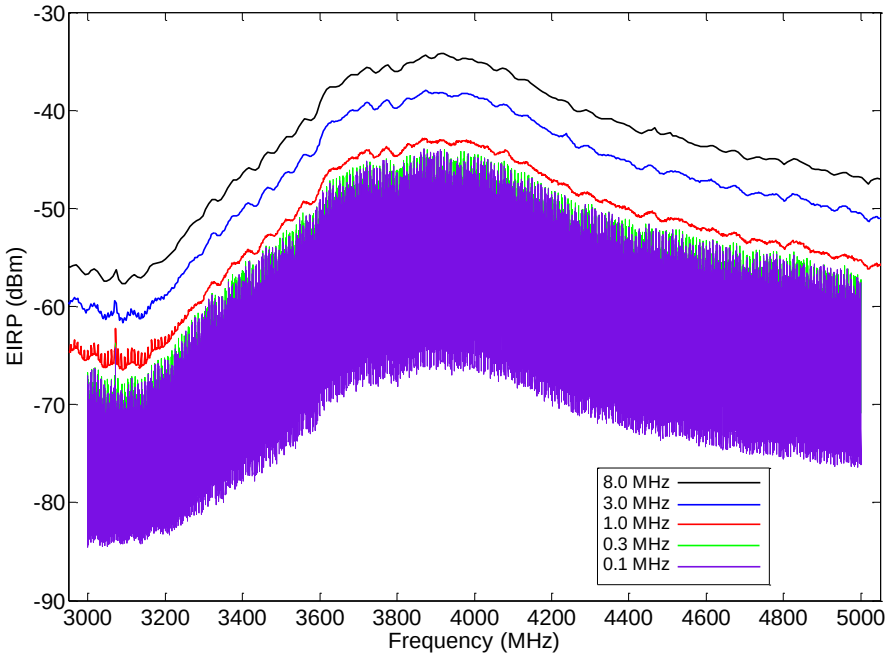

Figure 29. Swept-frequency P400 measurements with a dish receiving antenna at D = 3.0 m, average detection, and RBW = 0.1, 0.3, 1, 3, and 8 MHz (expanded view).

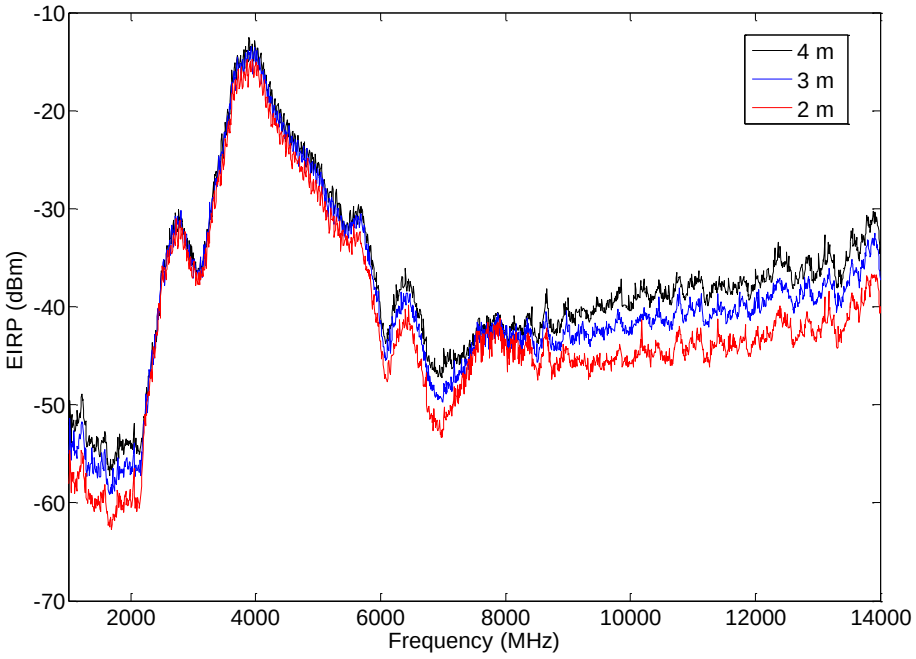

Figure 30. Peak-detected EIRP (RBW = 8.0 MHZ) swept-frequency results obtained at D = 2.0, 3.0, and 4.0 m with a dish receiving antenna.

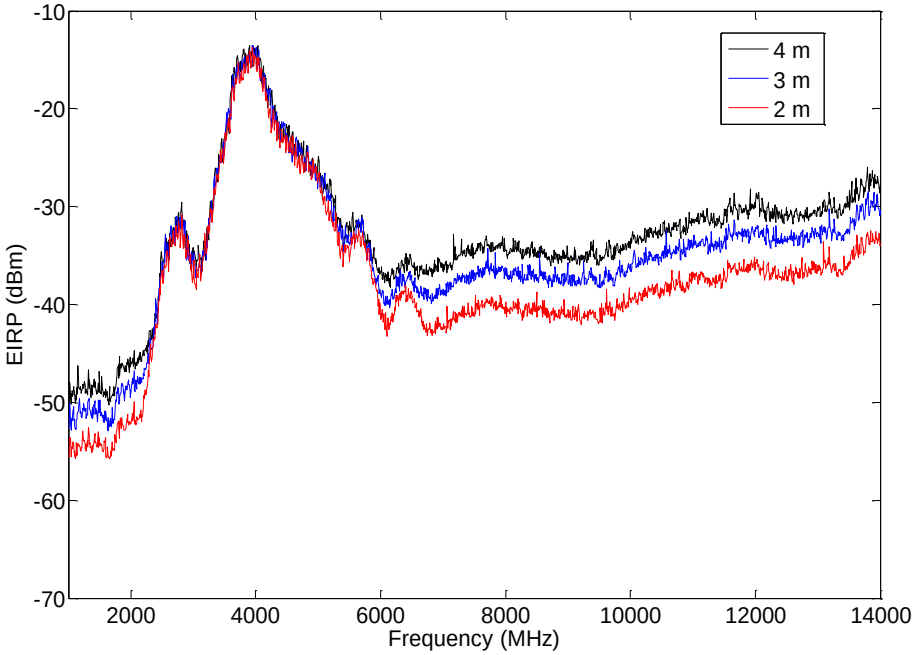

Figure 31. Peak-detected EIRP (RBW = 8 MHZ) swept-frequency results obtained at D = 2.0, 3.0, and 4.0 m with a DRH receiving antenna.

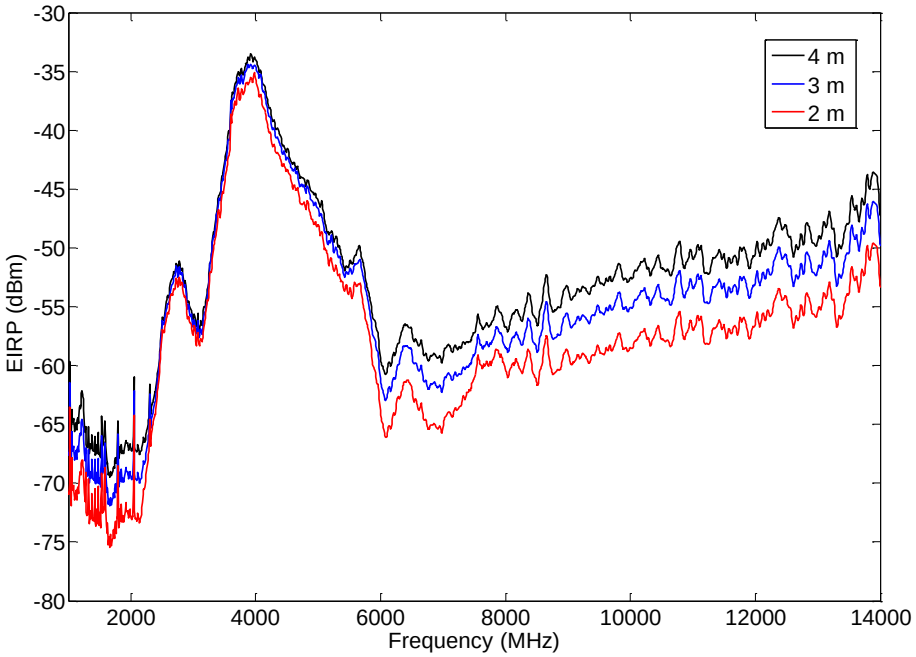

Figure 32. Average detected EIRP (RBW = 8 MHZ) swept-frequency results obtained at D = 2.0, 3.0, and 4.0 m with a dish receiving antenna.

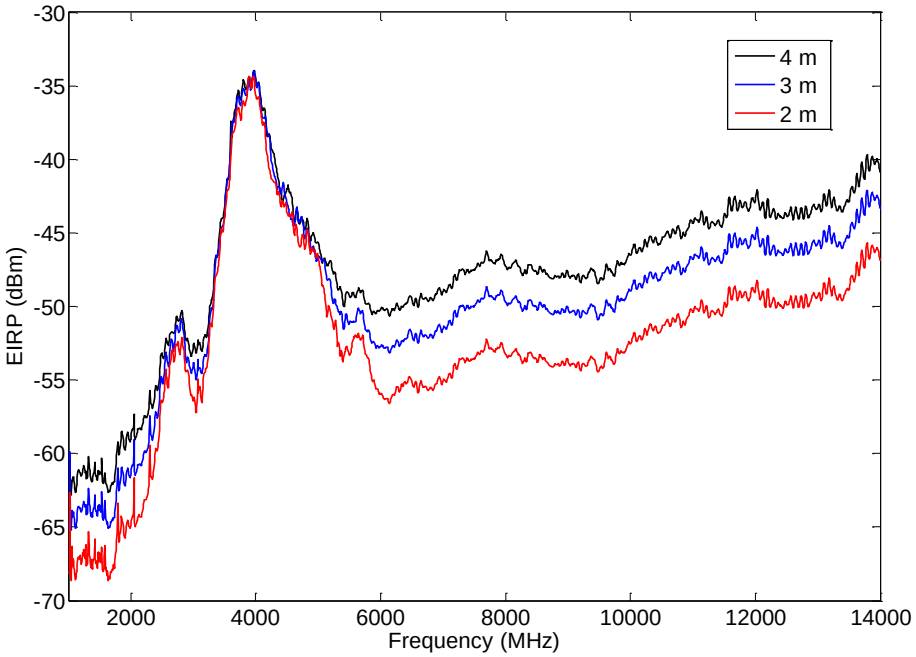

Figure 33. Average detected EIRP (RBW = 8 MHZ) results obtained at D = 2.0, 3.0, and 4.0 m with a DRH receiving antenna.

3.6 Radiated Emissions Characteristics

We now analyze the radiated emissions characteristics of the SLiMS radar emissions. Our discussion parallels that of section 2.3.3. Our calculations are once again carried out on the data obtained with RBW = 1 MHz, average detection, and an antenna-to-antenna separation of D = 3 m. In this case, we perform the calculations on the measured EIRP quantities.

Based on these measurements, the P400 radar has the following radiated emissions signal characteristics:

1) Location and power of the signal maximum: 3871 MHz, EIRP = -42.9 dBm
2) Center frequency based on (3): $F_{c\_10\_dB}$ = 4064 MHz
3) Fractional bandwidth based on (4): ΔBW = 0.285 (28.5%)
4) 3 dB points and bandwidth: 3653 MHz, 4149 MHz, BW_{3_dB}= 496 MHz
5) 10 dB points and bandwidth: 3484 MHz, 4644 MHz, BW_{10_dB}= 1160 MHz
6) 20 dB points and bandwidth: 3221 MHz, 5778 MHz, BW_{20_dB}= 2557 MHz
7) 40 dB points and bandwidth: not measureable
8) Occupied bandwidth $BW_{oc} = f_{ocU} - f_{ocL}$ = 3132 MHz (R_{OC} = 0.01, 0.5% criterion)
9) Integrated EIRP=3.14e-5 W, -15.0 dBm

The fractional bandwidths and 3, 10, and 20 dB bandwidths are narrower than the corresponding conducted quantities due to the band pass characteristics of the SLiMS radar antenna. We computed the occupied bandwidth using (5) and (6), but this time we set $f_{max} = 10\ GHz$ since the signal is noise limited above this frequency.

The EIRP and conducted power are related by the expression [5]:

$$EIRP(dBm) = P_T\,(dBm) + G_{slims}(dBi) \tag{7}$$

where P_T is the conducted power and G_{slims} is the boresight gain of the SLiMS antenna. We can use (7) as wellness check of our measurements. At 3950 MHz, we have an EIRP of -43.5 dBm (Figure 25) and a conducted power level of -46.4 dBm (Figure 10). Applying these results to (7) obtains

$$EIRP(dBm) - P_{conducted}(dBm) = 2.9\ dBi\ . \tag{8}$$

The low-gain result of (8) is reasonable, given the dipole-like pattern characteristics of the SLiMS antenna in this frequency range. The SLiMS radiation pattern characteristics are treated in detail in sections 3.10 and 3.13.

3.7 Comparisons with Selected NTIA and FCC Emissions Limits

We compared our swept-frequency measured data to the following NTIA- and FCC-specified limits (In all cases we used RMS averaging with RBW = 1.0 MHz as required by NTIA [1]): and the FCC.

- Part 15 surveillance radar emissions limits in the 1000–14000 MHz frequency range
- Part 15 limits at the GPS L1 and L2 frequencies in the 1–2 GHz frequency range
- Part 15 limits in the radio astronomy band 4990–5000 MHz
- NTIA 01-43 maximum EIRP limits and FCC Part 15 limits in the 4200–4400 MHz radar altimeter band

Figure 34 directly compares our measured results to the FCC UWB mask for surveillance radar systems [9] over the 1000–14000 MHz frequency range. The levels fall 2 dB or more below the limits near the emissions peak. The margins are even larger outside this frequency range. The same intercomparison is shown in Figure 35 for the 1000–2000 MHz frequency range which contains the notches for GPS L1 and L2 frequencies. The margins in this case are in excess of 5−10 dB throughout this frequency range. The UWB mask and NTIA 01–43 [10] protection levels are shown in Figure 36. The SLiMS emissions levels are more than 55 dB below the NTIA 01-43 protection levels. The measured emissions are 3 dB or more below the UWB emissions mask. Figure 37 compares the FCC UWB mask and the measured data in the 4900–5100 MHz band. The margin seen in the radio astronomy band (4990–5000 MHz) is greater than 14 dB. The SLiMS system emissions fall comfortably below these limits.

The key conclusions of our comparisons with selected NTIA/FCC EIRP limits are:

- The SLiMS system emissions fall below the FCC Part 15 UWB mask over the entire measured frequency range of 1–14 GHz
- The SLiMS emissions are well below the FCC Part 15 UWB limits in both the GPS L1 and L2 bands

- The FCC UWB mask is 55 dB lower than the NTIA 01-43 maximum EIRP protection level in the radar altimeter band (4200–4400 MHz), and our measured results are several dB or more below the FCC mask.
- A margin of 14 dB or more is seen in the radio astronomy band (4990–5000 MHz)

One thing that we should point out is that the emission levels from the SLiMS system are quite low. As we have already described, a combination of an anechoic chamber, sensitive measurement equipment, and precision positioning equipment are required to "see" and quantify these UWB emissions. It is unlikely that SLiMS emissions could be measured to any degree of accuracy or even seen in any other environment, since noise and ambient interference would swamp out the emissions.

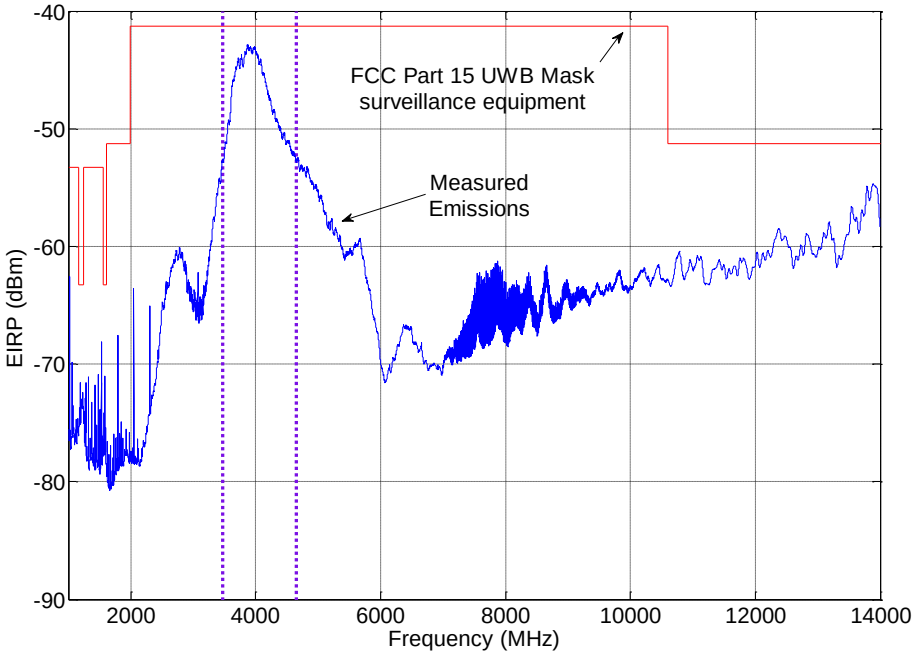

Figure 34. A comparison of ITS measurements (RBW = 1.0 MHz and average detection) and the FCC Part15 UWB mask for surveillance equipment.

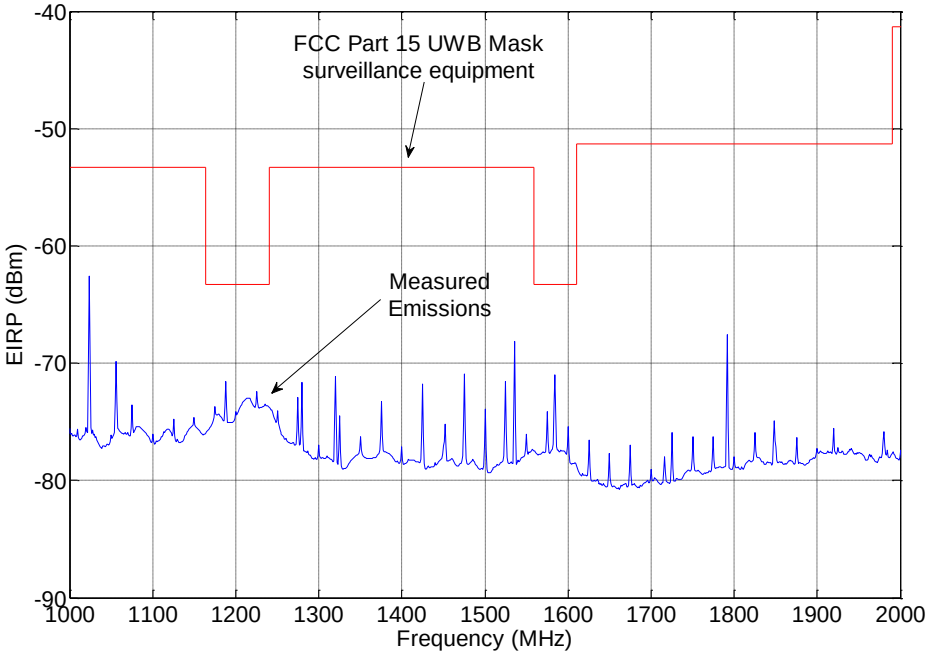

Figure 35. A comparison of ITS measurements (RBW = 1.0 MHz and average detection) and the FCC UWB mask for surveillance equipment in the 1000–2000 MHz frequency range.

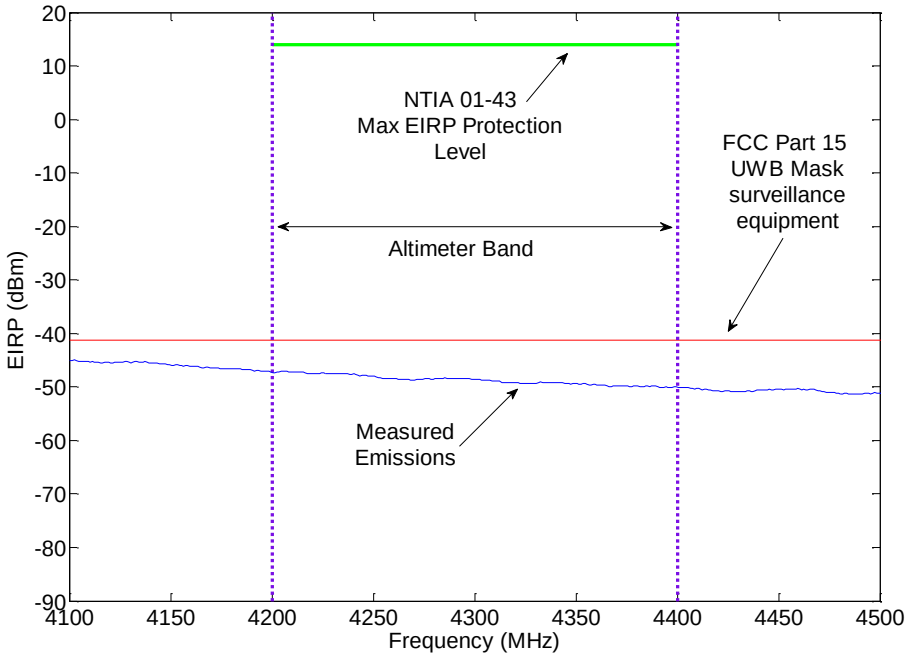

Figure 36. A comparison of ITS measurements (RBW = 1.0 MHz and average detection) and the FCC UWB mask for surveillance equipment in the 4100–4500 MHz band.

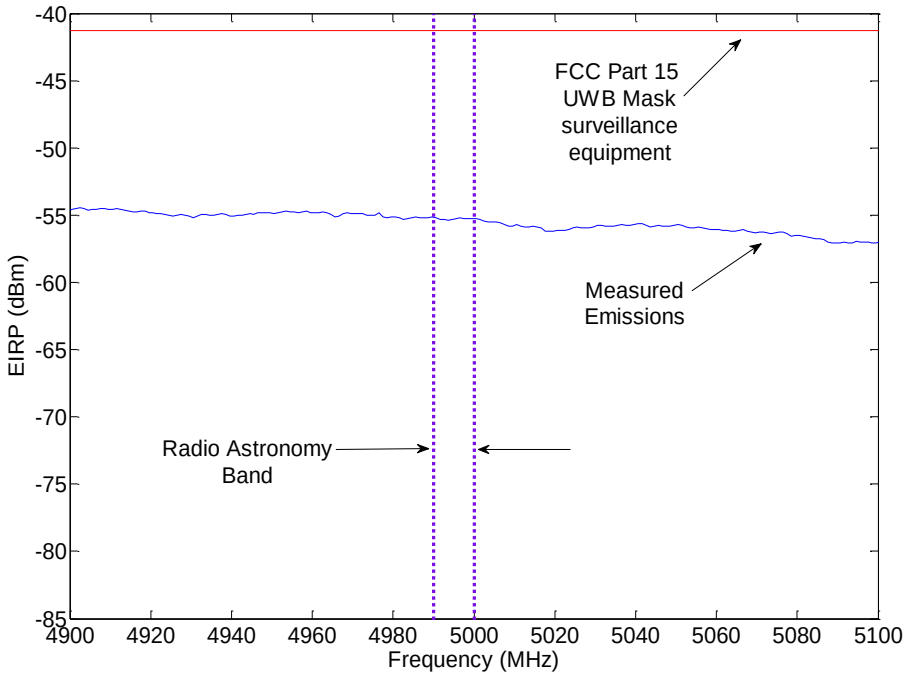

Figure 37. A comparison of ITS measurements (RBW = 1 MHz and average detection) and the FCC UWB mask for surveillance equipment in the 4900–5100 MHz frequency range.

3.8 Radome Measurements-I

We carried out a set of swept-frequency emissions measurements in order to assess the impact of the PVC radome. We bore sighted the P400 antenna at the dish antenna using the fixed configuration shown in Figure 17. The spectrum analyzer was configured to perform swept frequency measurements from 1–14 GHz. The first data set was obtained with an uncovered SLiMS short pole, and the second was obtained with the camouflaged PVC radome that is shown in Figure 19. The pole position remained unchanged during both sets of measurements to provide maximum sensitivity.

The results are shown in Figures 38 and 39. We clearly see the effects of the radome. Over some frequency ranges, the emissions levels with the cover on are higher than with the cover removed. This effect can be most clearly seen in the averaged results of Figure 39. In a frequency range of approximately 3900–4600 MHz, the emissions levels without the cover are actually lower than those with the cover. Above 4700 MHz and below 3500 MHz, this trend reverses.

The results highlight two issues. First, the radome losses are small. If the losses in the PVC were large, the emissions levels would be consistently be lower than those of the uncovered case. Second, the electromagnetic behavior of the pole is complex, with multiple scattering that results in constructive and destructive interference. A complex model is needed to predict the emissions levels.

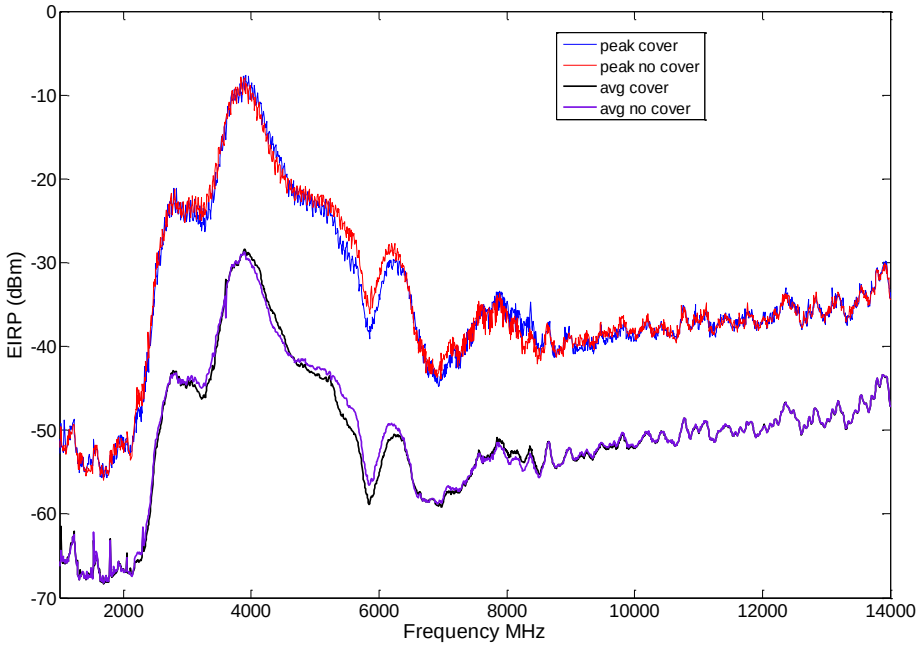

Figure 38. Intercomparisons of peak and average detected emissions (RBW = 8 MHz) with and without the PVC radome.

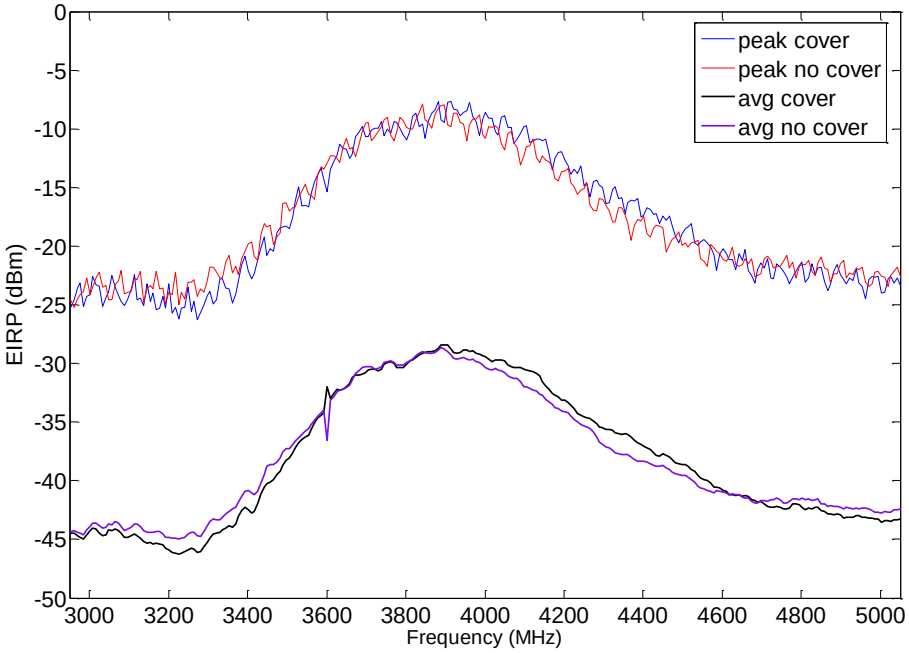

Figure 39. Intercomparisons of peak and average detected emissions (RBW = 8 MHz) with and without the PVC radome (expanded view).

3.9 Azimuth and Elevation Patterns

We performed a series of pattern measurements in the azimuth and elevation planes. We configured the spectrum analyzer in the zero-span mode with peak detection and resolution bandwidth of 1 MHz and a 1001 point sweep. The azimuthal setup is shown in Figure 19 at a 3 m separation. We rotated the SLiMS short pole over the range of 0°–360° at an angular velocity of 5°/sec. The sweep rate of the spectrum analyzer was set at 72 seconds which synchronized it with the rotation rate of the pole. We mounted the SLiMS pole horizontally using the test setup shown in Figure 40. The reasons for this were twofold: 1) we needed a balanced configuration to avoid overstressing the antenna positioner, and 2) this setup permitted us to perform the pattern measurements using only one axis of angular motion, greatly simplifying the measurement. We rotated the pole from the 0° position of Figure 40 counterclockwise to an angle of 180°. Thus the scan progresses from one horizon, over the top of the pole, to the opposite horizon. We adjusted the sweep rate of spectrum analyzer to 36 seconds since the sweep was only half as long as before. All of the other spectrum analyzer settings remained unchanged.

We performed the pattern measurements at 3000, 3950, 5000 MHz. Figures 41–52 show pairs of azimuth and elevation patterns at these frequencies. For each frequency, we present the azimuth and then elevation patterns sequentially in rectangular and polar form. The pattern characteristics exhibit different functional behaviors for each frequency. The patterns do show significant variations, which is due to: 1) the presence of the three dielectric support posts, 2) the PVC radome, and 3) the off-center transmitting antenna.

Figure 40. Elevation pattern measurement setup in the anechoic chamber.

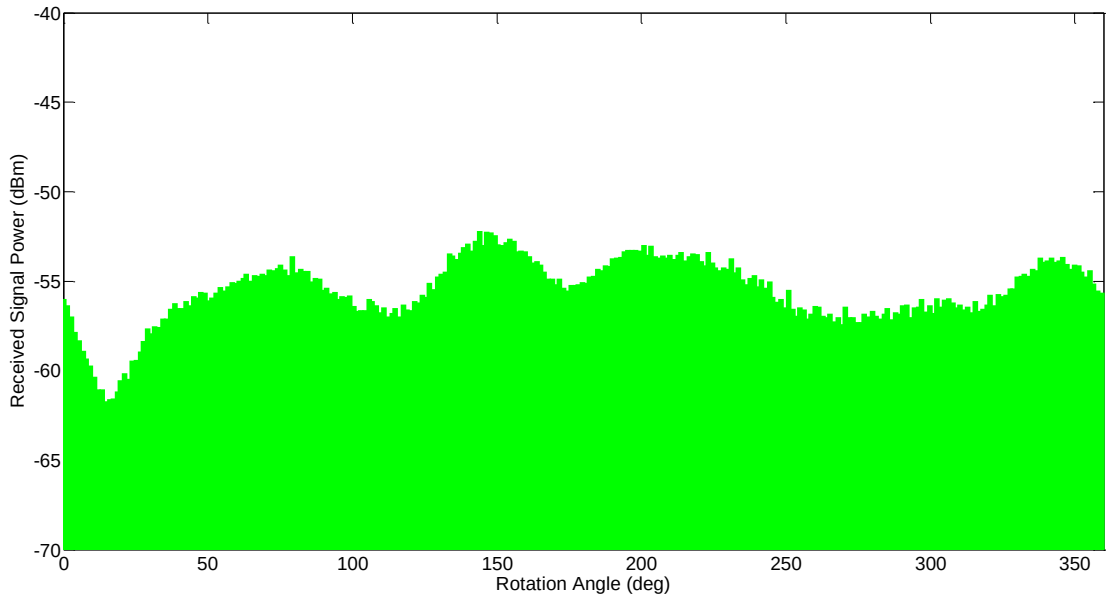

Figure 41. Azimuth pattern of the SLiMS short pole at 3000 MHz (peak detection and RBW = 1 MHz).

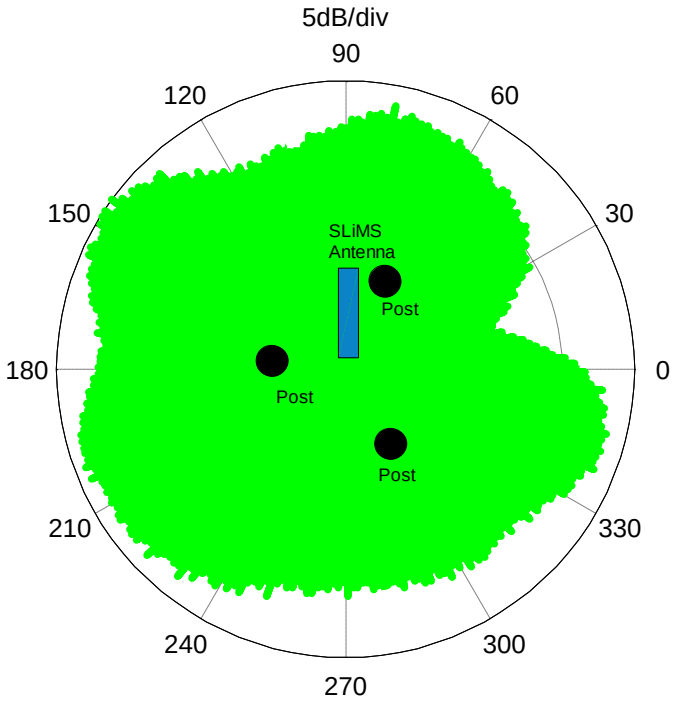

Figure 42. Polar azimuth plot (top view) of the SLiMS short pole emissions at 3000 MHz.

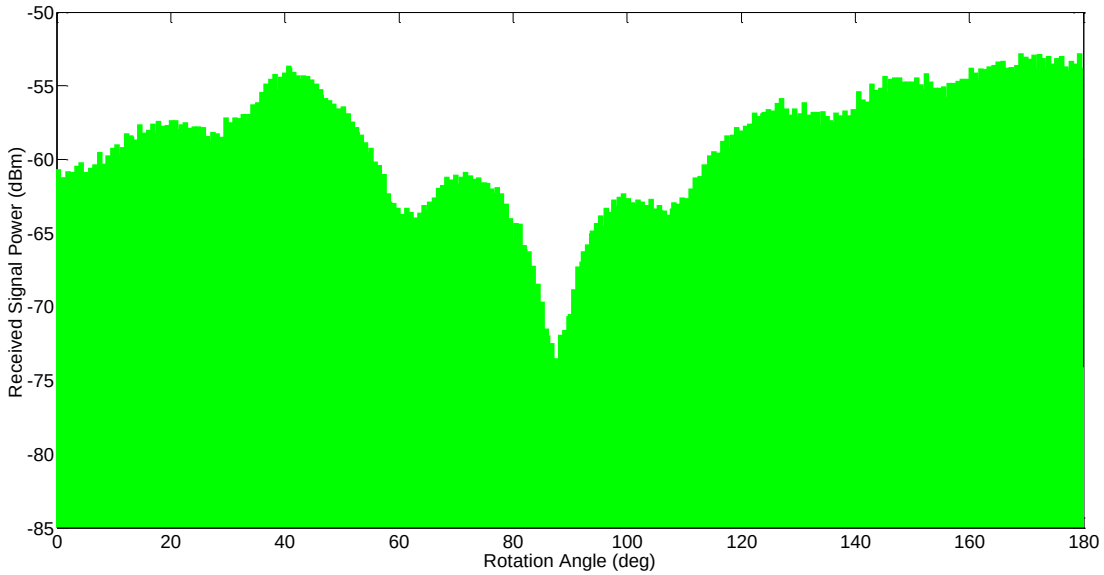

Figure 43. Elevation pattern of the SLiMS short pole at 3000 MHz (peak detection and RBW = 1 MHz).

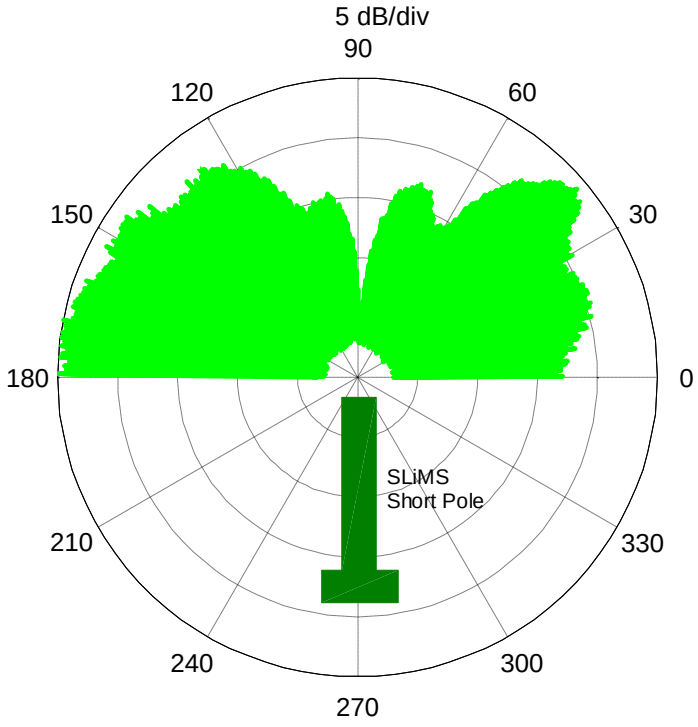

Figure 44. Polar elevation plot (side view) of the SLiMS short pole emissions at 3000 MHz.

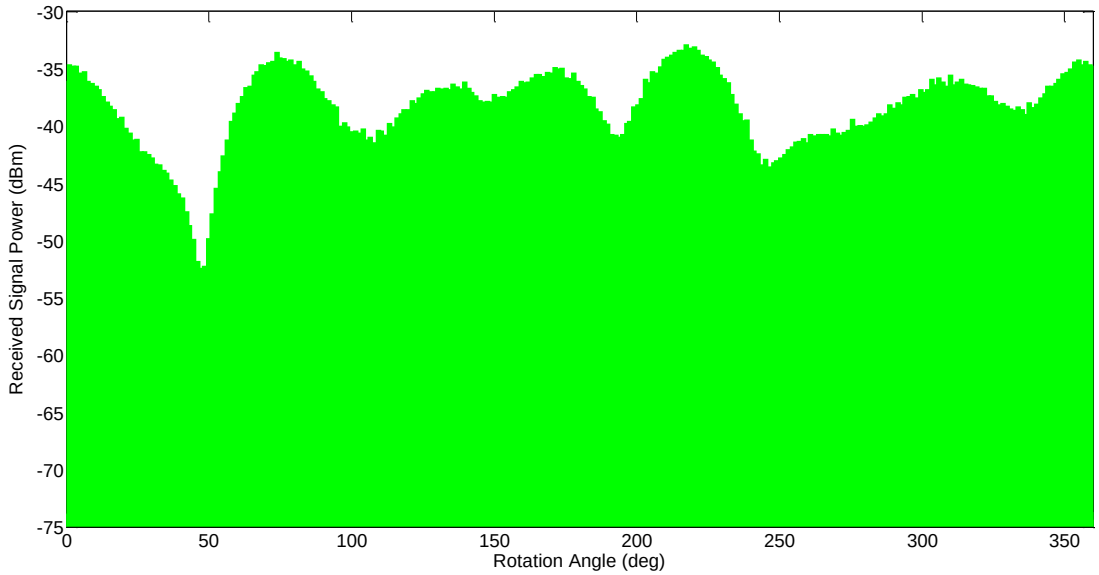

Figure 45. Azimuth pattern of the SLiMS short pole at 3950 MHz (peak detection and RBW = 1 MHz).

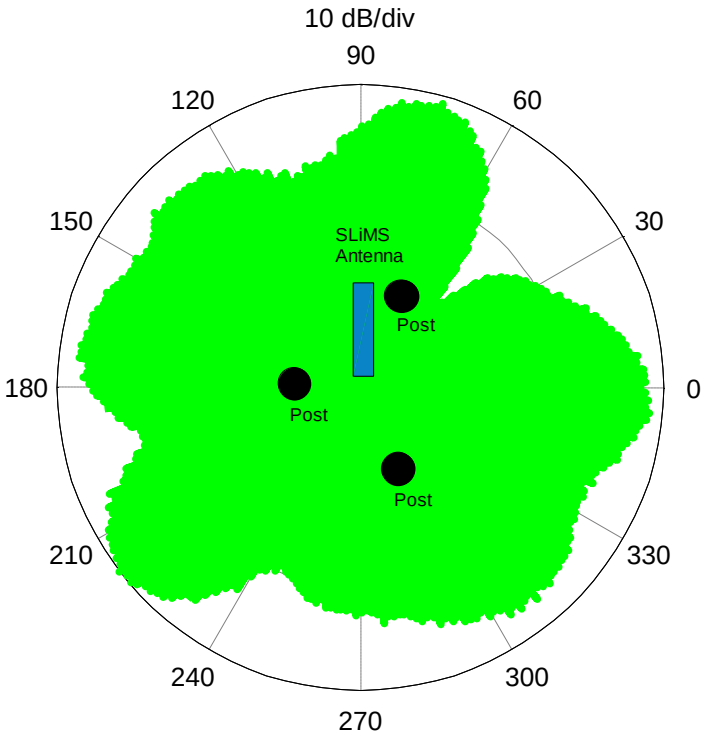

Figure 46. Polar azimuth plot (top view) of the SLiMS short pole emissions at 3950 MHz.

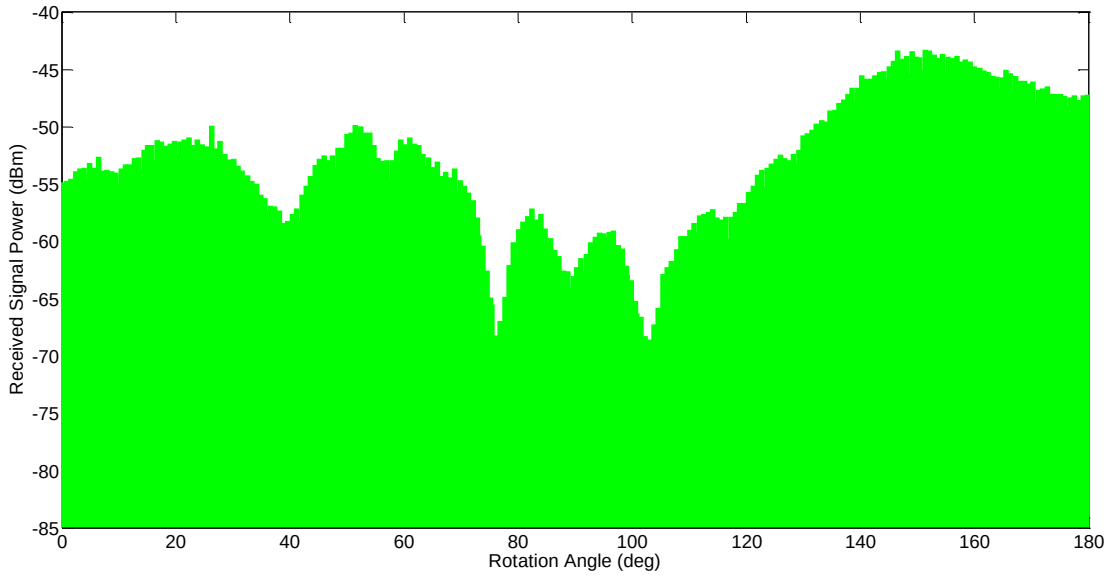

Figure 47. Elevation pattern of the SLiMS short pole at 3950 MHz (peak detection and RBW = 1 MHz).

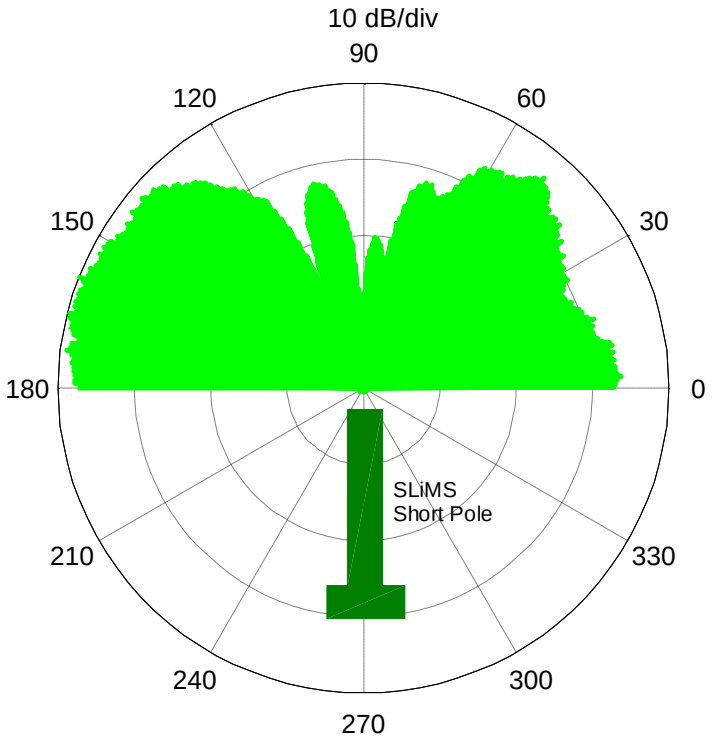

Figure 48. Polar elevation pattern of the SLiMS short pole at 3950 MHz (peak detection and RBW = 1 MHz).

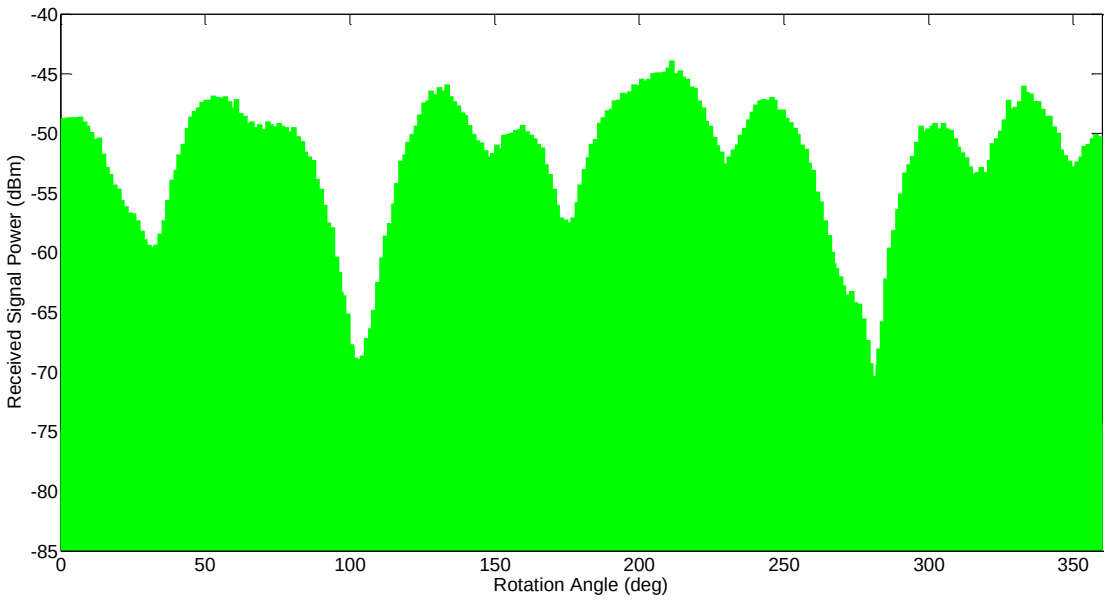

Figure 49. Azimuth pattern of the SLiMS short pole at 5000 MHz (peak detection and RBW = 1 MHz).

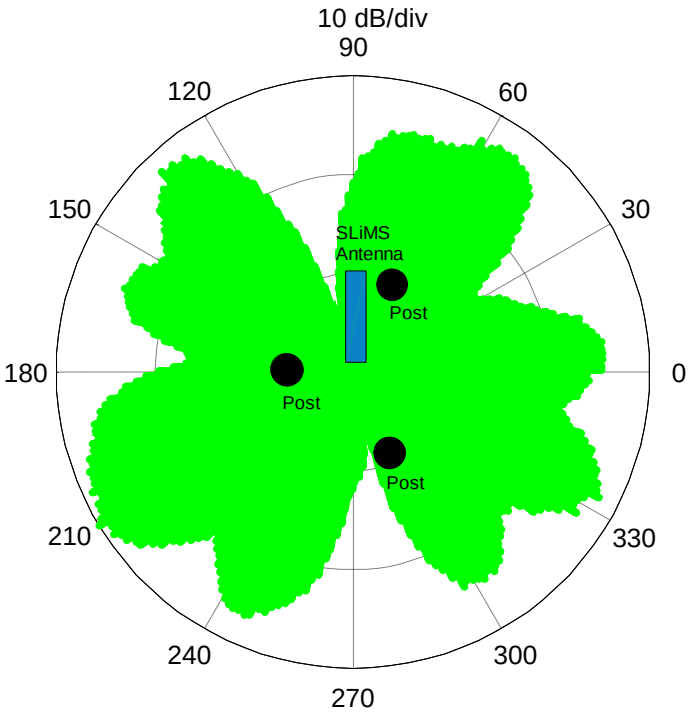

Figure 50. Polar azimuth plot (top view) of the SLiMS short pole emissions at 5000 MHz.

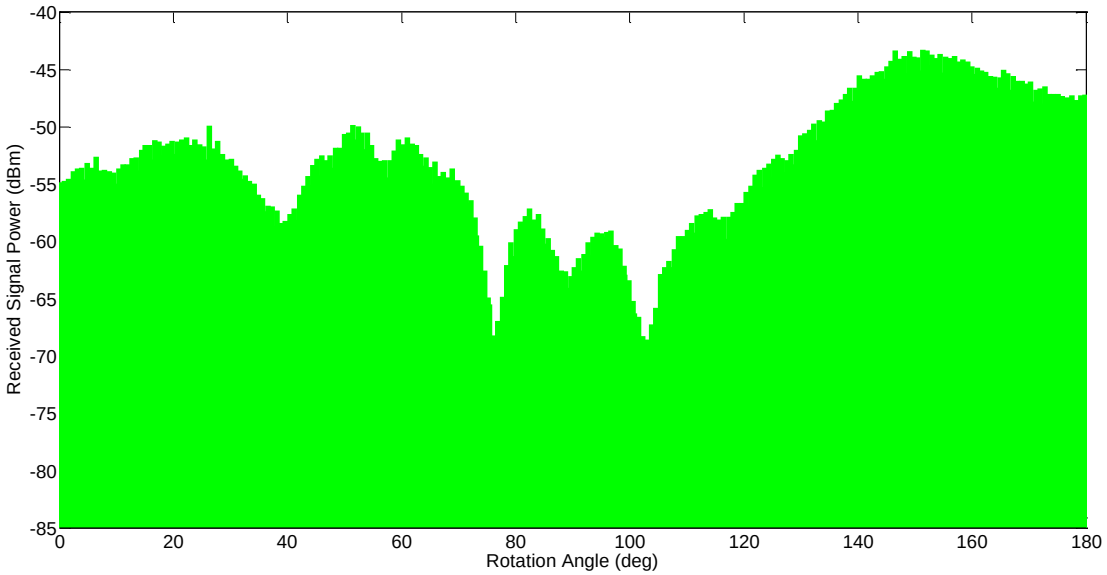

Figure 51. Elevation pattern of the SLiMS short pole at 5000 MHz (peak detection and RBW = 1 MHz).

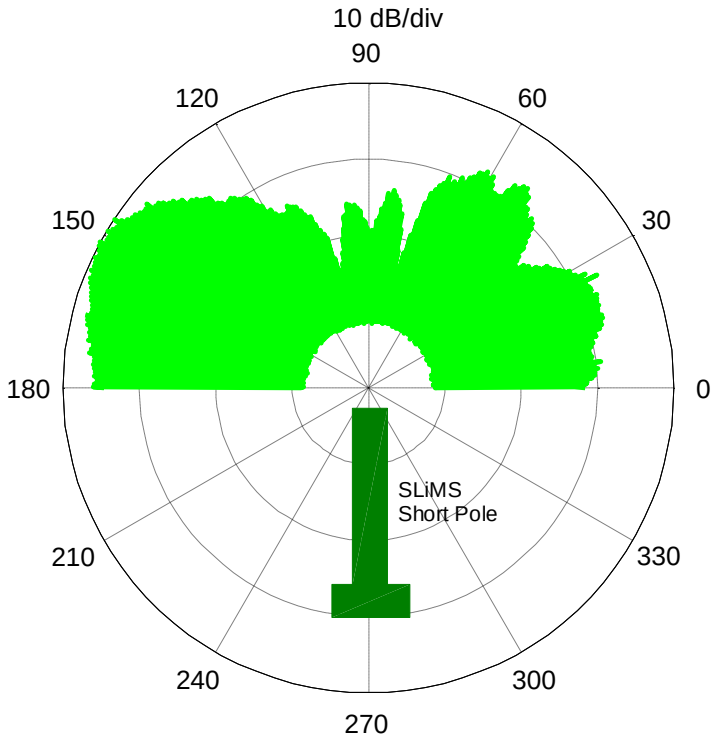

Figure 52. Elevation pattern of the SLiMS short pole at 5000 MHz (peak detection and RBW = 1 MHz).

3.10 Zero-Span Emissions Measurements

We carried out a series of the time-domain envelope measurements of the radiated emissions using the zero-span mode of the spectrum analyzer. We measured at 3000, 3950 and 5000 MHz with a distance of D = 3 m between the transmitting and receiving antennas. We used five resolution bandwidths from 100 kHz to 8 MHz. Figures 53–55 summarize the power envelope results obtained at the spectrum analyzer input with no calibration correction factors applied.

Figure 53 shows the power waveform envelopes with five different resolution bandwidths measured at 3000 MHz. The structure of a burst from the P400 radar is readily visible with a pulse width of 24 msec and period of 0.265 sec. The waveform levels increase with the bandwidth as expected since more signal energy is being passed through the analyzer filter. Figure 54 shows the 3950 MHz results, with maximum signal levels that were observed. The signal levels follow the same progression as before with increasing bandwidths. The 5000 MHz results are given in Figure 55, and the signal levels are reduced.

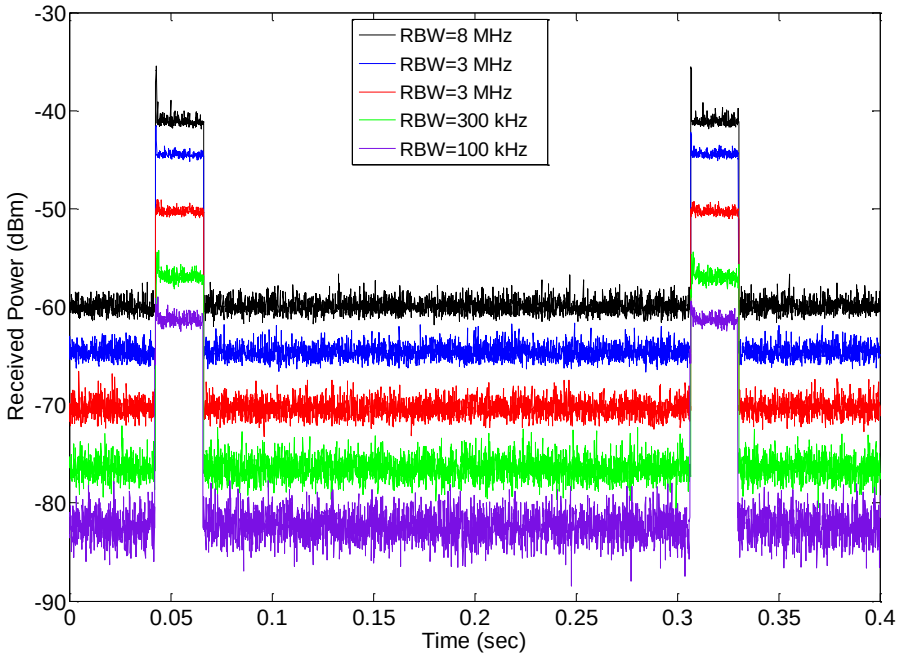

Figure 53. 3000 MHz zero-span results as a function of resolution bandwidth for peak detection.

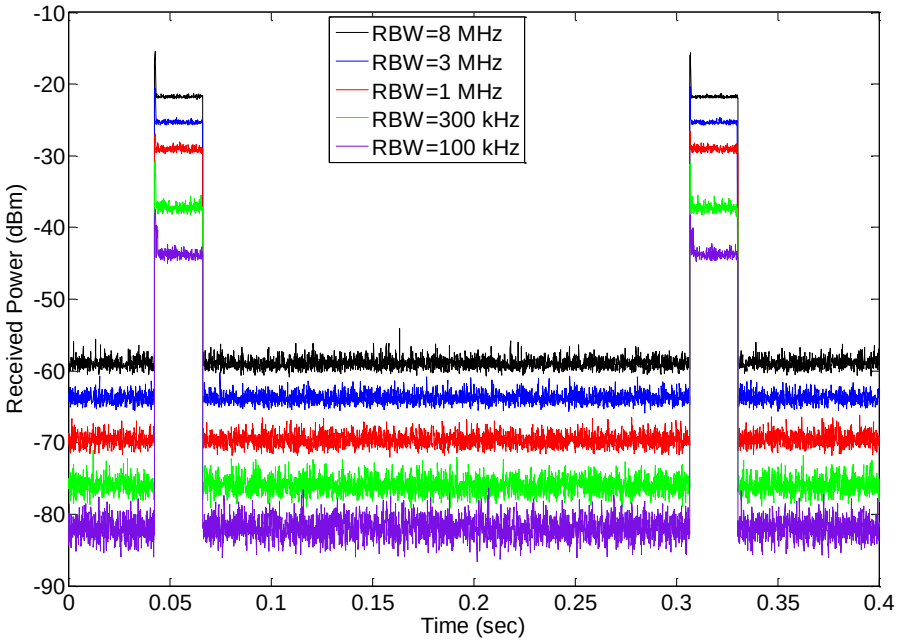

Figure 54. 3950 MHz zero-span results as a function of resolution bandwidth for peak detection.

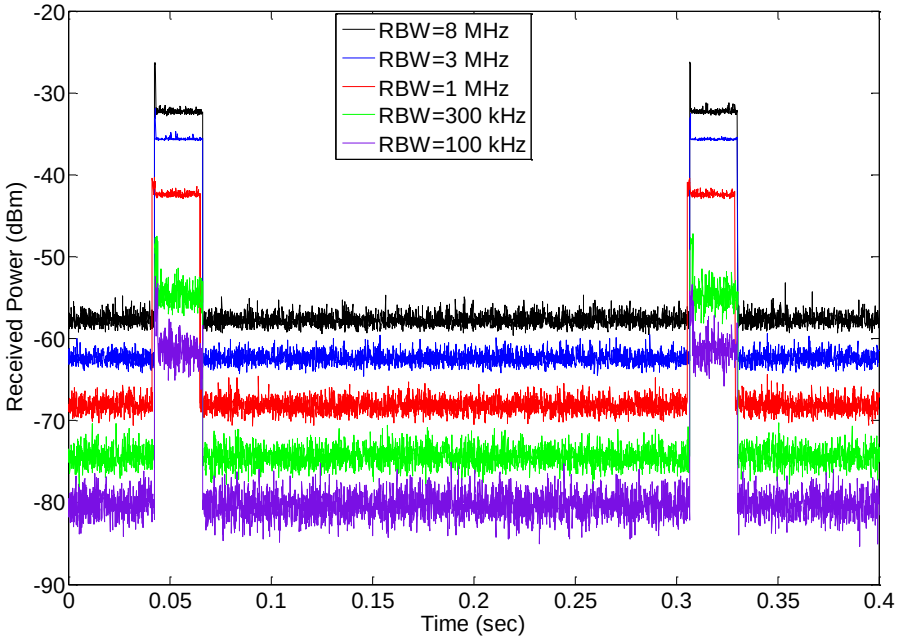

Figure 55. 5000 MHz zero-span results as a function of resolution bandwidth with peak detection.

3.11 Radiated Ultrawideband Waveforms

We performed a series of full-bandwidth, time-domain measurements using a high-speed, real-time oscilloscope. The bandwidth of the oscilloscope is 12 GHz, which permitted us to capture the fine details of the transmitted signal. We connected the output of the receiving antenna feed

network to the scope input using the radiated emission test setup shown in Figure 16. We collected waveforms at two different sampling intervals: 1) high speed with $t_s = 0.625$ ps with a record length of 40 μs, and 2) a lower sampling rate of $t_s = 0.2$ μs with a 400 ms record length. The high-speed sampling permits the resolution of individual UWB wavelets, and the lower speed allows us to examine the more global structure of the radar signal.

Figure 56 depicts a 400 ms record of the radiated radar signal at a distance of D = 3 m. The global structure is precisely the same as observed in the conducted case, with a burst duration of 24 ms and burst repetition interval of 0.265 s. Two successive wavelets are shown in Figure 57 and the spacing is 57.5 ns, which is the same as the conducted hardline tests. Figures 58–60 show the fundamental radiated wavelets received with a dish antenna at distances of D = 3, 2, and 4 m respectively. The duration of the wavelets is approximately 2.5 ns which is the same as observed in the conducted measurements. The shape of the wavelets is clearly more symmetric than the conducted result shown in Figure 3, due primarily to the impulse response characteristics of the dish receiving antenna. The peak amplitudes of the emitted impulses decrease with increasing distance as expected but do not follow a precise 1/D variation. More analysis is needed to better understand this behavior.

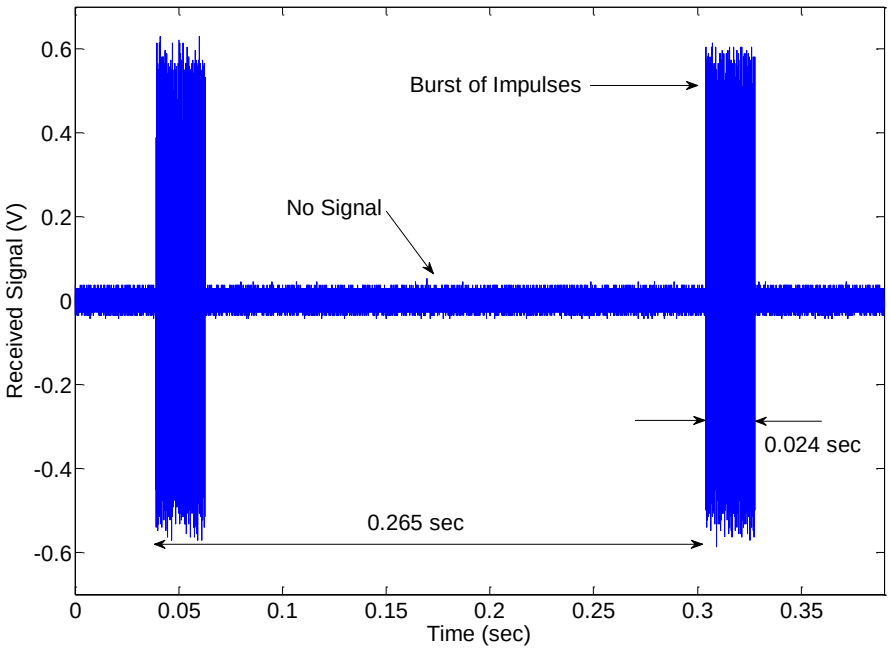

Figure 56. Radiated burst of the SLiMS pole received by the dish antenna at D = 3 m.

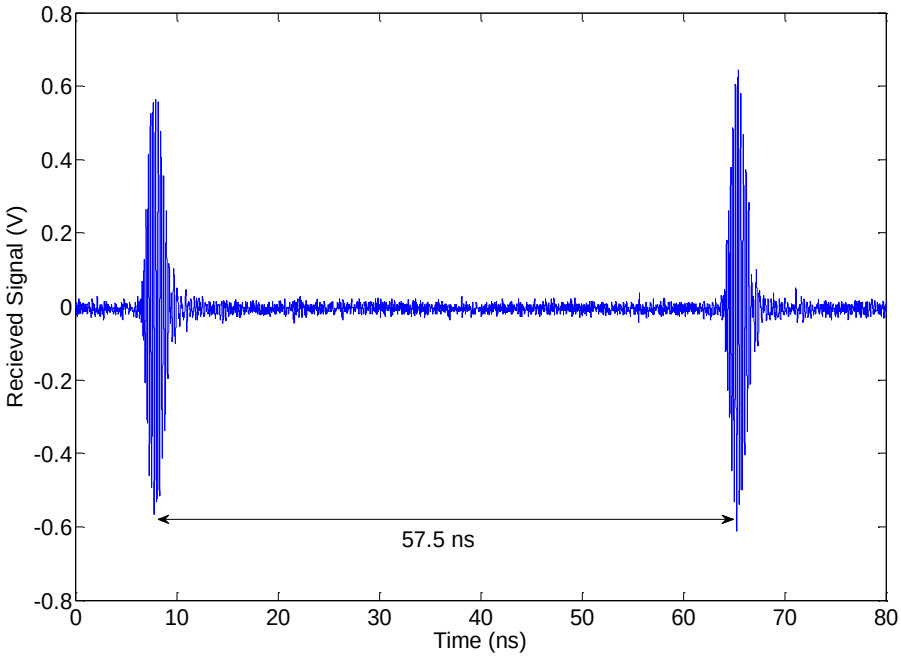

Figure 57. Two successive wavelets emitted by the SLiMS short pole received by the dish antenna at D = 3 m.

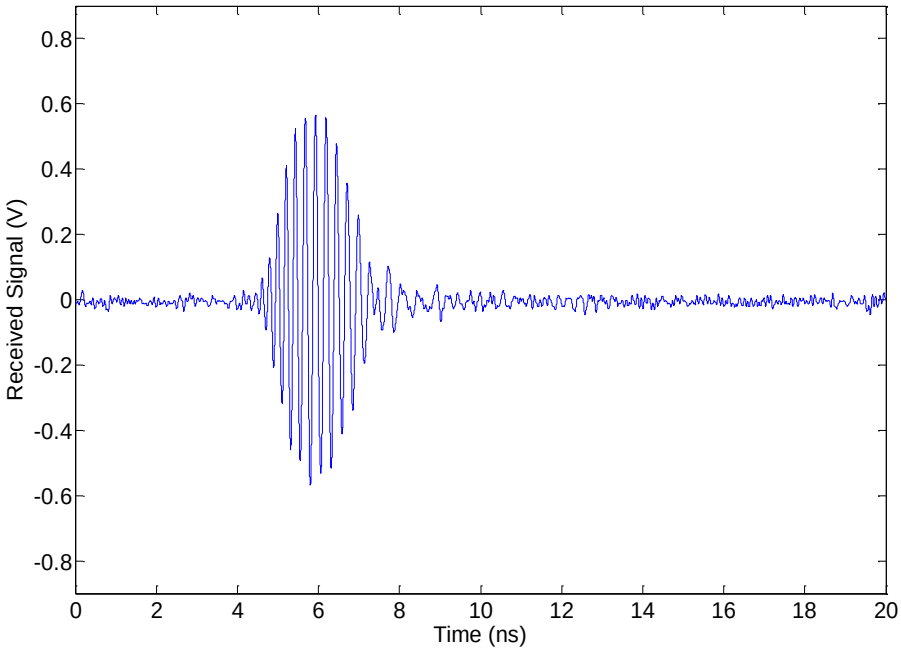

Figure 58. Single wavelet emitted by the by the SLiMS short pole received by the dish antenna at D = 3 m.

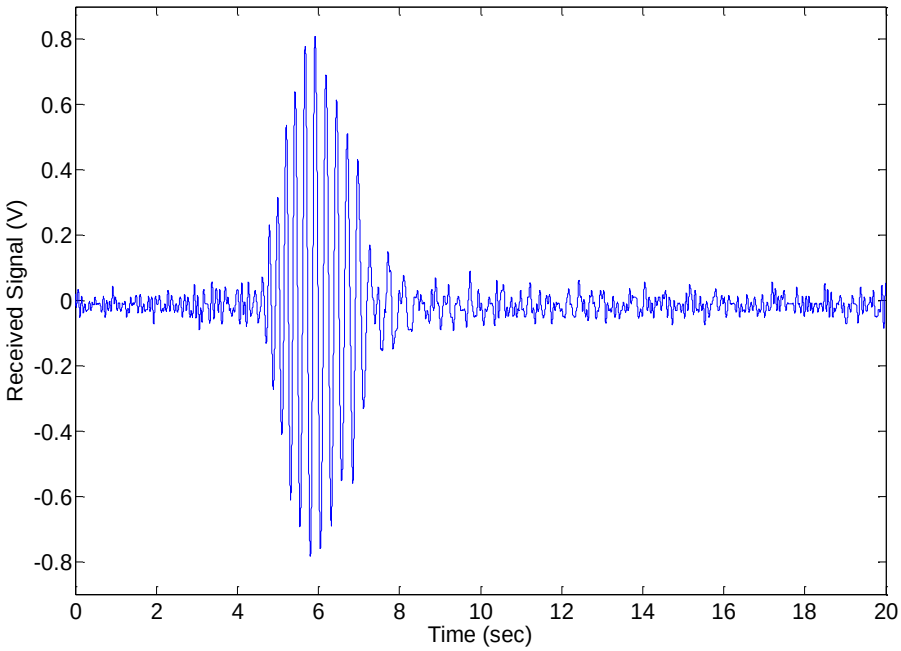

Figure 59. Single wavelet emitted by the by the SLiMS short pole received by the dish antenna at D = 2 m.

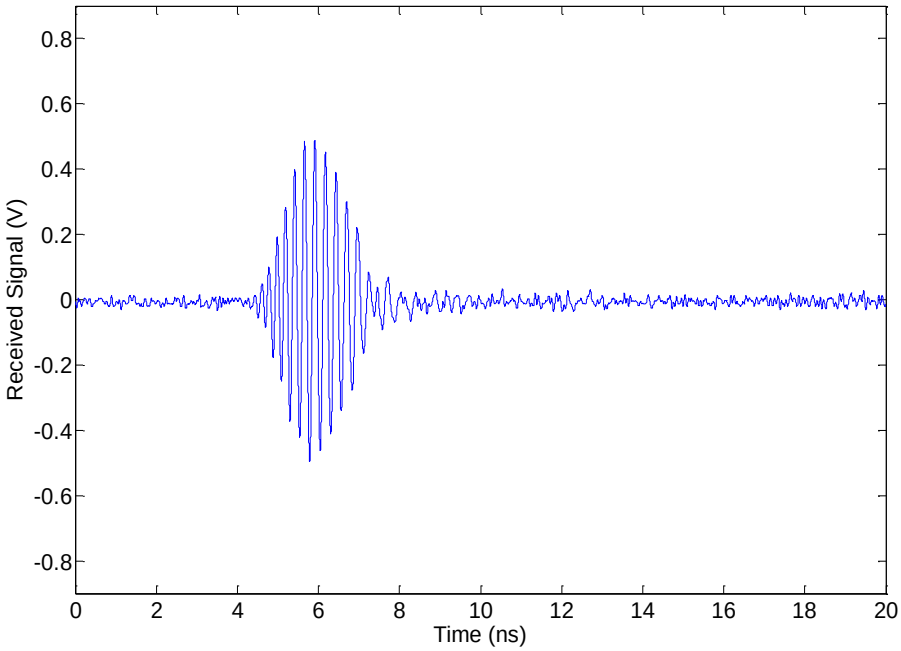

Figure 60. Single wavelet emitted by the by the SLiMS short pole received by the dish antenna at D = 4 m.

3.12 Radome Tests-II

We performed a second series of elevation and azimuthal pattern measurements on the shortened SLiMS pole. The purpose of this effort was to assess the impact of two different protective radome materials on the electromagnetic radiation properties of the SLiMS pole and to examine the impact of centering the P400 radar. We performed measurements on:

- The uncovered SLiMS pole
- The SliMS pole covered with a PVC plastic pipe material
- The SLiMS pole covered with a ABS plastic pipe material

For each of these pole configurations we measured:

- A 360° azimuthal pattern at 2000, 3000, 3950, 4000, 5000, and 6000 MHz
- A 180° elevation pattern at 2000, 3000, 3950, 4000, 5000 and 6000 MHz
- Swept frequency responses over the 2000–6000 MHz frequency range at selected azimuth angles

We conducted a series of azimuthal pattern measurements at selected frequencies from 2000–6000 MHz for several SLiMS pole configurations. We first measured the uncovered SLiMS short pole using the 0.9 m diameter dish receiving antenna at a distance of 3 m. TDC provided a new P400 antenna and mounting bracket. The setup is shown in Figure 18. The new antenna radiating element itself was unchanged but the feed line was treated with absorbing material to suppress common-mode currents on the outer conductor of the coaxial feed line. The mounting bracket was provided by TDC to permit the antenna radiating element to be placed at the center of the pole, in order to improve angular pattern symmetry. To perform pattern measurements, we configured the spectrum analyzer to operate in the zero-span mode with average detection and RBW = 1 MHz. We divided the time scale into 360 equal bins (buckets) and set the sweep time such that four bursts were captured within each bin to ensure an accurate measurement. We synchronized the rotation time of the positioner to be identical with the sweep time of the spectrum analyzer. These settings resulted in excellent measurement fidelity.

For the elevation measurements, we used the same methodology of synchronizing the rotation time of the pole to the sweep time of the spectrum analyzer. With the exception of the sweep time, all of the other spectrum analyzer settings were identical to those used in the azimuthal pattern measurements. We slowed down the sweep time to once again allow averaging over four bursts to see if including additional bursts would significantly impact the results. The observed impact was minimal. Table 4 summarizes the instrument settings that were used in the pattern measurements.

We sequentially measured three different SLiMS pole configurations: 1) the uncovered pole shown in Figure 22, 2) a pole with an ABS cover shown in Figure 25, and 3) a pole with the PVC cover that was used in the prior test, shown in Figure 24. We performed a series of elevation measurements as well. In order to obtain an elevation pattern we attached the pole horizontally to a dielectric support as shown in Figures 61 (a)–(c). We then rotated the pole in the horizontal plane over the range of angles of 0°–180° using the azimuth axis of the antenna positioner. The rotation scans progressively from the front of the pole (0°), over the top (90°), to

the back side (180°). Since the pole was re-oriented horizontally, we rotated the receiving antenna 90° to maintain a co-polarized condition. We repeated the measurements with the ABS and PVC radome as is depicted in Figures 65 (b) and (c) respectively.

Table 4. Instrument and turntable settings for the SLiMS pattern measurements.

Measurement Parameter	Azimuthal Pattern (0°–360°)	Elevation Pattern (0°–180°)
SA Resolution Bandwidth	1 MHz	1 MHz
SA Video Bandwidth	1 MHz	1 MHz
SA Detection Mode	Average	Average
SA Sweep Time	766 s	382 s
Positioner Rotation Rate	0.47° /s	0.47° /s

We used the same methodology of synchronizing the rotation time of the pole to the sweep time of the spectrum analyzer. With the exception of the sweep time, all of the other spectrum analyzer settings were identical to those used in the azimuthal pattern measurements. We slowed the sweep time to perform averaging over four TDMA bursts to see if including additional bursts would significantly impact the results. The observed impact was minimal.

The azimuth and elevation pattern results are shown in Figures 62–85 at six frequencies. The plots are grouped by frequency. Each group contains both azimuth and elevation graphs that are plotted in both rectangular and polar coordinates. Each graph contains plots with no cover (as a baseline reference) along with results for the two radome materials. The results show complex behavior that is a strong function of both frequency and angle. At 3950 MHz and 4000 MHz, the use of radome materials significantly reduces the peak-to-peak variations in radiated field levels as can be seen in Figures 70–73. This is because the radomes provide a more homogenous boundary and thereby reduce angular pattern variations. Also, when there is no radome present, we see minima in the radiated field levels when the dielectric support rods are located directly between the transmitting and receiving antennas. This is a blockage effect. This does disappear as we move away from the peak emissions region. The largest variations are seen above the peak resonance region at 5000 MHz. In the elevation patterns, we see a pronounced dipole null at angles near 90° at 3950 MHz, 4000 MHz, and 5000 MHz. A less pronounced null is seen at 3000 MHz. No null occurs at either 2000 MHz or 6000 MHz.

We performed fully calibrated swept-frequency measurements for both peak and average detection. Measurements were taken at 3950 MHz at the azimuth angles which maximized emission levels. The azimuth angle for a maximum was 26° with no cover and the PVC radome, and 120° with the ABS cover. The results are shown in Figures 86 and 87, and the ABS radome results depart significantly from the others above 4800 MHz. The measured EIRP levels are quite similar to those obtained in earlier measurements. However, each emissions plot has a distinctly different functional behavior depending on the radome treatment. This is a result of the maximization process where we perform swept measurements at different azimuth angles. We did not see this with the earlier radome tests (Section 3.9) since the azimuth angle remained fixed at 0°.

(a)

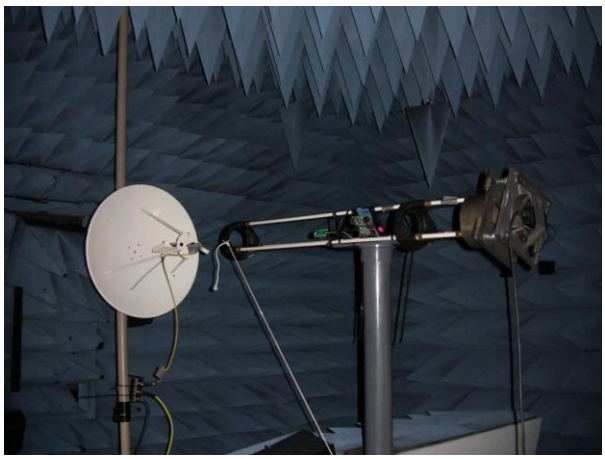

(b)

(c)

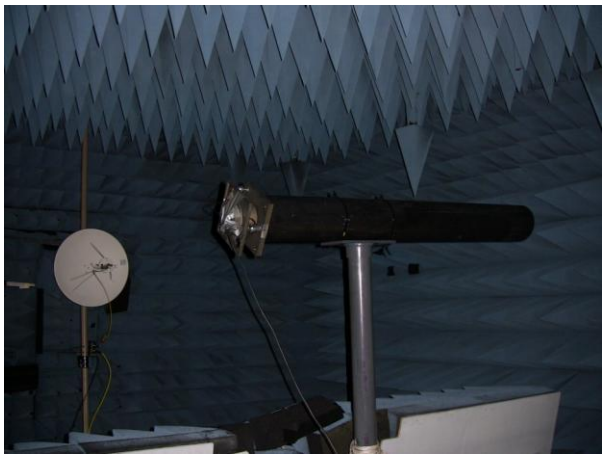

Figure 61. Elevation pattern measurements. (a) Uncovered pole, (b) PVC radome, and (c) ABS radome.

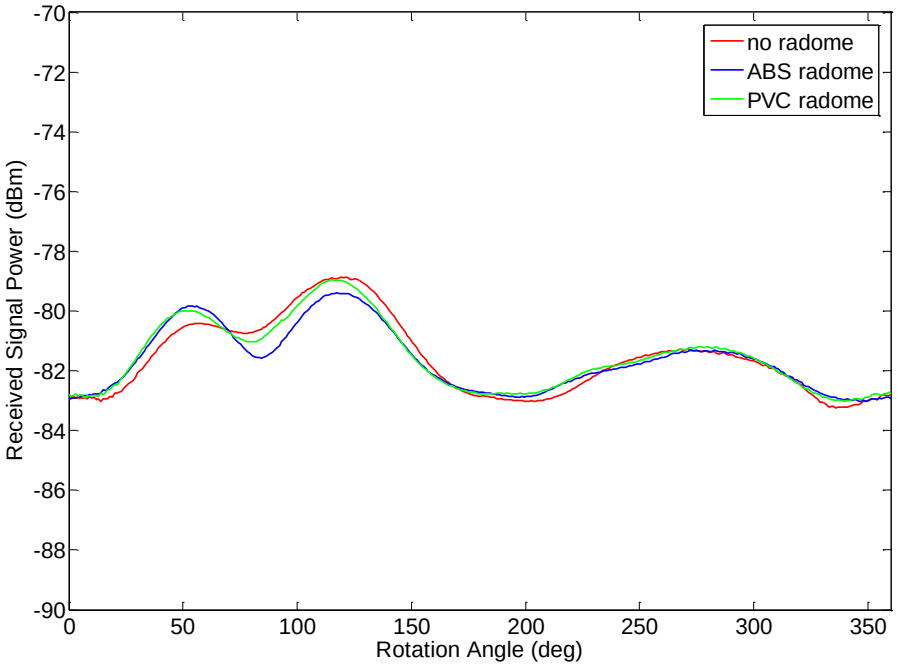

Figure 62. Azimuth pattern of the SLiMS short pole at 2000 MHz with average detection and RBW = 1 MHz.

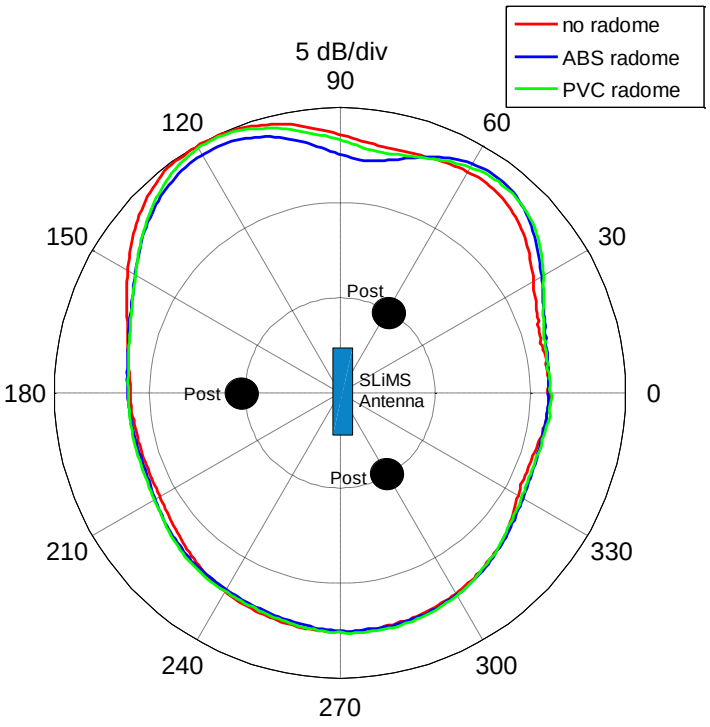

Figure 63. Polar azimuth plot (top view) of the SLiMS short pole emissions at 2000 MHz.

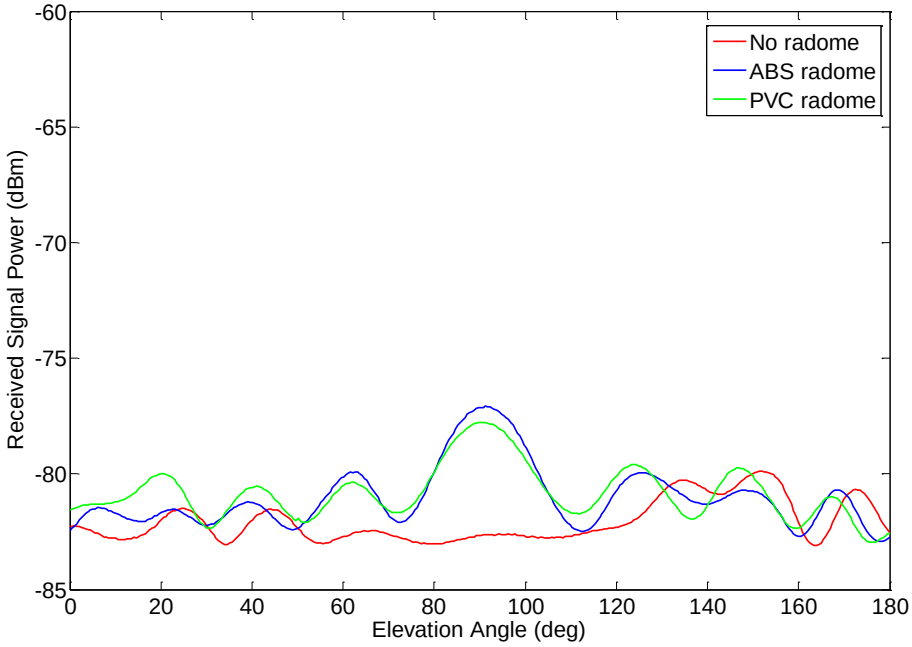

Figure 64. Elevation pattern of the SLiMS short pole at 2000 MHz with average detection and RBW = 1 MHz.

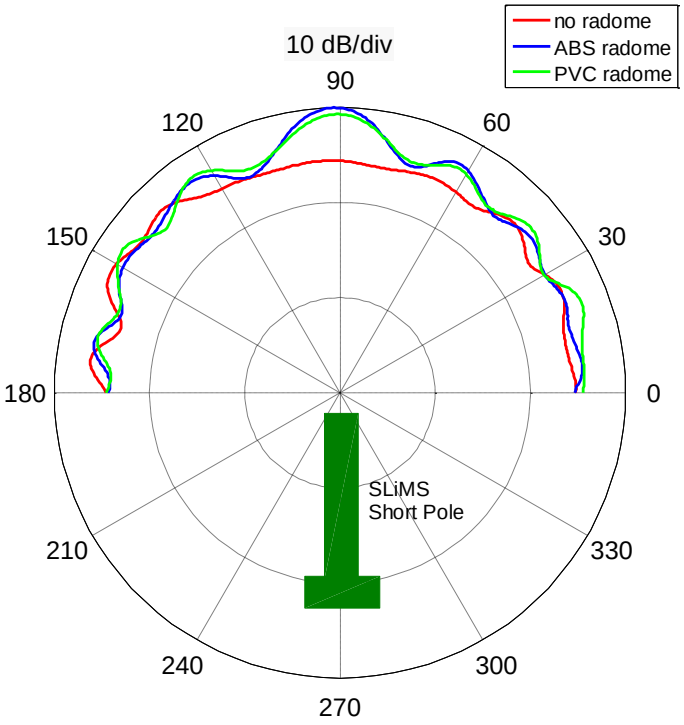

Figure 65. Polar elevation plot (side view) of the SLiMS short pole emissions at 2000 MHz.

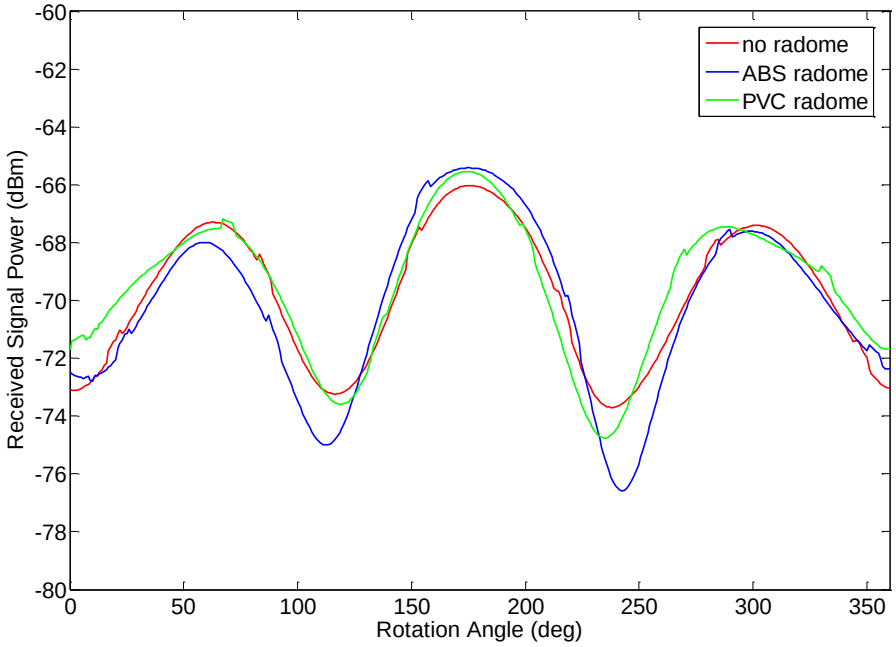

Figure 66. Azimuth pattern of the SLiMS short pole at 3000 MHz with average detection and RBW = 1 MHz.

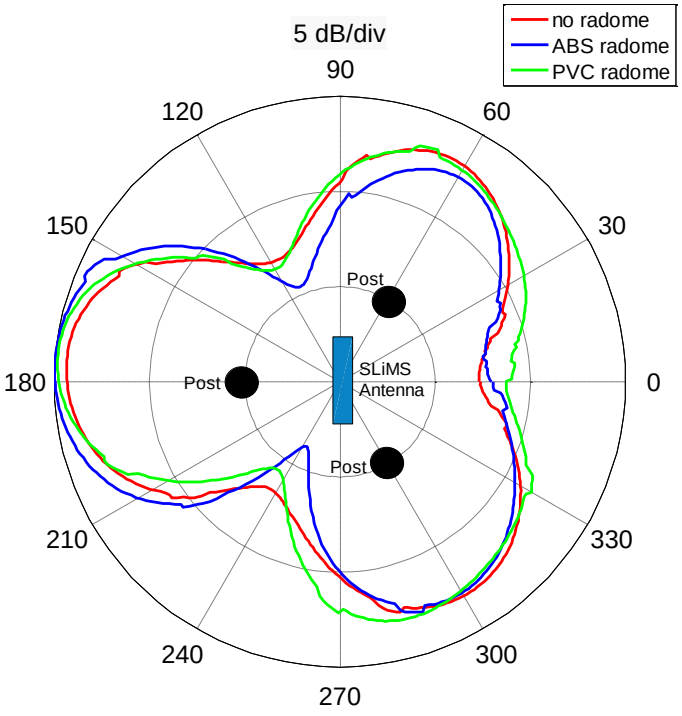

Figure 67. Polar azimuth plot (top view) of the SLiMS short pole emissions at 3000 MHz.

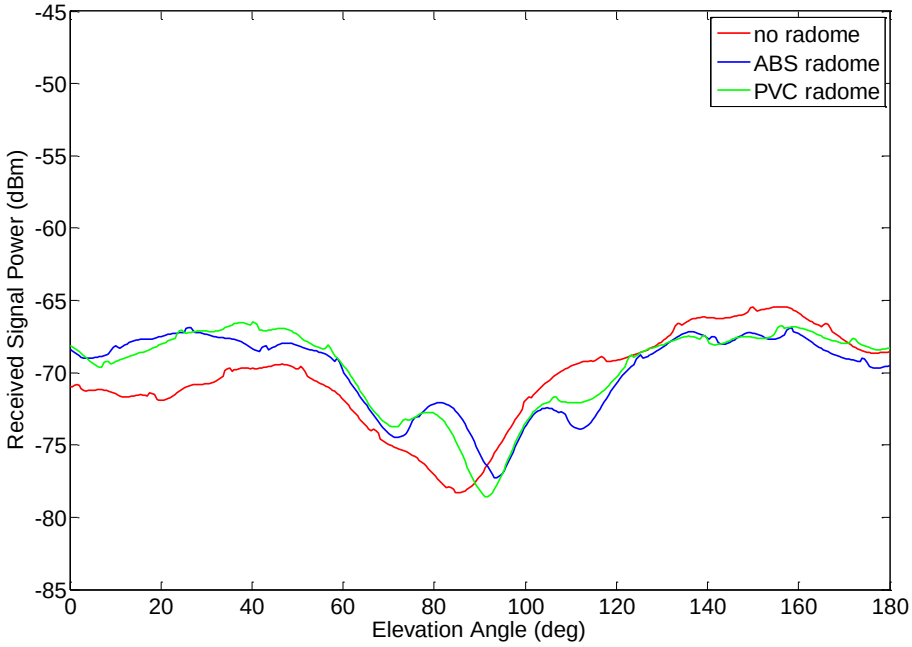

Figure 68. Elevation pattern of the SLiMS short pole at 3000 MHz with average detection and RBW = 1 MHz.

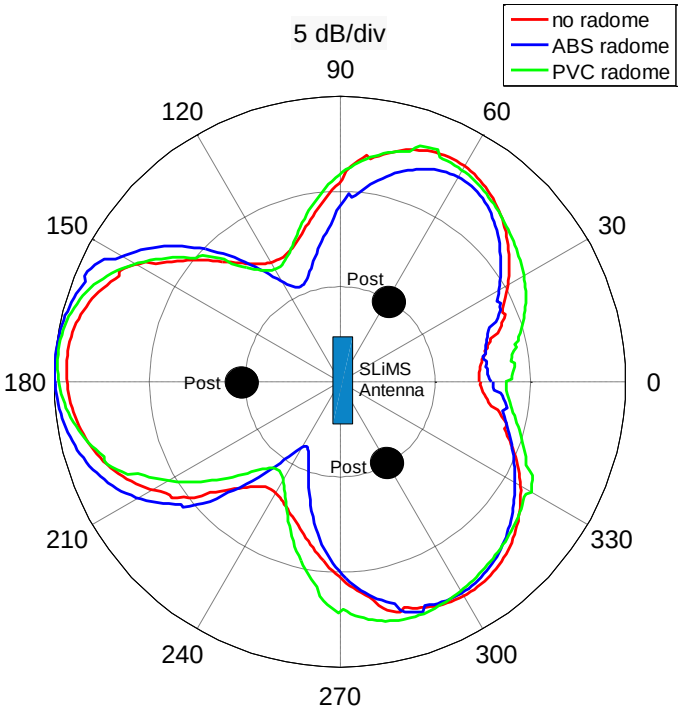

Figure 69. Polar elevation plot (side view) of the SLiMS short pole emissions at 3000 MHz.

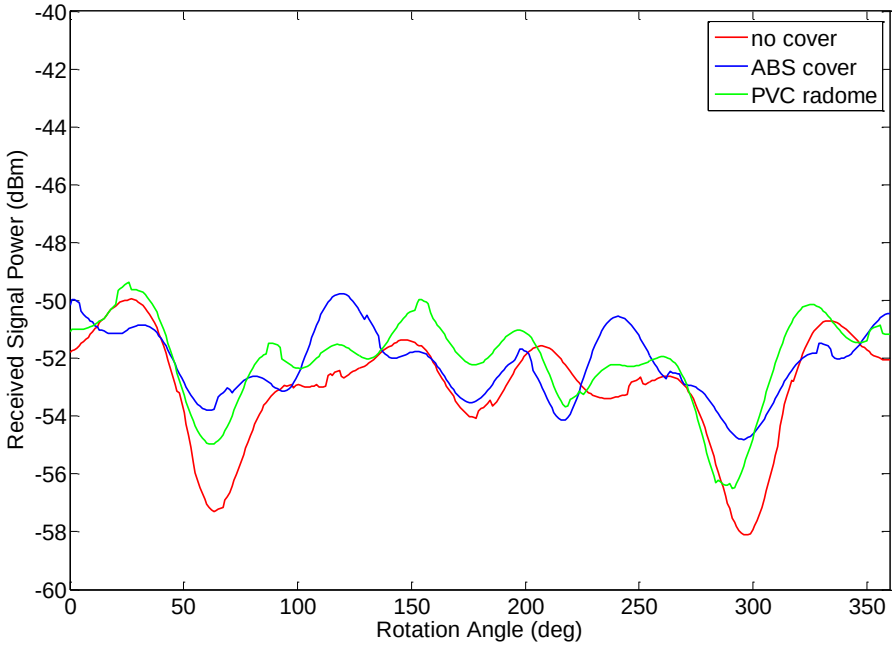

Figure 70. Azimuth pattern of the SLiMS short pole at 3950 MHz with average detection and RBW = 1 MHz.

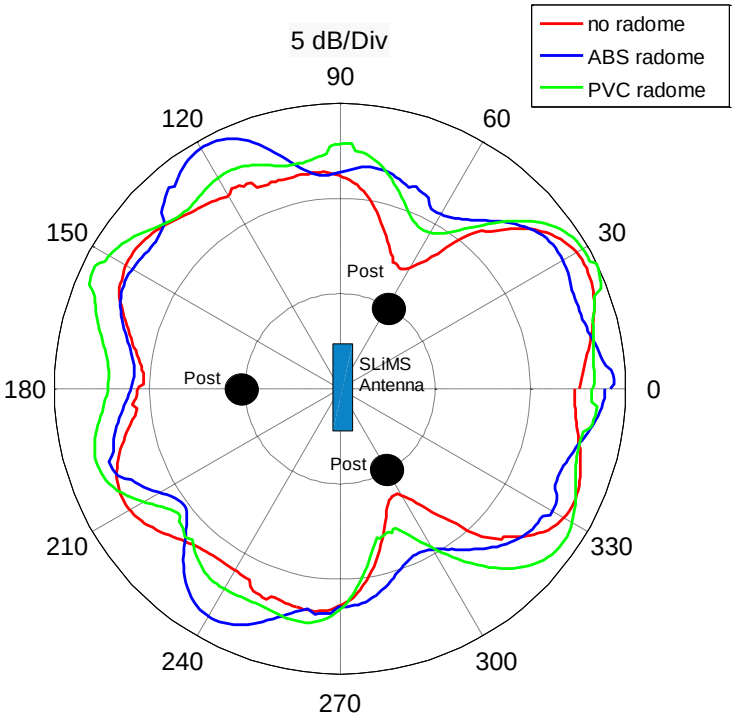

Figure 71. Polar azimuth plot (top view) of the SLiMS short pole emissions at 3950 MHz.

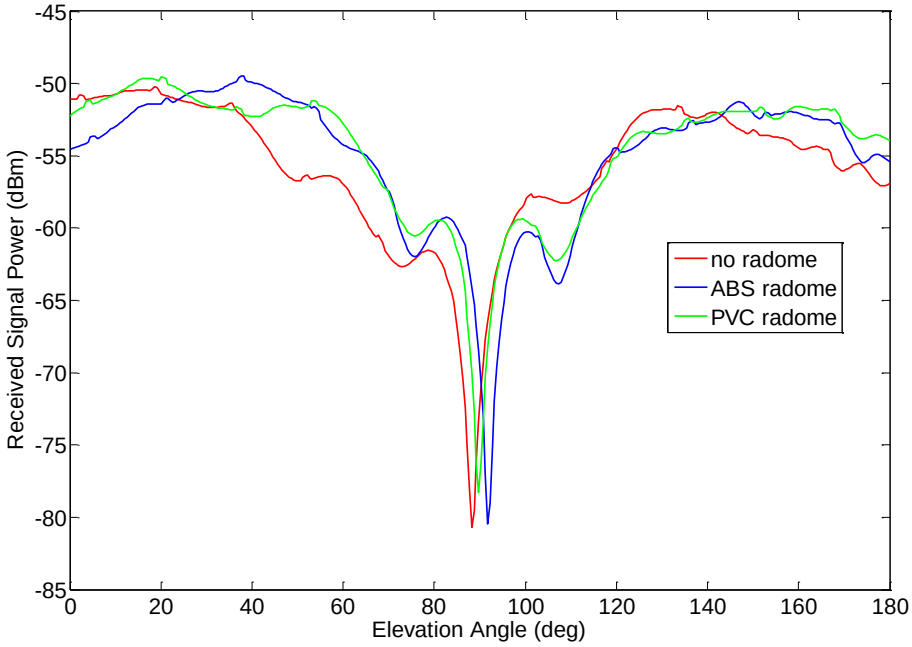

Figure 72. Elevation pattern of the SLiMS short pole at 3950 MHz with average detection and RBW = 1 MHz.

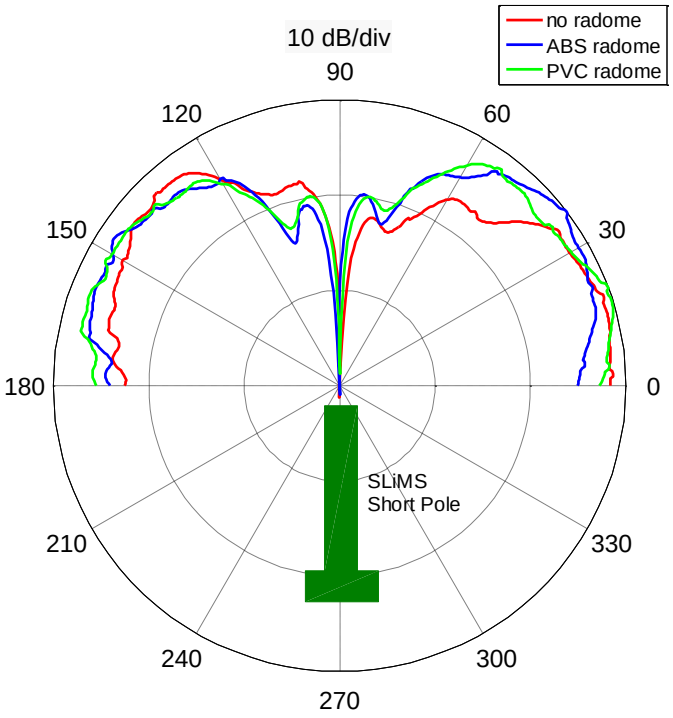

Figure 73. Polar elevation plot (side view) of the SLiMS short pole emissions at 3950 MHz.

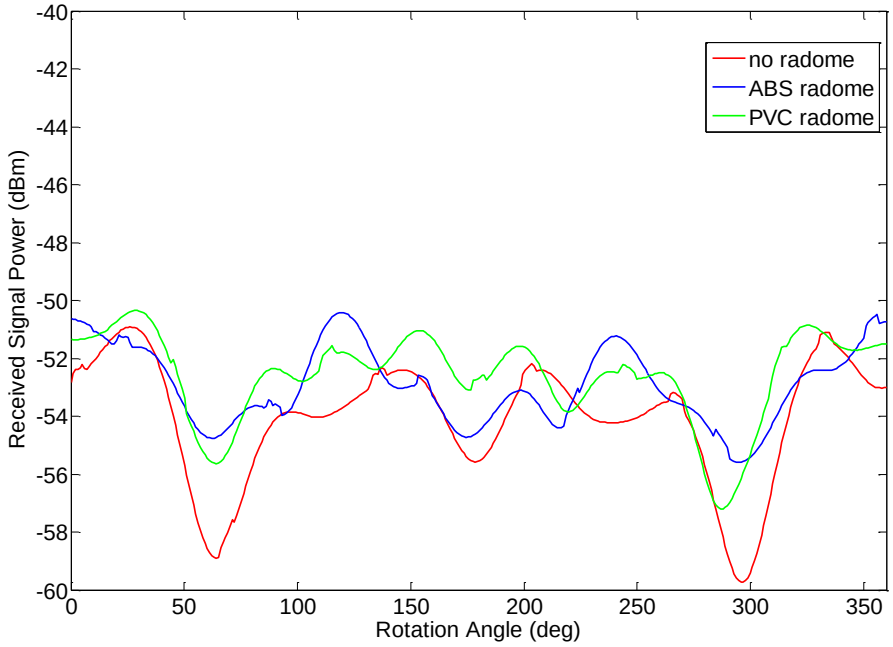

Figure 74. Azimuth pattern of the SLiMS short pole at 4000 MHz with average detection and RBW = 1 MHz.

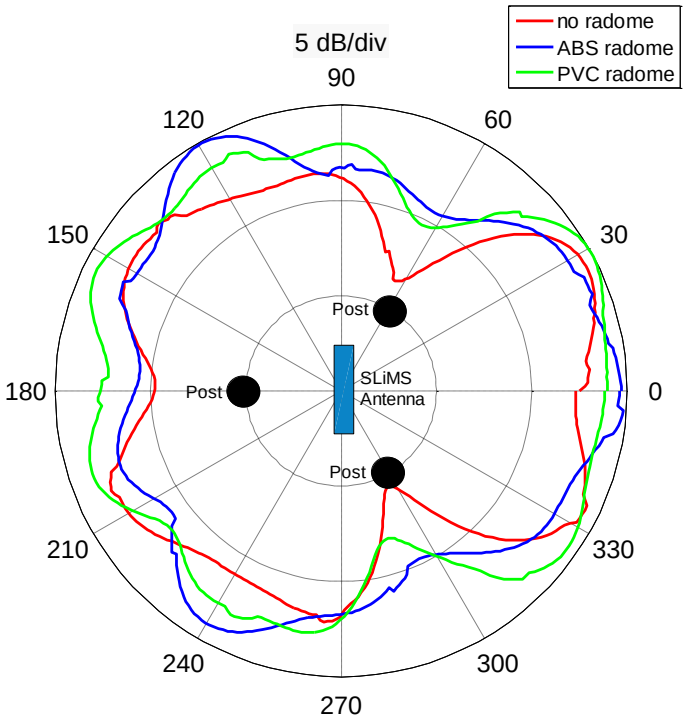

Figure 75. Polar azimuth plot (top view) of the SLiMS short pole emissions at 4000 MHz.

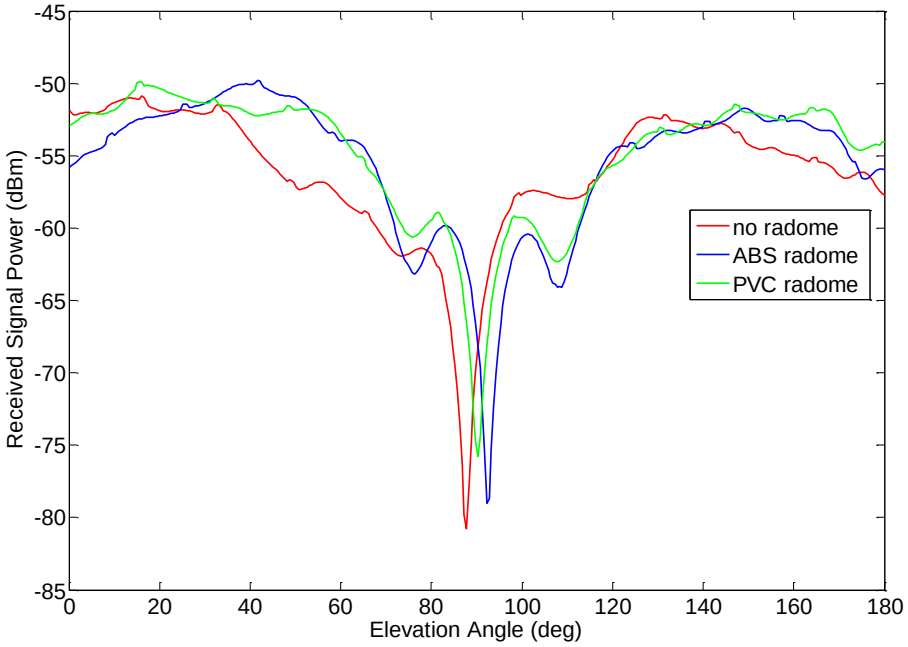

Figure 76. Elevation pattern of the SLiMS short pole at 4000 MHz with average detection and RBW = 1 MHz.

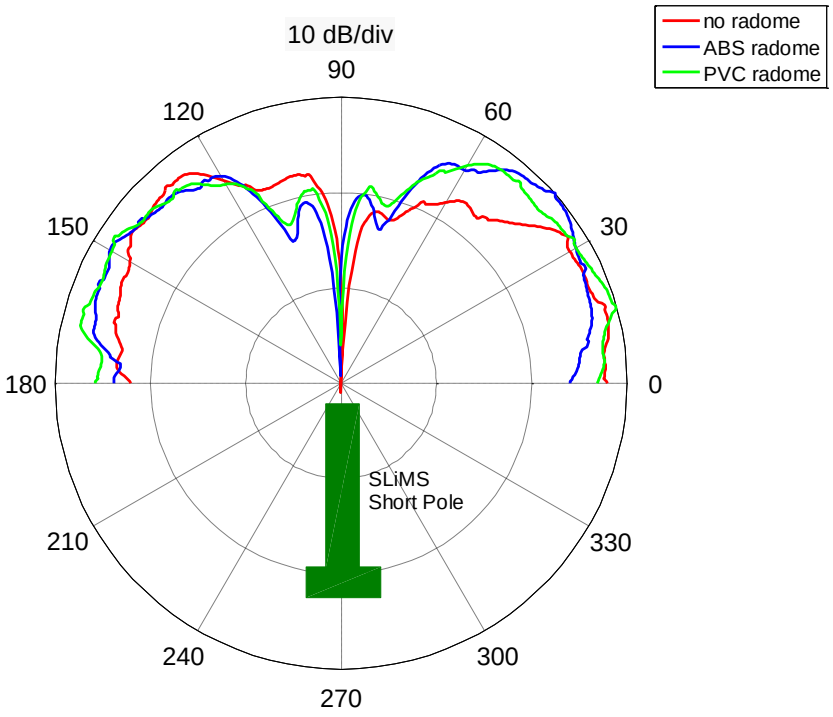

Figure 77. Polar elevation plot (side view) of the SLiMS short pole emissions at 4000 MHz.

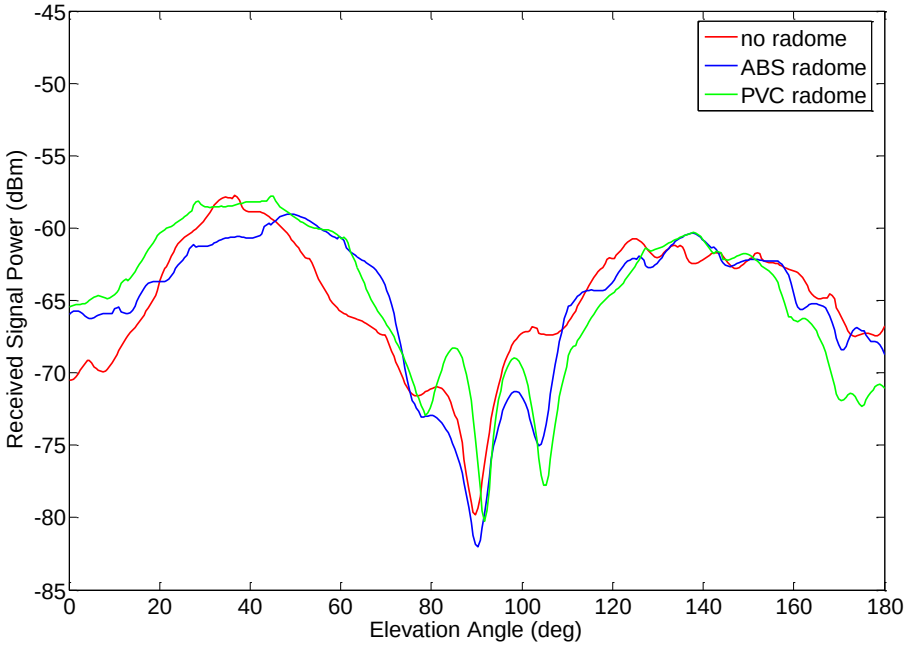

Figure 78. Azimuth pattern of the SLiMS short pole at 5000 MHz with average detection and RBW = 1 MHz.

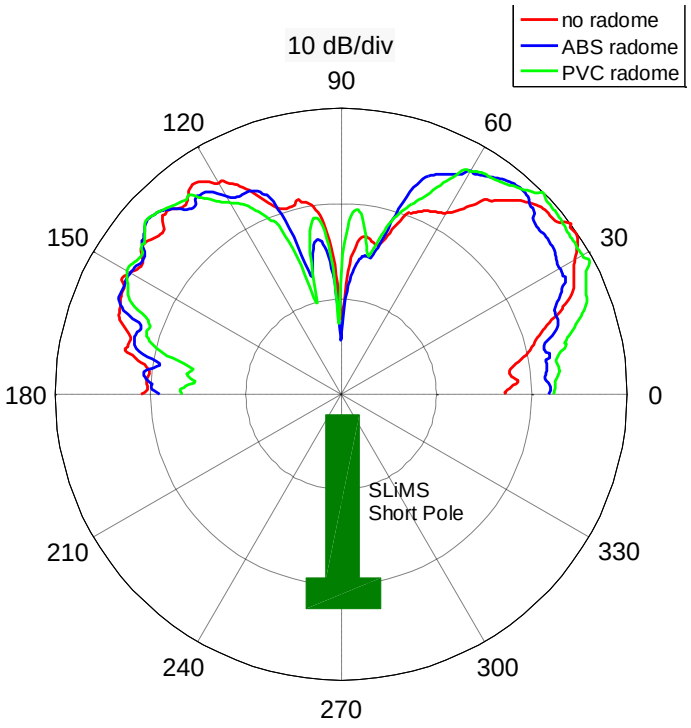

Figure 79. Polar azimuth plot (top view) of the SLiMS short pole emissions at 5000 MHz.

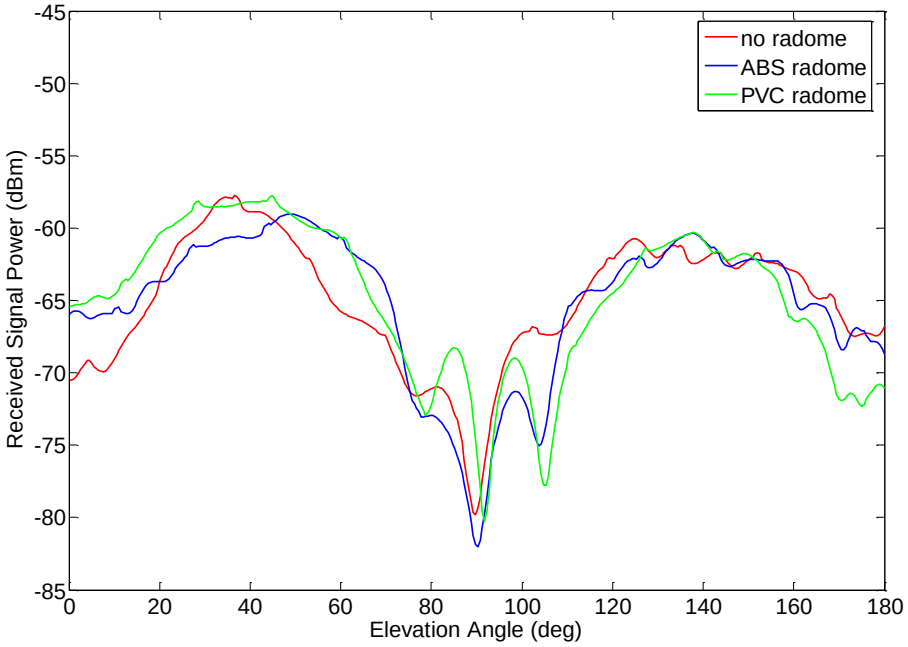

Figure 80. Elevation pattern of the SLiMS short pole at 5000 MHz with average detection and RBW = 1 MHz.

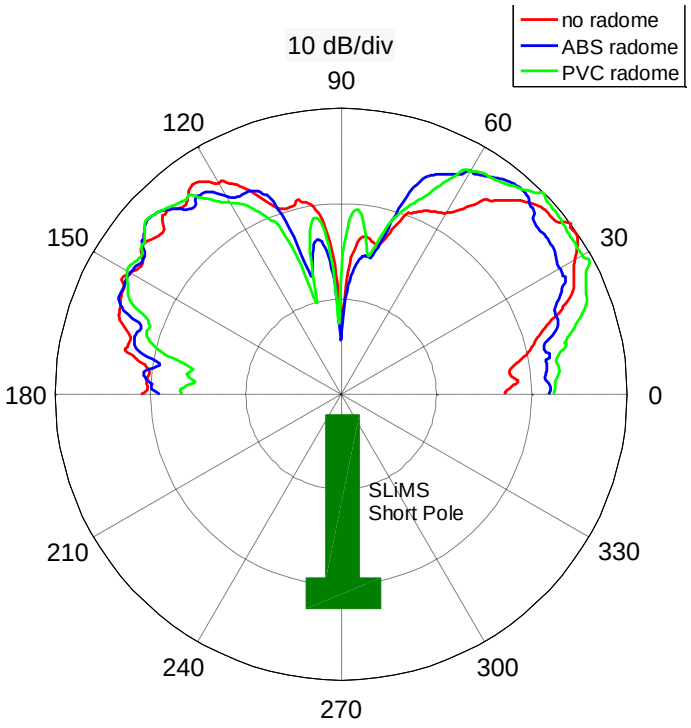

Figure 81. Polar elevation plot (side view) of the SLiMS short pole emissions at 5000 MHz.

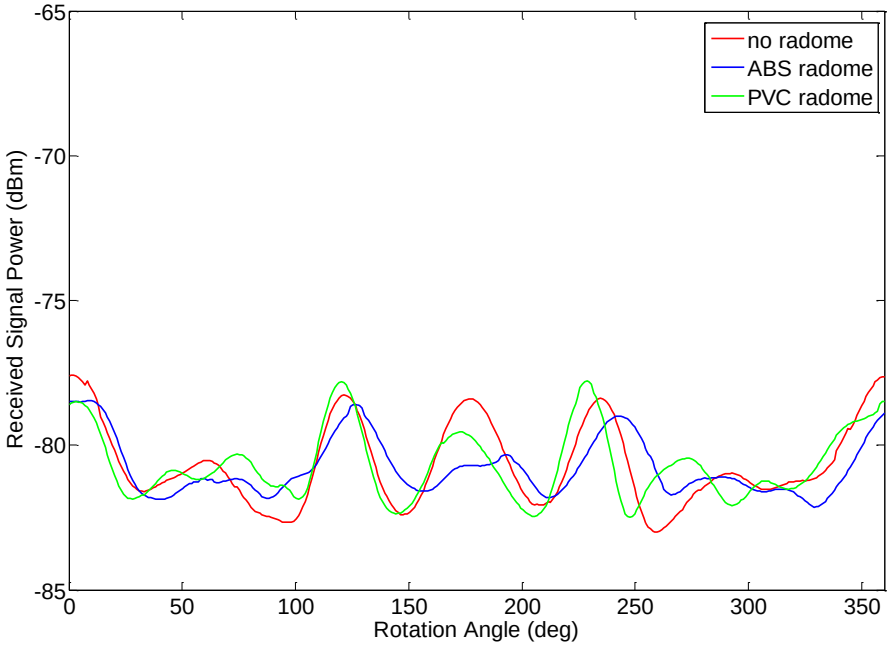

Figure 82. Azimuth pattern of the SLiMS short pole at 6000 MHz (average detection and RBW = 1 MHz.

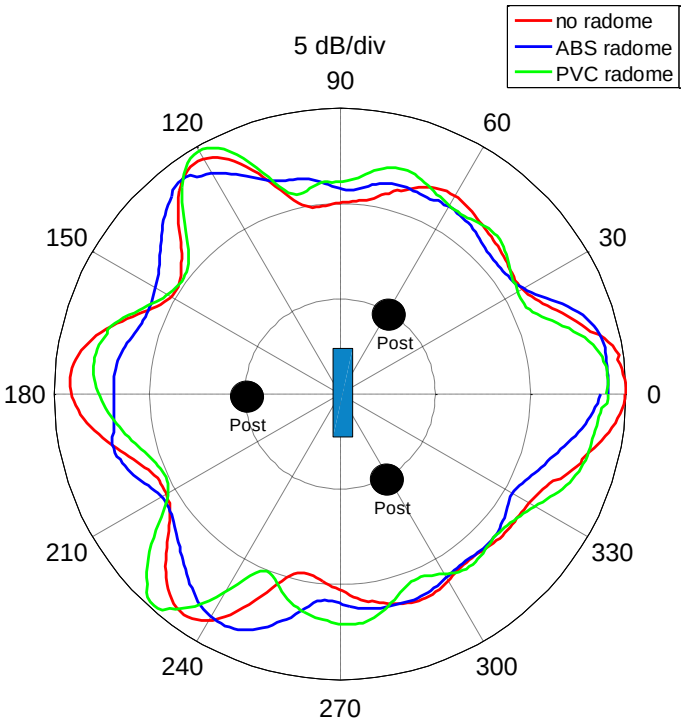

Figure 83. Polar azimuth plot (top view) of the SLiMS short pole emissions at 6000 MHz.

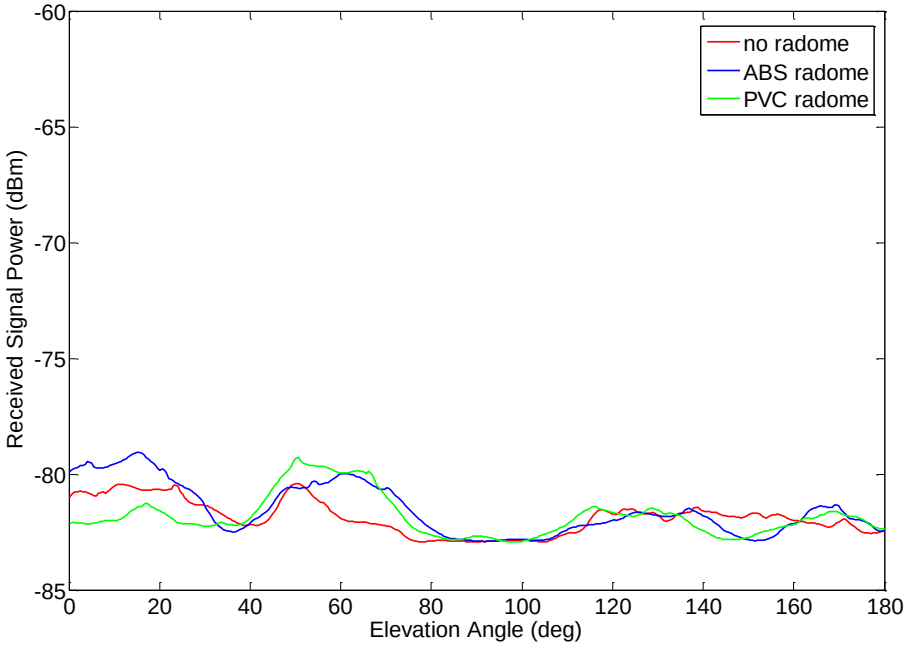

Figure 84. Elevation pattern of the SLiMS short pole at 6000 MHz with average detection and RBW = 1 MHz.

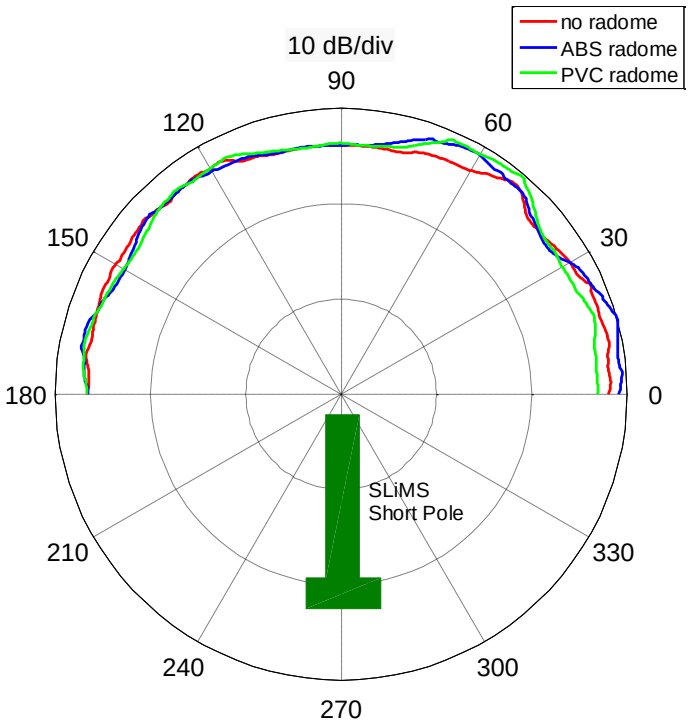

Figure 85. Polar elevation plot (side view) of the SLiMS short pole emissions at 6000 MHz.

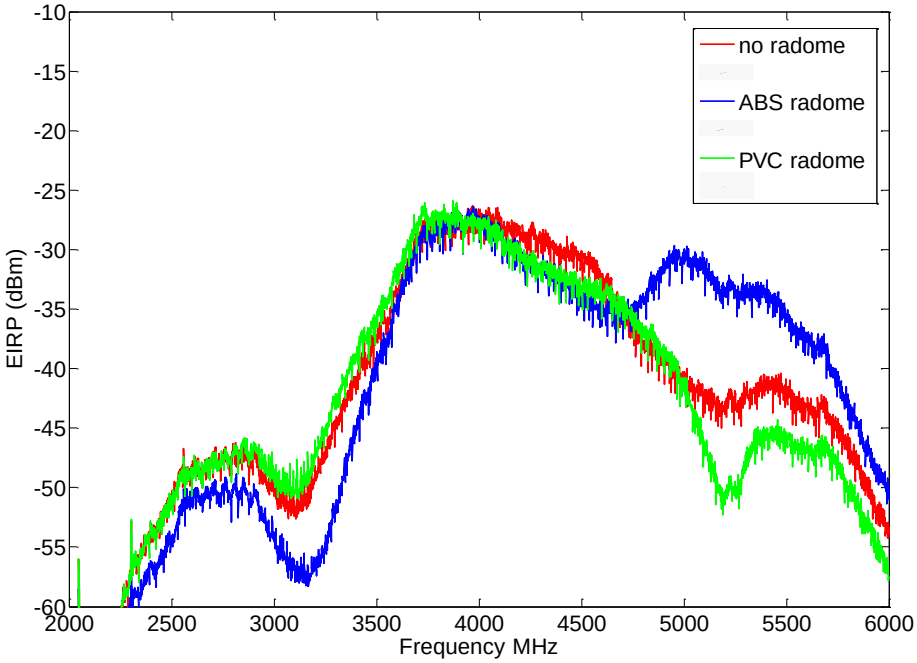

Figure 86. Maximized swept-frequency peak emissions measurements with no cover and two different radome types.

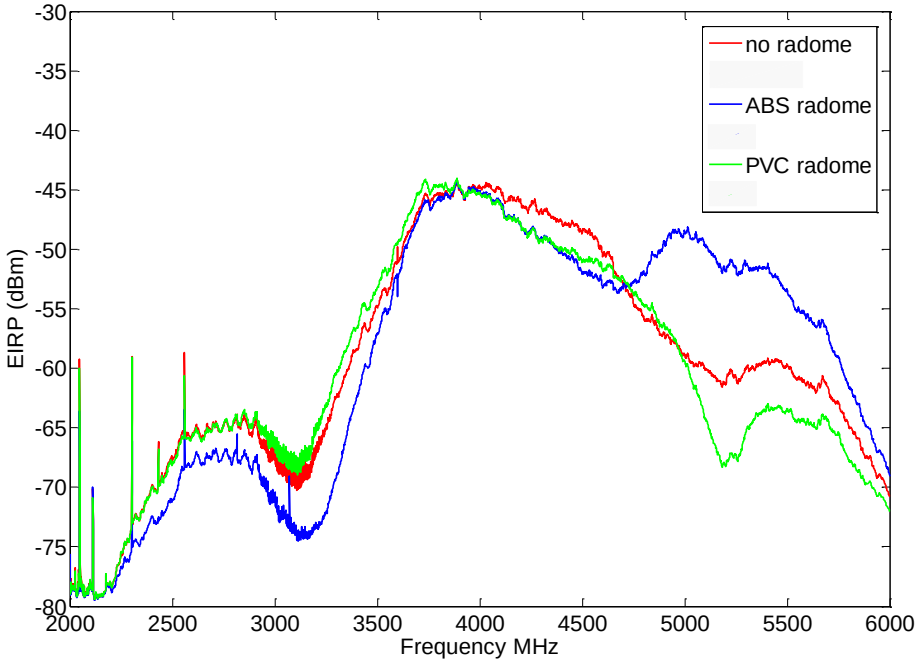

Figure 87. Maximized swept-frequency average emissions measurements with no cover and two different radome types.

4 CONCLUSIONS

The measurement of the SLiMS UWB emissions places stringent demands on the measurement test setup and configurations. The design of a test setup for measuring this UWB radar first requires a thorough understanding of the time-domain characteristics of the emitted waveform. Once that is understood, we can progress into a customized regimen of swept-frequency measurements using a spectrum analyzer.

The main challenge we face is the emission level, which has two ramifications. First we need to use a fully anechoic chamber with a high level of isolation from RF ambients. We also need high-precision measurement and positioning equipment to accurately characterize the UWB emissions and pattern characteristics. In short, a high level of precision and expertise is required to perform the characterization of a device like SLiMS.

We performed a comprehensive series of emissions measurements on the P400 UWB radar unit of the SLiMS system. We first carried out wideband time-domain measurements using a high-speed oscilloscope, recording signals at both a fast sampling rate and a slower rate to explore the time-domain structure of the radar waveform. This information enabled us to configure the spectrum analyzer for accurate frequency-domain measurements.

We characterized the conducted emissions in the frequency range of 1000–15000 MHz at five resolution bandwidths and two detector modes (peak, average). We analyzed the conducted emissions levels and used the results, in conjunction with procedures defined in the NTIA Red Book [1] to recommend an emissions designator of 1G92V1D for the SLiMS radar.

We also performed an extensive series of radiated measurements in a fully-anechoic chamber. We placed a single P400 radar system in a shortened pole to accommodate the space restrictions of the chamber as well as to provide an accurate representation of emission levels. The purpose of this was threefold: 1) to make sure that the radiated EIRP levels were below NTIA/FCC specified limits, 2) to verify that radiated emissions electric levels decay at a rate proportional to the inverse of the distance from the radar, and 3) to assess the impact of weather-protective radome materials on radiation patterns.

We measured the radiated emissions using the same combination of time- and frequency-domain instrumentation that we used for the conducted measurements. We obtained a comprehensive set of swept-frequency emissions data, time-domain waveforms at several separations between the transmit and receive antennas. We also performed a series of azimuth and elevation pattern measurements at selected frequencies. A third and final measurement campaign focused on the evaluation of two different weather-protective radome materials and the impact that these would have the emissions characteristics.

The SLiMS system exhibits radiated emissions levels that are 3 dB or more below the FCC part 15 UWB emission limits in the frequency range of 1–14 GHz. The measured SLiMS emissions were 55 dB (or more) lower than the NTIA 01-43 maximum EIRP protection level in the radar altimeter band (4200–4400 MHz). A margin of 14 dB or more is seen in the radio astronomy band (4990–5000 MHz).

We conclude that the SLiMS system has a low potential for causing interference to incumbent electronic, communication, and navigation systems.

5 ACKNOWLEDGEMENTS

The authors would like to thank Jeff Bratcher, Patti Raush, and Eric Nelson of the NTIA/ITS management team for their support. We would also thank Dennis Camell and Jason Coder of the National Institute of Standards and Technology (NIST) for their valuable assistance and guidance with the anechoic chamber testing. Finally, we would also like to thank Delmon Morrison of the NTIA Office of Spectrum Management (NTIA/OSM) for his insights and valuable discussions during his visit to the Boulder Laboratories during February, 2012.

6 REFERENCES

[1] *Manual of Regulations and Procedures for Federal Radio Frequency Management*, Washington D.C., National Telecommunications and Information Administration, May, 2011.

[2] *Spectrum Analyzer Basics*, Agilent Application Note 150-1, Agilent Technologies, June, 2006.

[3] M. Engleson, *Modern Spectrum Analyzer Measurements*, Portland, Oregon, JMS Publishing, 1991.

[4] K. Uwe-Sander, *Power Measurements on Pulsed Signals with Spectrum Analyzers*, Rohde & Schwartz Application Note 1EF48_2E, January, 2003.

[5] W.L. Stutzman and G.A. Thiel, *Antenna Theory and Design*, New York, New York, John Wiley & Sons, 1981.

[6] C.T.A. Johnk, *Engineering Electromagnetic Fields and Waves*, New York, New York, John Wiley & Sons, 1988.

[7] 47 CFR § 15 Radio Frequency Devices (2011).

[8] "Hazards of electromagnetic radiation to ordinance analysis of the Time Domain Corporation Acquisitions Holding Inc. ultrawideband P400 shoreline intrusion monitoring system," Naval Surface Warfare Center, Dahlgren Division, Report 8020, Q52/2101, January 31, 2012.

[9] G. Breed, "A summary of FCC rules for ultra wideband communications," High-Frequency Electronics, January 2005, pp. 42-44.

[10] L.K. Brunson, J.P. Camacho, W.M. Doolan, R.L. Hinkle, G.F. Hurt, M.J. Murray, R.A. Najmy, P.C. Roosa, Jr., R.L. Sole, "Assessment of compatibility between ultrawideband devices and selected federal systems," NTIA Special Publication 01-43, January 2001.

[11] E.B. Larsen, R.L. Ehret, D.G Camell, G.H. Koepke, "Calibration of antenna factor at a ground screen site using an automatic network analyzer," *IEEE International Symposium on EMC*, 23 to 25 May 1989, pp. 19–24.

[12] A. A. Smith, Jr., *Radio Frequency Principles and Applications*, Piscataway, New Jersey, IEEE Press, 1998.

APPENDIX A: SYSTEM CALIBRATIONS

We used a vector network analyzer to calibrate the spectrum analyzer measurements. There are two calibrations needed. We first need to calibrate the feed network from the receiving antenna port to the spectrum analyzer. We then need to calibrate the receiving antenna using the so-called three-antenna method. We describe these calibrations in this appendix.

A.1 Feed System Calibrations

The receiver feed network used for radiated measurements consists of two cables and a low-noise amplifier (LNA). The first section runs from the antenna port to the LNA input, and the second from LNA output to either the oscilloscope or the spectrum analyzer. The calibration process is shown in Figure A-1. We first perform a thru calibration to calibrate out the effects of analyzer cables and internal RF hardware as is shown in Figure A-1(a). The network cables are connected, and the analyzer is configured to perform measurements over the range of 750 kHz–15 GHz in 750 kHz steps.

The insertion gain characteristics of the feed are shown in Figure A-2. The gain exhibits significant variations with respect to frequency and these must be corrected for. The feed network gain also drops off significantly above 14 GHz. We also computed the feed network impulse response shown in Figure A-3 using the measured data and VNA processing software.

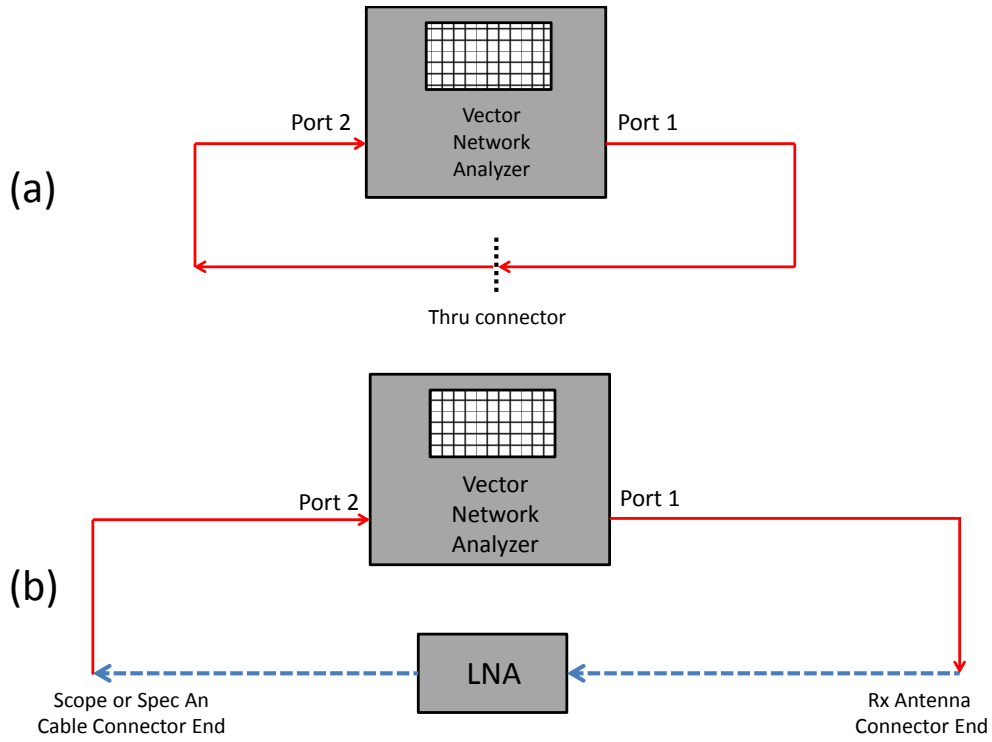

Figure A-1. (a) Thru calibration of the VNA to measure S_{21}. (b) Measurement of the receiver feed network transmission characteristics S_{21}.

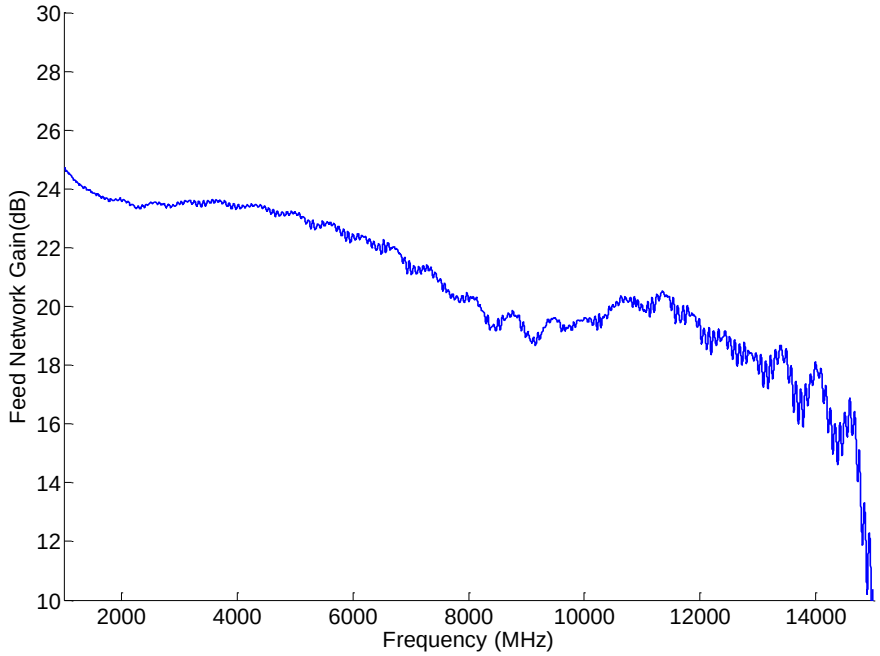

Figure A-2. Feed network insertion gain measured using the VNA.

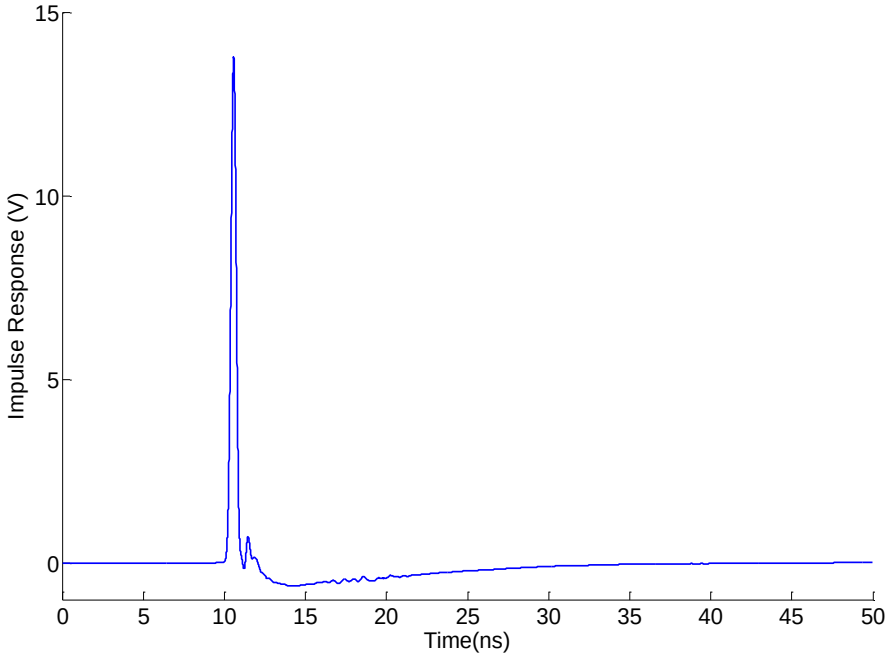

Figure A-3. Feed network impulse response obtained from the VNA measurements.

A.2 Antenna Calibrations

We performed a three-antenna calibration [11], [12] using a combination of two DRH antennas and a parabolic dish. We carried out three insertion gain measurements using the test setup

shown in Figure A-4. A VNA is used to perform stepped-frequency measurements of $|S_{21}(f)|$ over a frequency range of 1–14 GHz. Three insertion gain measurements are performed between three distinct pairs of antennas using the sequence shown in Figure A-5.

We performed the measurements at distance of 3 m between the antenna aperture planes using the test setups of Figures A-6 and A-7. The first combination consisted of a dish antenna and the first DRH receiving antenna shown in Figure A-6 to obtain $|S_{21}^{(1)}|$. We substituted in a second DRH antenna for the second measurement of $|S_{21}^{(2)}|$. Both DRH antennas are used for the third and final measurement of $|S_{21}^{(3)}|$.

The three measurements can now be applied to the following set of equations:

$$G_{dish}(dB) = \frac{1}{2}\left[\left|S_{21}^{(1)}\right|(dB) + \left|S_{21}^{(2)}\right|(dB) - \left|S_{21}^{(3)}\right|(dB)\right] + Q \quad \text{(A.1)}$$

$$G_{drh1}(dB) = \frac{1}{2}\left[\left|S_{21}^{(1)}\right|(dB) + \left|S_{21}^{(3)}\right|(dB) - \left|S_{21}^{(2)}\right|(dB)\right] + Q \quad \text{(A.2)}$$

$$G_{drh2}(dB) = \frac{1}{2}\left[\left|S_{21}^{(2)}\right|(dB) + \left|S_{21}^{(3)}\right|(dB) - \left|S_{21}^{(1)}\right|(dB)\right] + Q \quad \text{(A.3)}$$

$$Q = 10\,log_{10}\left(\frac{4\pi D}{\lambda}\right) \quad \text{(A.4)}$$

where G is the realized gain, λ is the electrical wavelength (m), and D is the antenna separation (m).

Once the gain of a particular antenna has been determined, the corresponding antenna factor is computed as follows

$$K(dB) = 20\,log_{10}[f(MHz)] - G(dB) - 29.78 \quad \text{(A.5)}$$

The measured antenna gains, which are derived from(A.1)–(A.4), are plotted for the dish and DRH antennas in Figure A-8. The dish antenna achieves peak performance in the 4–6 GHz band. Due to its much larger aperture size, the dish antenna has significantly more gain than the DRH—approximately 12 dB in the 4–6 GHz frequency range. This improved sensitivity of the dish antenna makes it ideal for the radiated measurements of the SLiMS radar. The corresponding plots for the antenna factors are plotted in Figure A-9 and the improved sensitivity of the dish antenna is manifested in the lower antenna factor values.

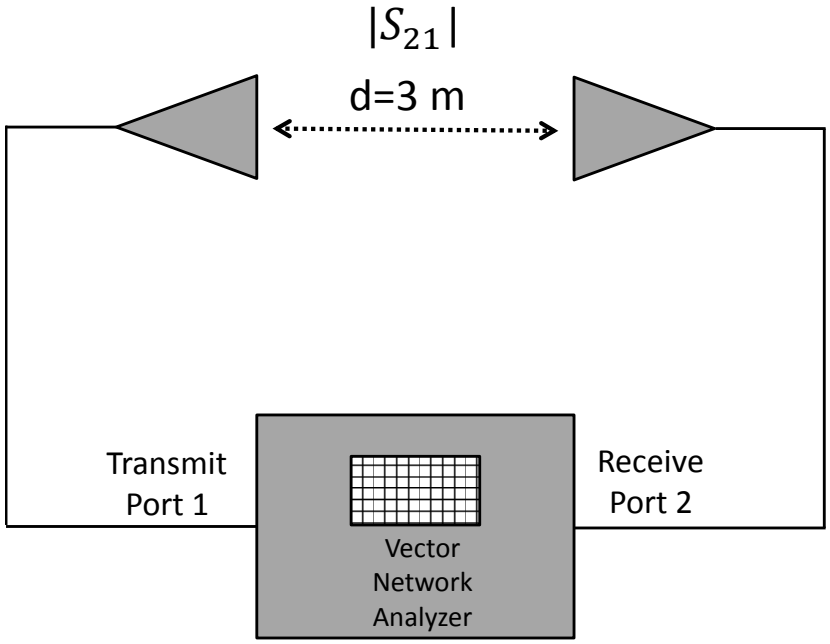

Figure A-4. Test setup for insertion gain measurements for a selected pair of antennas.

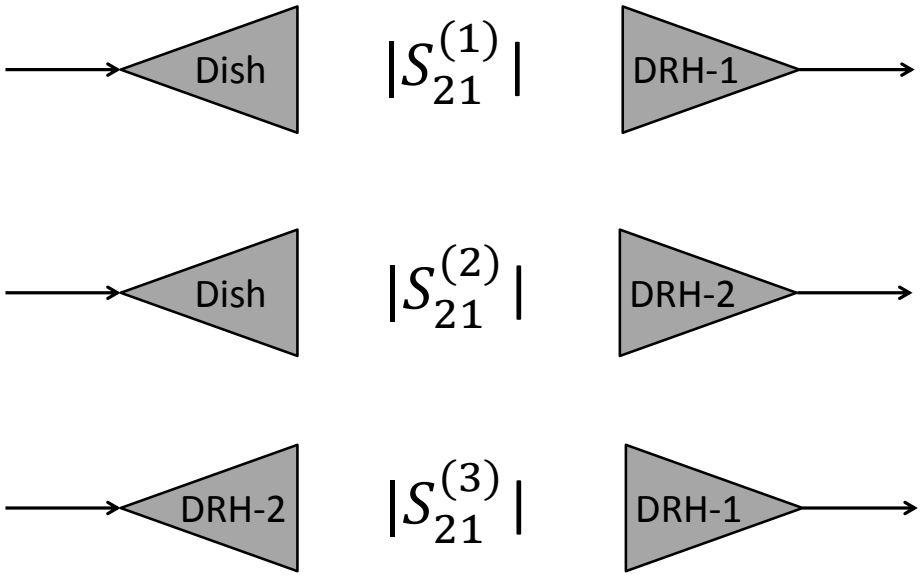

Figure A-5. Antenna pair combinations used in a three-antenna calibration.

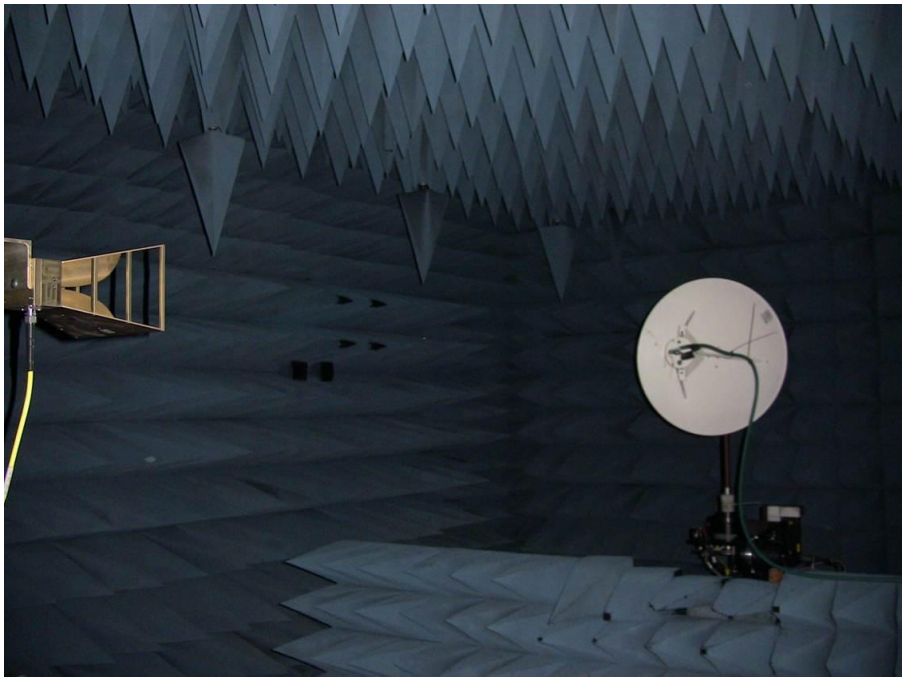

Figure A-6. Insertion measurement between a DRH and parabolic dish antenna.

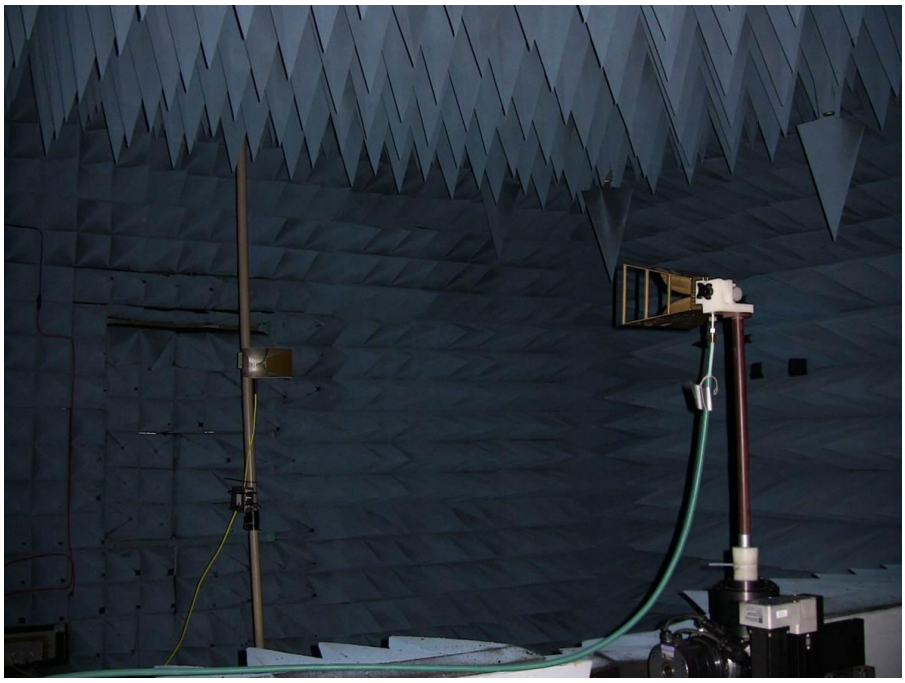

Figure A-7. Insertion measurement between a pair of DRH antennas.

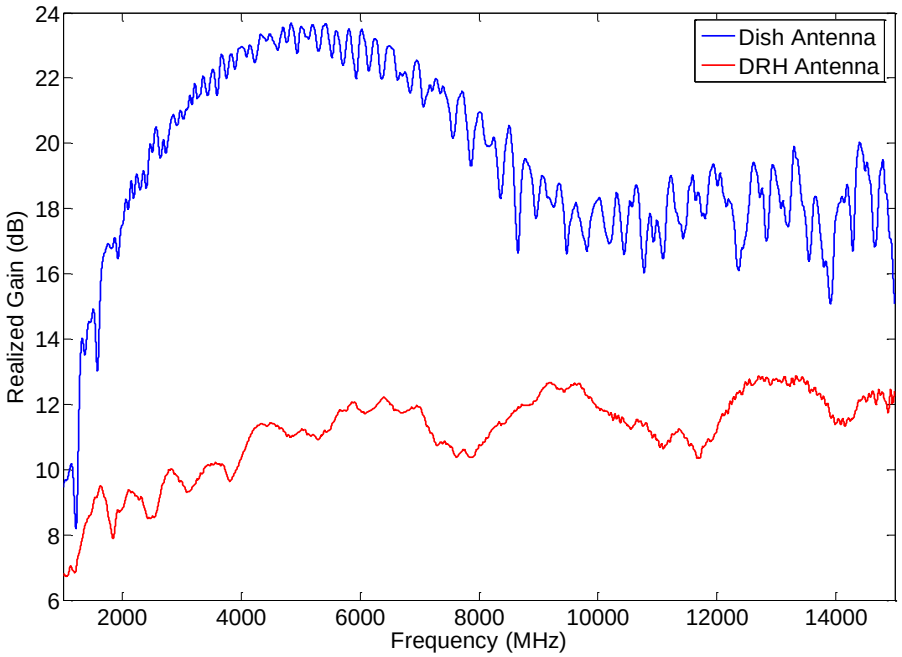

Figure A-8. Parabolic dish and DRH antenna gains obtained from a three-antenna calibration.

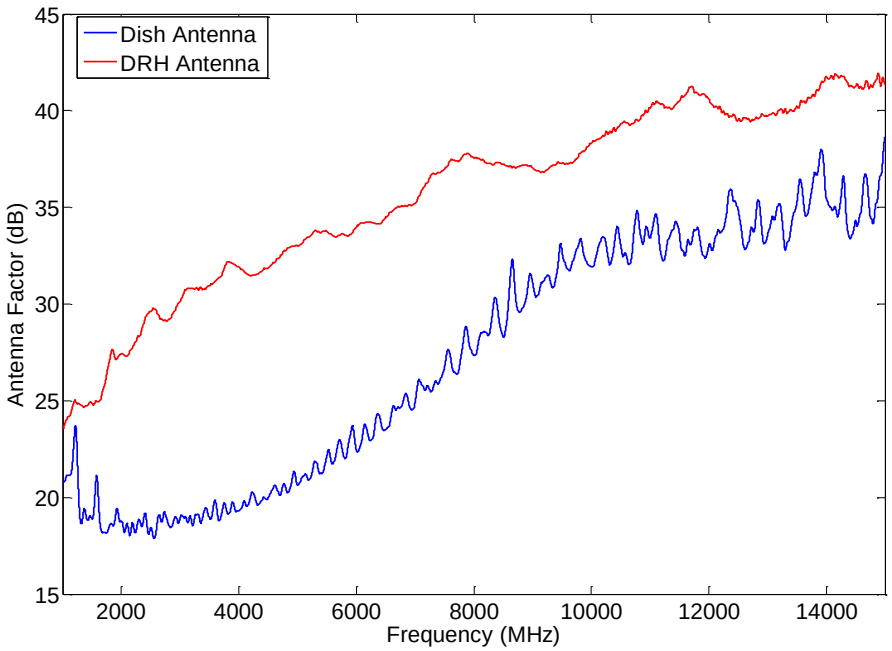

Figure A-9. Parabolic dish and DRH antenna factors obtained from the three-antenna calibrations.

APPENDIX B: EXPRESSIONS FOR EFFECTIVE ISOTROPIC RADIATED POWER

We derive expressions for the effective isotropic radiated power in terms of the power received by the spectrum analyzer. We start with a cascaded set of four equations and then combine them to develop expressions for the EIRP in both linear and decibel units. Our approach is to start at the spectrum analyzer input port, work our way back to the receiving antenna input port, and then infer the electromagnetic field parameters incident on the receiving antenna. We then use these field quantities in conjunction with the distance between the receiving antenna and device under test to compute the EIRP.

Assuming a 50 Ω system, we first express the voltage at the receiving antenna port in terms of our spectrum analyzer power reading as follows

$$V_{ant} = \frac{\sqrt{50\ P_r}}{G_f}\ (V) \tag{B.1}$$

where P_r is the power level (W) measured by the spectrum analyzer and G_f is the voltage gain of the receiving amplifier/feed cable combination. We then use the received antenna voltage, along with the measured antenna factors, to compute the incident electric field [12]

$$E_{inc} = V_{ant}\ AF\ (V/m)\ . \tag{B.2}$$

We then compute the electromagnetic power density at the receiving antenna as follows [6]

$$S_{inc} = {}^{E_{inc}^2}/_{120}\ (W/\ m^2)\ . \tag{B.3}$$

Using the combination of the incident power density and the known separation, *R*, between the receiving antenna and the device under test, we have [5]

$$EIRP = (4\pi R^2)\ S_{inc}\ (W)\ . \tag{B.4}$$

We now combine Eqs. B.1-B.4 to obtain an expression for the EIRP in terms of the received power at the spectrum analyzer input:

$$EIRP = P_r\ \left(\frac{5\ AF^2R^2}{3G_f^2}\right)\ (W)\ . \tag{B.5}$$

Thus the EIRP is the product of the received power and a correction factor that is a function of distance, the receiving feed network gain, and the receiving antenna factor.

Taking 10 log_{10} of both sides of (B.5) obtains the following expression

$$EIRP\ (dBm) = P_r\ (dBm) - G_f(dB) + AF(dB) + 20\ log_{10}(R) + 2.218\ . \tag{B.6}$$

Equation (B.6) permits us to compute the EIRP in dBm directly from the spectrum analyzer received power in dBm. We apply (B.6) to our spectrum analyzer readings with either peak or average detection.

FORM **NTIA-29**
(4-80)

U.S. DEPARTMENT OF COMMERCE
NAT'L. TELECOMMUNICATIONS AND INFORMATION ADMINISTRATION

BIBLIOGRAPHIC DATA SHEET

1. PUBLICATION NO.	2. Government Accession No.	3. Recipient's Accession No.
TR-13-491		

4. TITLE AND SUBTITLE	5. Publication Date
Conducted and Radiated Emissions Measurements of an Ultrawideband Surveillance Radar	November 2012
	6. Performing Organization Code NTIA/ITS.T

7. AUTHOR(S)	9. Project/Task/Work Unit No.
Robert T. Johnk, Frank H. Sanders, Kristen E. Davis, Geoffrey A. Sanders, John D. Ewan, Ronald L. Carey, Steven J. Gunderson	6700000-300
8. PERFORMING ORGANIZATION NAME AND ADDRESS Institute for Telecommunication Sciences National Telecommunications & Information Administration U.S. Department of Commerce 325 Broadway Boulder, CO 80305	10. Contract/Grant Number.

11. Sponsoring Organization Name and Address	12. Type of Report and Period Covered
National Telecommunications & Information Administration Herbert C. Hoover Building 14th & Constitution Ave., NW Washington, DC 20230	

14. SUPPLEMENTARY NOTES

15. ABSTRACT (A 200-word or less factual summary of most significant information. If document includes a significant bibliography or literature survey, mention it here.)

We provide detailed descriptions of recent measurements conducted by the National Telecommunications and Information Administration Institute for Telecommunication Sciences in Boulder, Colorado. ITS engineers performed a comprehensive series of both conducted and radiated emission measurements of the Shore-Line-intrusion-Monitoring System (SLiMS). The SLiMS system is currently being developed by Time Domain® under the sponsorship of the Naval Facilities Engineering Command.

16. Key Words (Alphabetical order, separated by semicolons)
amplifier; antenna; bandwidth; calibration; dual-ridged horn; dish antenna; effective isotropic radiated power; frequency-domain; oscilloscope; power; resolution; spectrum analyzer; time-domain; waveform

17. AVAILABILITY STATEMENT	18. Security Class. (This report)	20. Number of pages
☒ UNLIMITED.	Unclassified	95
☐ FOR OFFICIAL DISTRIBUTION.	19. Security Class. (This page) Unclassified	21. Price:

NTIA FORMAL PUBLICATION SERIES

NTIA MONOGRAPH (MG)

A scholarly, professionally oriented publication dealing with state-of-the-art research or an authoritative treatment of a broad area. Expected to have long-lasting value.

NTIA SPECIAL PUBLICATION (SP)

Conference proceedings, bibliographies, selected speeches, course and instructional materials, directories, and major studies mandated by Congress.

NTIA REPORT (TR)

Important contributions to existing knowledge of less breadth than a monograph, such as results of completed projects and major activities. Subsets of this series include:

NTIA RESTRICTED REPORT (RR)

Contributions that are limited in distribution because of national security classification or Departmental constraints.

NTIA CONTRACTOR REPORT (CR)

Information generated under an NTIA contract or grant, written by the contractor, and considered an important contribution to existing knowledge.

JOINT NTIA/OTHER-AGENCY REPORT (JR)

This report receives both local NTIA and other agency review. Both agencies' logos and report series numbering appear on the cover.

NTIA SOFTWARE & DATA PRODUCTS (SD)

Software such as programs, test data, and sound/video files. This series can be used to transfer technology to U.S. industry.

NTIA HANDBOOK (HB)

Information pertaining to technical procedures, reference and data guides, and formal user's manuals that are expected to be pertinent for a long time.

NTIA TECHNICAL MEMORANDUM (TM)

Technical information typically of less breadth than an NTIA Report. The series includes data, preliminary project results, and information for a specific, limited audience.

For information about NTIA publications, contact the NTIA/ITS Technical Publications Office at 325 Broadway, Boulder, CO, 80305 Tel. (303) 497-3572 or e-mail info@its.bldrdoc.gov.

This report is for sale by the National Technical Information Service, 5285 Port Royal Road, Springfield, VA 22161,Tel. (800) 553-6847.